A study of competing decay channels of nuclear systems formed in low energy heavy-ion reactions

A THESIS

Submitted to the

FACULTY OF SCIENCE

THAPAR UNIVERSITY, PATIALA

for the degree of

DOCTOR OF PHILOSOPHY

by

GURVINDER KAUR

SCHOOL OF PHYSICS AND MATERIALS SCIENCE

THAPAR UNIVERSITY

PATIALA-147004, INDIA

DECEMBER, 2014

"It is not the fruits of scientific research that elevate a man and enrich his nature, but the urge to understand."

$\sim\sim$ *Albert Einstein*

This Thesis is dedicated to

My Family

For their love, support and encouragement

CERTIFICATE

This is to certify that the thesis entitled "**A STUDY OF COMPETING DECAY CHANNELS OF NUCLEAR SYSTEMS FORMED IN LOW ENERGY HEAVY ION REACTIONS**" being submitted by **Ms. Gurvinder Kaur** for the fulfillment of the requirements for the award of Degree of Doctor of Philosophy in the School of Physics and Materials Science, Thapar University, Patiala, is a record of the candidate's own work carried out by her under my supervision. The matter presented in this thesis has not been submitted in part or full for the award of any degree in any university or institute.

Supervisor

Dr. Manoj K. Sharma

Professor and Head of Department

School of Physics and Materials Science

Thapar University, Patiala- 147004

Punjab (India)

Thapar University, Patiala

CANDIDATE'S DECLARATION

I hereby certify that the thesis entitled "**A STUDY OF COMPETING DECAY CHANNELS OF NUCLEAR SYSTEMS FORMED IN LOW ENERGY HEAVY-ION REACTIONS**" being submitted for partial fulfillment of the requirements for the award of Degree of Doctor of Philosophy in the School of Physics and Materials Science, Thapar University, Patiala, is a record of my own work carried out under the supervision of Dr. Manoj K. Sharma. The matter presented in this thesis has not been submitted by me in part or full for the award of any degree in any university or institute.

This is to certify that the above statement made by the candidate is correct to the best of our knowledge.

Supervisor
(Dr. Manoj K. Sharma)

Head of the Department
(Dr. Manoj K. Sharma)

Dean R&SP
(Dr. O.P.Pandey)

External Examiner
(Dr. B.P.Singh)

Acknowledgements

The path of success in life is full of hardships and today I believe that I have crossed one phase of life with the blessings of the almighty, the source of knowledge and inspiration who kept me motivated by surrounding with optimistic individuals throughout this challenging time of four years.

During the course of this thesis I have come across several personnel and would like to thank everyone who directly or indirectly contributed in making this goal achievable and will always remain deeply indebted to them.

Firstly, from the core of my heart, I would like to thank my esteemed supervisor Dr. Manoj K. Sharma, Professor and Head, School of Physics and Materials Sciences (SPMS), Thapar University Patiala, for not only giving me the opportunity to achieve my dream, but also for showing me what a researcher should strive to be; patient, thorough, passionate and personable. The consistent support, dynamic supervision, valuable and innovative suggestions by Dr. Sharma have enlightened my knowledge and skills in the area of nuclear physics. I owe a debt of gratitude and greatly appreciate his knowledge and willingness to always assist me in my research work. I hope that my future scientific endeavors will reflect the same dedication and accuracy. Thank you very much Sir, for helping me with everything; it has been an honor to work with you. A special word of thanks is also due to Madam Sharma for her motherly nature and care. I really enjoyed and cherish many pleasant memories of the time spent with the family, specially with Kritika and Ritvik.

I wish to express humble and special thanks to Prof. Kulbir Singh and Prof. O.P. Pandey for providing me necessary facilities in the department along with their encouragement and constant moral support to accomplish this task. I would also like to acknowledge the valuable suggestions of the members of the doctoral committee, Dr. Suneel Kumar, Dr. Alka Upadhyay and Dr. S.S.Bhatia. My sincere thanks also goes to all the faculty and

staff of the SPMS for their kind support and motivation. I am also thankful to Prof. K. K. Raina, Deputy Director, for his moral support. Thanks also goes to Dr. P.K. Bajpai, Dean of Research and Sponsored Projects for providing the possible research facilities.

The time period spent to achieve this goal is a culmination of large collaborative efforts, primarily with the my colleagues in physics department. The interactions with my seniors, Dr. Birbikram Singh, Dr. Shefali Kanwar, Dr. Gudveen Sawhney, Dr. Manpreet Kaur and Dr. Deepika Jain have provided a wonderful environment to do research and helped me through their gentle guidance and suggestions during my Ph.D. tenure.

I am grateful to my friends who shared the simulation lab with me, Rajni, Aman, Kanishka, Navjot, Amandeep, Kamal for their co-operation and encouragement.On a more personal note, the support and guidance I have received from my dear friend Mrs.Mandeep Kaur, over the voyage has been absolutely amazing. I must also express my gratitude to Ms. Neha Grover for her suggestions and help in framing this thesis. All you gals have made my time here enjoyable, and the trips to conference venues and elsewhere fun. I may not be able to list all the names running in my mind, but I thank all my colleagues in the Nuclear Physics group of the present and the past. I am also happy to acknowledge Dr.Jasminder Parmar, Dr. Karamjeet Kaur, Dr.Nidhi and Mr. Anirudh Sharma, for having the doors open to any of my questions and problems, for invaluable help and jovial company.

I deeply appreciate my friends, Mrs. Kirandeep Sunny Sandhir , Mrs. Pooja Munish Arora, Mrs. Anubha Harish Chopra who have helped me in ways unknown to them. I am also thankful to the lovely Garg family and specially gratefull to Mr. Mohit Garg for making difficult situations much easier and giving me a fascinating insight to life. I admire his suggestions which have helped me to iron out the creases in my thesis. You people have always taken my problems as your own, and helped me to overcome them,

and encouraged me to achieve a high level. Thank you so much for your faithful love and endless help. I could say, without you all, this thesis wouldn't exist.

Lastly the most important, I also thank my entire family for allowing me to further my studies. God is generous enough to bless me with worlds best brother, S. Amrinder Singh, who always stood by me in all situations. I also feel immense admiration and gratitude for my parents, S. Ranjit Singh and Sdn. Sukhvinder Kaur who have always been my strongest support and my source of motivation during moments of despair and discouragement. Thanks Mama and Papa, for giving me the zest to learn and your endless love and strong belief in me. I am honoured to have you as my parents and deeply appreciate your love, support, encouragement and sacrifices. Thank you for giving me a chance to prove myself and I'm glad that I could live upto your dreams and make you proud of me. This work is dedicated to you for your love and sacrifice.

You all have kept me well-balanced and have tried to make this challenging task a pleasant journey.

The financial assistance from Department of Science and Technology and then from University Grants Commission (UGC), New Delhi, under the "Maulana Azad National Fellowship For Minority Students Scheme" is gratefully acknowledged.

Patiala

December, 2014.

(Gurvinder Kaur)

List of Publications

I. International Journals:

1. Compound and non-compound nucleus contributions in the evaporation residue cross-sections of ^{20}Ne + ^{181}Ta$\rightarrow$ ^{201}Bi* reaction at $E_{c.m.}$ = 135 MeV and 162 MeV, **Gurvinder Kaur** and Manoj K. Sharma, Nucl. Phys. A **884**, 36 (2012).

2. Decay of ^{150,158}Tb* nuclear systems formed in reactions induced by loosely bound ^{6}Li,

   Gurvinder Kaur and Manoj K. Sharma, Phys. Rev. C **87**, 044601 (2013).

3. Formation and decay cross-sections of ^{66}As* formed in an exotic proton-halo ^{8}B induced reaction,

   Gurvinder Kaur, Deepika Jain, Raj Kumar and Manoj K.Sharma, Nucl. Phys. A **916**, 260 (2013).

4. Role of rotational energy and deformations in the dynamics of ^{6}Li+^{90}Zr reaction,

   Gurvinder Kaur,Neha Grover, Kirandeep Sandhu and Manoj K.Sharma, Nucl. Phys. A **927**, 232 (2014).

5. Theoretical study of odd-mass Fr isotopes using the collective clusterization approach of the dynamical cluster-decay model,

Gudveen Sawhney, **Gurvinder Kaur**, Manoj K. Sharma and Raj K. Gupta, Phys. Rev. C **88**, 034603 (2013).

6. Dynamics of ^{40,48}Ca+^{238}U→ ^{278,286}112* reactions across the Coulomb barrier using dynamical cluster decay model,
   Kirandeep Sandhu, **Gurvinder Kaur** and Manoj K. Sharma, Nucl. Phys. A **921**, 114 (2014).

7. Fragment mass identification and related aspects in the decay of ^{40}Ca* and ^{39}K* nuclei,
   Gurvinder Kaur and Manoj K. Sharma, Int. Jour. of Mod. Phys. E **23**, 1450063 (2014).

8. Dynamics of ^{6}Li+^{1152}Sm→ ^{158}Tb* reaction across the Coulomb barrier,
   Gurvinder Kaur and Manoj K. Sharma, AIP conference proceedings, **1524**, 155 (2013).

9. Dynamics of light, intermediate, heavy and superheavy nuclear systems formed in heavy-ion collisions,
   Manoj K. Sharma and **Gurvinder Kaur**, Pramana-Jour. of phys. **82**, 919 (2014).

10. Cluster decay analysis and related structure effects of fissionable heavy and superheavy nuclei,
    Manoj K. Sharma and **Gurvinder Kaur**, Pramana-Jour. of phys (10.1007/s12043-015-1058-9).

11. Fission dynamics of ^{240}Cf* formed in ^{34,36}S induced reactions,
    Deepika Jain, **Gurvinder Kaur** and Manoj K. Sharma, EPJ Web of conferences **86**, 00016 (2015).

12. Fission decay analysis of n-induced reaction using collective clusterization approach
Amandeep Kaur, **Gurvinder Kaur** and Manoj K. Sharma, Nucl. Phys. A **941**, 152 (2015).

13. Decay of Zr isotopes and related nuclear structure effects,
Gurvinder Kaur, Rajni and Manoj K. Sharma, Phys. Scripta (Accepted)

14. Dynamics of ^{16,18}O induced reactions using Ni, Ge and Mo targets,
Rajni, **Gurvinder Kaur** and Manoj K. Sharma, Eur. Phys. Jour. A (under review).

15. Comparative study of pre-actinide and trans-actinide nuclei formed using various projectiles induced on ^{197}Au target at E^*_{CN}=60MeV
Neha Grover, **Gurvinder Kaur** and Manoj K. Sharma, Phys. Rev. C (under review).

II. International and National Conferences, Symposiums and Workshops:

1. Fusion-fission of very light mass compound nucleus ^{28}Al* using the dynamical cluster decay model, BirBikram Singh, **Gurvinder Kaur**, Manoj K Sharma and Raj K Gupta, Proceedings of Department of Atomic Energy symposium on nuclear physics, Andhra University, (Vishakhapatnam), Vol. **56**, 474 (2011).

2. Evaporation residue cross-section of ^{201}Bi* formed at $E_{c.m.}$=135 MeV, **Gurvinder Kaur** and Manoj K. Sharma, Proceedings of Department of Atomic Energy symposium on nuclear physics, Vol. **56**, 530 (2011).

3. Fusion excitation functions of $^{66}As^*$ formed in ^{8}B + ^{58}Ni reaction at near barrier energies, **Gurvinder Kaur**, Deepika Jain, Raj Kumar, Manoj K. Sharma, Pro-

ceedings of Department of Atomic Energy symposium on nuclear physics. Vol. **57**, 502 (2012).

4. Fusion-fission of compound nucleus $^{28}Al^*$ formed in $^{18,17}O+^{10,11}B$ reactions using dynamical cluster decay model, BirBikram Singh, **Gurvinder Kaur**, Manoj K Sharma and Raj K Gupta, Proceedings of Department of Atomic energy symposium nuclear physics, Delhi University, Delhi, Vol. **57**, 550 (2012).

5. Fragment Mass Distribution of Radioactive $^{238}U^*$ Nucleus, **Gurvinder Kaur**, Amandeep Kaur and Manoj K. Sharma, 3^{rd} National Conference on Advanced Materials and Radiation Physics (AMRP), RP(P)-15, pp-85. (2013).

6. Shell closure effects in the decay of Fr isotopes, Gudveen Sawhney, **Gurvinder Kaur**, Manoj K. Sharma and Raj K. Gupta, Proceedings of Department of Atomic energy symposium nuclear physics, BARC, Vol **58**, 404 (2013).

7. Effect of Centrifugal potential on the dynamics of ^6Li induced reaction, **Gurvinder Kaur** and Manoj K. Sharma, Proceedings of Department of Atomic energy symposium nuclear physics, BARC, Vol **58**, 416 (2013).

8. Fusion-fission and quasi-fission contribution in decay of heavy mass nuclei, **Gurvinder Kaur**, Neha Grover, and Manoj K. Sharma, Proceedings of Department of Atomic energy symposium nuclear physics, BHU, Vol **59**, 344 (2014).

9. Dynamics of transuranic $^{240}Np^*$ nucleus formed in n-induced reaction, Amandeep Kaur, **Gurvinder Kaur** , and Manoj K. Sharma, Proceedings of Department of Atomic energy symposium nuclear physics, BHU, Vol **59**, 364 (2014).

10. Dynamics of $^{92}Zr^*$ and $^{108,110}Sn$ nuclei formed in $^{16,18}O$-induced reactions, Rajni, Kanishka Sharma,**Gurvinder Kaur**, and Manoj K. Sharma, Proceedings of

Department of Atomic energy symposium nuclear physics, BHU, Vol **59**, 562 (2014).

Contents

List of Figures

List of Tables

Abstract

The present study is carried out to understand the theoretical aspects and signatures of various decay processes observed in reactions involving heavy, intermediate and light mass nuclei. The decay of hot (T≠0) and rotating (ℓ≠0) nuclear systems formed in low energy heavy ion reactions is studied in form of evaporation residues (ERs; also called light particles LPs), intermediate mass fragments (IMFs) and symmetric, asymmetric fission fragments, by applying the dynamical cluster-decay model (DCM), which treats all these decay processes on equal footing. The DCM, applied to study the aforementioned decay processes for various nuclei formed via complete fusion (CF) and incomplete fusion (ICF) processes focusses primarily on the role of deformations, related optimum orientations, temperature and angular momentum effects. Besides this an attempt is also made to address the non-compound nucleus (nCN) mechanisms such as quasi-fission (QF) and deep inelastic collision (DIC) in framework of DCM. The thesis is organized into seven chapters and the outline of wok carried is given below.

Chapter 1 starts with general introduction of nuclear physics, its applications, importance, relevance to mankind and converges to the understanding of nuclear reaction dynamics and related nuclear structure effects involved in low energy heavy ion collisions. Further, an extensive study of compound nucleus (CN) formed through CF, the ICF process and the nCN mechanism is carried out explaining the factors influencing the

formation and decay of these processes.

Chapter 2 gives the detail of methodology used, the DCM for the decay of hot and rotating nuclei. It is based on quantum mechanical fragmentation theory (QMFT) and the temperature, angular momentum, deformations and orientations effects are incorporated within DCM description. It is a two step process where the stationary state Schrodinger equation having fragmentation potential as an input, is solved to obtain the preformation probability of decaying fragments while, the WKB approximation is used to establish the penetrability of decaying fragments. The fragmentation potential is calculated as sum of binding energies, Coulomb interaction potential, proximity potential and angular momentum dependent potential. In DCM, the emission of LPs, IMFs and fission fragments upto symmetric division of the compound nucleus, are treated on equal footings as the dynamical collective mass motions of preformed clusters or fragments through the barrier, in contrast to statistical models which follow different formalisms for different processes. The application of DCM is extended further in view of ICF, QF and DIC etc.

In **Chapter 3**, the decay of CN in form of ERs and fission fragments is studied using DCM, for the odd-mass $^{211-219}$Fr* compound systems formed in ^{18}O+^{197}Au and ^{19}F+^{192,194,196,198,200}Pt reactions. The ER cross-sections of ^{215}Fr* are predicted using the systematics attained through ER cross-sections of ^{213,217}Fr* isotopes. In addition to this, the fission and ER cross sections of ^{213,217}Fr* isotopes are extended to higher energies. Further, to check for the consistency of earlier observations of ^{215}Fr* and absence of QF contribution, the fission fragment anisotropy is calculated for ^{213,217}Fr* isotopes. Additionally, the entrance channel effect for ^{215}Fr* formed through ^{18}O+^{197}Au and ^{19}F+^{196}Pt reaction is analyzed through the variation of fragmentation potential, preformation fac-

tor and decay barrier height. Also, the shell closure effects of decaying fragments are explored in context of decay pattern observed for odd mass Fr isotopes, A_{CN}=211-219. Besides this, the contribution of QF is worked out for isotopes of superheavy $^{278}112^{*}$ and $^{286}112^{*}$ nuclei, through the orientation degree of freedom studied using DCM. For the use of cold (polar) elongated orientation, an overestimation of fission cross-section in the deep sub-barrier region is observed which may be associated with the QF decay channel. In agreement with experimental observations, the contribution of quasi-fission is more for the neutron-deficient $^{278}112^{*}$ isotope as compared to $^{286}112^{*}$ nucleus.

In **Chapter 4**, the role of static and dynamic (temperature dependent) quadrupole deformations is studied in framework of DCM for the decay of intermediate mass $^{158}Tb^{*}$ nucleus formed in $^{6}Li+^{152}Sm$ reaction. The ER decay cross-sections are calculated using spherical choice of fragmentation, and by considering static $\beta_{2i}(0)$ and dynamic $\beta_{2i}(T)$ quadrupole deformations within optimum orientations θ_i^{opt} approach. The barrier modification and angular momentum dependence is duly addressed for $^{158}Tb^{*}$ nucleus. Also, the shell closure effect and the iso-spin dependence of decay fragments is studied for $^{150}Tb^{*}$ nucleus formed in $^{6}Li+^{144}Sm$ reaction, and comparative analysis is carried out with $^{158}Tb^{*}$ nucleus. Furthermore, the orientation effect is investigated by considering hot (equatorial) compact as well as cold (polar) elongated orientational features. Finally, the ER cross-sections corresponding to ICF observed due to break up of loosely bound ^{6}Li projectile induced on the deformed target ^{152}Sm is worked out in the framework of DCM by applying relevant energy correction as discussed in chapter 2.

In **Chapter 5**, the role of higher order deformation effects, upto hexadecapole (β_2-β_4) are studied for the decay of heavy mass $^{201}Bi^{*}$ nucleus formed in $^{20}Ne+^{181}Ta$ reaction. The

decay of ^{201}Bi* system in form of ER decay channel is studied for spherical choice and with inclusion of quadrupole (β_2) and hexadecapole (i.e β_2+β_3+β_4) deformations. Further, the decay cross-sections observed through ICF of ^{20}Ne projectile are also studied using DCM and results obtained are found to be consistent with Morgestern systematics. In addition to this, for the ER decay of light mass ^{96}Tc* system formed in ^{6}Li induced reaction, the effect of angular momentum in reference to the sticking (I_S) and non-sticking (I_{NS}) limit of moment of inertia is analyzed. The effect of either of the two approaches on the angular momentum and hence the rotational energy associated with it, is assessed through the fragment mass distribution, preformation factor and the barrier penetrability and it is observed that I_S approach is more favorable to address fusion excitation functions. Besides this, the role of angular momentum in disentangling the CF and ICF contribution observed due to break-up of loosely bound ^{6}Li projectile is exercised explicitly. It is observed that for both ^{20}Ne and ^{6}Li induced reactions, the cross-sections calculated using DCM are in agreement with experimental observations for complete fusion and incomplete fusion processes.

In **Chapter 6**, a systematic decay study of light mass $^{66}As^{*}$ nucleus formed through proton-halo ^{8}B induced reaction is carried out in framework of DCM in reference to the ER, IMF and fission decay fragments. The calculations suggest that the fusion excitation function of $^{66}As^{*}$ consists of LPs as the most dominant contributors, followed by IMFs and fission fragments. A description of deformation effects is also provided by comparative analysis of spherical and deformed choice of fragmentation by opting deformations upto quadrupole (β_{2i}) and hexadecapole ($\beta_{2i} - \beta_{4i}$). The DCM based excitation functions agree well with the observed experimental cross sections for all three choices of fragmentation. Also the cross-sections are predicted using DCM at higher energies, which need

experimental verification in near future. Further, decay of very light mass $^{40}Ca^{*}$ and $^{39}K^{*}$ nuclei formed in asymmetric channels $^{12}C+^{28}Si$, $^{11}B+^{28}Si$ and $^{12}C+^{27}Al$ are investigated using spherical choice of fragmentation in framework of DCM. In reference to the experimentally measured charge particle cross sections, the fragment masses and their relative contribution towards the decay of $^{40}Ca^{*}$ and $^{39}K^{*}$ nuclei is identified. Also, the role of entrance channel is investigated by studying the decay of $^{39}K^{*}$ nuclear system formed in two different reactions at same excitation energy. The behavior of fragmentation potential, preformation probability and penetrability is analyzed to figure out the favorable mass fragments, their relative emergence and the entrance channel effects etc. In addition to this, the cross sections for the LPs and heavier charge fragments are estimated for the CN decay. Besides this, one of the nCN process, DIC is also addressed in context to DCM approach. The cross sections obtained in framework of DCM for both CN and nCN processes are found to have nice agreement with the available experimental data.

Finally, in **chapter 7**, conclusions and an outlook of the work is presented.

Chapter 1

Introduction

Ever since the Big Bang, origin and evolution of universe continues to be an enigma and nuclear matter forms an essential requisite in understanding it. This is by virtue of the fact that, nuclear matter originates from the soup of quarks and gluons together arranging themselves to form protons and neutrons, which collectively represents a nucleus that accounts for the mass of an atom and extends upto the enduring nuclear reactions being carried in sun that make life on earth viable. Figure 1.1 illustrates different ways through which nuclear physics enters our world, its applications and importance to society. Initiating at very small length scale ($\sim 10^{-19}$cm), nuclear physics starts contributing in form of basic constituents of matter-the quarks which appear in our world as building blocks-the protons and neutrons and give rise to an atomic nucleus. The origin of nucleus further results into an atom which combine together to form a molecule. The applications of nuclear physics perforates from the structure of molecules determined by nuclear magnetic resonance (NMR). At further larger length ($\sim 10^{2}$cm), with the impact of "tools or engines of discovery"-the accelerators and detectors, the application of nuclear physics extends from nuclear medicine such as nuclear diagnostic techniques for tumor diagnosis and therapy, nuclear power generation and nuclear weapons to accelerator mass spec-

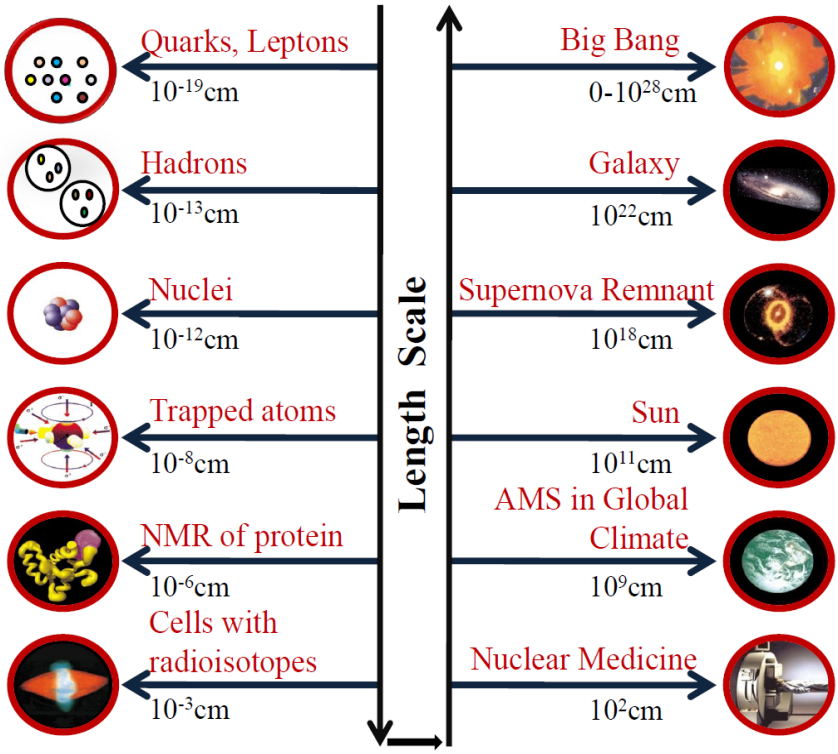

Figure 1.1 Illustration of different phases of nuclear matter and hence the nuclear physics, its constituents and diverse features entering our world at different length scales.

troscopy implied to study the global climate variations. The implementation of nuclear phenomenon further extends to the Sun- burning its nuclear fuel, supernovae, the galaxies whose light shines from nuclear reactions in stars and finally returns to the Big Bang whose remains encompass the universe. Thus, a nucleus can be viewed as a linking bridge between the infinitesimal and astronomical world [1] and hence needs to be explored intensively by studying its properties, behavior and internal structure. Before discussing the motivation, methodology and henceforth the results obtained in the present work, a concise account of background and basics of nuclear physics is made ahead.

Nuclear physics as a field distinct from atomic physics, originated with the discovery of radioactivity by Henri Becquerel in 1896 [2] and gained impetus as the 19^{th} century headed towards an end, with the advent of quantum mechanics (a theory more general

than classical mechanics). Investigating the world of atomic nucleus at microscopic level revealed that it is composed of two fermions-the positively charged protons and the electrically neutral neutrons, which are almost identical except for difference in charge they possess. These fermions collectively called nucleons are closely packed together in a nucleus, which is heavier than the negatively charged electrons orbiting around it in an atom. Ever since its experimental discovery by Ernest Rutherford [3], various theoretical models were developed to account for structure, properties and interaction of nuclei. For instance, the macroscopic approach such as Liquid Drop Model (LDM) described the average properties of nuclei like trend of binding energy with respect to mass number and provided preliminary inputs regarding the fusion-fission dynamics [4]. However, the attempts made to understand the dynamic properties of a nucleus using LDM were not very prosperous as the macroscopic approach neglects the effect of non-uniform distribution of nucleons. To account for unique distribution of nucleons, corrections were applied to macroscopic approach by means of Shell Model by Maria Goeppert-Mayer and Hans Jensen [5], which described the behavior of magic numbers and properties such as angular momentum, magnetic moment, shape and nuclear spectra of a nucleus. The macro-microscopic approach obtained by implying energy corrections for ground and excited states [6] were based on Nilsson or Wood-Saxon single particle potential. Nilsson Model approach has also been exercised to address the deformed intrinsic states of nuclear systems [7]. Besides this, the Collective Model by Aage Bohr and Ben Mottleson [8] involved the rotational and vibrational features and complemented the Shell Model by considering even-even nuclei having no valence particles. Further, the Unified Model described nuclear properties by including features of both Shell Model and Collective Model. By means of these important nuclear models explaining different features of nuclei, numerous new theoretical approaches have been developed to enhance the understanding of nuclear structure. This proved beneficial

in interpretation of various nuclear phenomenon which are governed by three fundamental forces, the gravitational, electroweak [9] and strong force [10], each playing its own special role. An extensive effect of attractive gravitational force is apparent in neutron stars which eventually behave like gigantic nuclei whereas, the electroweak and strong forces are perceived to influence the nucleus of an atom. The interaction of charged protons in the nucleus is governed via the electromagnetic force while the weak forces cause transformation between the nucleonic states. Moreover, the existence of a nucleus is attributed to the much pronounced attractive strong force, which suppresses the repulsive Coulomb force between the protons and binds them together with neutrons. In comparison to other fundamental forces, the experimental investigation and theoretical analysis of the strong force has always been a challenging task due to its short range (maximum upto 2 fm distance). Despite this, continuous attempts are being made to percept the behavior of nuclear forces completely, as it may lead to tremendous advancement in the overall understanding of nuclear behavior and its associated applications. Therefore, for better understanding of the short range forces, the analysis of structure and dynamics involved in a reaction has always been a central point in nuclear physics. Each type of reaction exhibits certain specific nuclear properties which are constructively helpful in comprehensive study of nuclear structure and related dynamics. For instance the nucleon-nucleon scattering helps to learn more about the fundamental nuclear forces while the elastic scattering of nuclei provides information regarding nuclear size and interaction potential. Besides this, the reactions involving compound nucleus (CN) formation are helpful in studying the statistical properties of a nucleus whereas the fusion and fission reactions reveal information about the astrophysical processes and properties of the Liquid Drop Model respectively.

1.1 Type of nuclear reactions

Nuclear reactions may be segregated into numerous brackets, based on features like energy, type of incident nuclei, mechanism involved etc. On the basis of energy domain, the reactions may be classified into three different categories varying from few MeV/nucleon upto GeV/nucleon. The low energy reactions with incident beam energy, $E_{beam}\leq$15 MeV/nucleon enormously describe the fusion, fission, particle evaporation and cluster decay processes through a variety of statistical methods [11–14] or alternatively via clusterization approach based preformation cluster-decay model (PCM) [15] and dynamical cluster-decay model (DCM) [16–26].

The PCM is used to address ground state decay whereas DCM is applied to account for excited state decay patterns of nuclear systems. The energy range 15 MeV/nucleon to 500 MeV/nucleon corresponds to intermediate energy reactions where processes like flow of particles, stopping, multifragmentation etc., are observed and dealt through models such as Cascade, QMD [27] etc., while the reactions with energy above 500 MeV/nucleon describe high energy nuclear reactions which fall in the domain of particle physics. The average/mean nuclear force field acting between the nucleons dominate in low energy reactions [28] and nucleon-nucleon interactions are evident at high energy whereas, both the aspects are found to exist in intermediate energy regime. The low energy nuclear reactions form a clear picture of two-body problem, but the extrapolation of its results show a remarkable difference at higher energies. This may lead to the fact that the exchange properties as well as distance influence the mode of interaction deeply at high and intermediate energies. For instance, the reactions at low energy strongly suggest that nuclear force is charge independent [10] whereas the intermediate and high energy reactions indicate different forces acting between proton-proton and proton-neutron pair [29]. The low energy reactions are helpful in understanding the structure of nuclei, while the

reactions studied at intermediate energy help in analyzing the interactions among proton and neutron in the excited composite system. It also aids in investigating the relation between density and pressure, the so-called equation of state which plays crucial role in exploring the composition, evolution of neutron stars and the conditions which prevailed after the formation of universe [30]. Thus, each type of reaction with its own specific scenario provides information that helps to frame a better picture of reaction dynamics and nuclear physics as a whole. The low energy nuclear reactions, to which the work in this thesis is confined, provides useful information regarding fundamental properties of nucleus and associated dynamical aspects, without much recourse to subnuclear degrees of freedom which are important for intermediate and high energy reactions.

In addition to incident energy, the projectile involved also plays a significant role in studying the dynamics of a given reaction. Embarking the beginning of nuclear reactions (1911), the energetic α-particle from radioactive source was used as a projectile in the celebrated Rutherford scattering experiment. A little later (1919) transmutation into different particles was discovered following which many successful attempts were made to study nuclear reaction dynamics involving alpha particles. The significant and remarkable discoveries like production of first nuclear reaction, establishment of structure of nucleus, discovery of neutron which subsequently lead to discovery of fission and generation of free energy have been possible with the use of α-particle emitted from natural radioactive sources. However, these sources imposed severe restrictions as they provided very limited energy range and extremely low intensities. This limitation was resolved with the invention of first linear accelerator 'LINAC' (1929), through which nuclear reactions initiated with proton accelerated beams was possible. Further, an impetus was gained when Chadwick discovered neutrons (1932), which due to their neutral nature are not influenced by Coulomb force in the entrance channel and turned a keystone in studying

fundamental structure of nuclei. Interestingly, neutron induced reactions also considered as an isospin-symmetric counterpart of proton induced reactions, proved to be an initial source for synthesis of superheavy elements. The use of neutrons as projectile helped in removing various inconsistencies such as those related to nuclear isotopes and brought significant achievements like fundamental symmetry of isospin and formulation of the idea of charge independence of the nuclear interaction by Heisenberg. However, the absolute determination of neutron cross-sections, flux and energies requires careful calibration and suitable models and codes.

Interestingly, with persistent efforts, the scientist have produced a variety of nuclear beams (projectiles) and one seeks to understand the changing nature and mechanisms observed in collision of projectile and target nuclei at ever increasing energies. With highly advanced particle accelerator techniques, nuclear reactions could be produced using high energy beams of not only protons, deuterons, neutrons and alpha particles but also heavy ions (heavier than α-particle) over a wide range of precisely controllable bombarding energies. The transition from light charged particles to heavy ion induced reactions, which take place predominantly at or near the nuclear surface, came into widespread use as a versatile probe for nuclear reaction dynamics and as an indispensable constituent in interpretation of nuclear forces.

Amongst various applications of heavy ion reactions (HIRs), the production of exotic and superheavy nuclei has been an asset. The modern nuclear reactions tend to deviate from stable and excited deformed nuclei towards the investigation of region near the drip line, having excess and deficient neutrons or the region of new superheavy elements. Unlike collision with protons and neutrons, the HIRs involve relatively large number of nucleons due to which their theoretical description is laborious task and is limited to approximate reaction models. In the present work, we have concentrated on low energy

heavy ion reactions and intend to explore various decay mechanisms observed through CN and non-compound nucleus (nCN) reactions using collective clusterization approach of the dynamical cluster decay model (DCM) [16–26].

1.2 Compound Nucleus Reactions

In 1936, Niels Bohr and Kalckar proposed the theory for CN reactions as a two stage process. The former stage involves capture of incident projectile by target nucleus with sufficient kinetic energy to overcome the mutual electrostatic repulsion, followed by distribution of energy among all nucleons of the composite system. Consequently, the CN has long mean-life time (10^{-14} s) in comparison to the characteristic time of nuclear interaction (10^{-23} s) and is statistically equilibrated in all degrees of freedom. In the later stage, succeeding formation, the excited CN does not retain the history of its formation and decays either through the emission of light particles analogous to evaporation of molecules from the liquid droplet or through the emission of binary fission fragments. In general the nuclear dynamics obeys the Bohr independent hypothesis which was first tested experimentally by Ghoshal (1950) and later by others [31]. Interestingly, the hypothesis was enormously beneficial in exploring reaction dynamics as it lead Weisskopf and Ewing [32], to develop a theory for total cross-section and subsequently enabled Hauser and Feshbach [11], to account for differential cross-sections. Over the years, many quantum mechanical theories have been developed to study the formation and decay of a CN and account for the structure and related dynamics involved in HIRs [33].

The formation of CN observed due to fusion of nuclei confined in the range of attractive nuclear force, is influenced by many factors such as incident energy, position of projectile in reference to the target nucleus, structure and shape of the interacting nuclei.

Thus, understanding the formation of CN requires thorough description of complete fusion process which may be considered as a quantum mechanical tunnelling through the barrier governed by the long range Coulomb potential, the short range nuclear potential and the centrifugal potential. Ever since the availability of heavy ion accelerators, mechanism of fusion has been a topic of considerable interest. Eventually, it gained significant importance with the emergence of advanced experimental techniques for investigation of loosely bound radioactive (rare) isotopes, with halo nuclei such as ^{6}He,^{6,7,11}Li,^{9,11,14}Be,^{8}B and many more, being a special case amongst them [34]. These nuclei possessing anomalous properties, affect the reaction dynamics and are mandatory to be studied in order to attain clear picture of fusion. Owing to their extended structure, loosely bound nuclei exhibit an increased penetration probability through the potential barrier thus causing enhancement in fusion cross-sections. On the other hand, one or more valence neutrons (protons) circulating around the core account for low threshold and increased probability of break-up, resulting into fusion hindrance and thus reduction in fusion cross-sections [35]. The difference in dynamics of loosely bound reactions from those of tightly bound was first pointed out by Takigawa and Sagawa [36] following which several experiments were performed to analyze the conditions prevailing in them. Many experimental techniques such as gamma-ray spectroscopy, X-ray detection [37] and theoretical approaches like coupled channel have been applied to measure the fusion cross-sections of tightly bound and loosely bound nuclei.

To have an insight of composite system and evolution of CN, the decay mechanisms also need to be studied in addition to its formation. During collision, depending on interaction of incident beam, the hot and rotating CN is internally excited and decays by emitting radiations, charged particles or heavier nuclei. Depending upon its mass (A_{CN}), the CN may decay through single or multiple modes either by emission of light particles, LPs (evapora-

tion residues; Z≤2 and A ≤4) such as proton, neutron, alpha-particle or through emission of intermediate mass fragments (IMFs; 2≤Z≤10 and 5≤A≤20), heavy mass fragments (HMFs) and symmetric/asymmetric fission fragments. Although the fission phenomenon has been discovered several years back, it continues to remain a challenging task even today [38], and considerable efforts are required to understand its aspects by analyzing the collective participation of nucleons within deformed shapes of nuclear entities. For heavy deformed targets forming CN with mass A>200, the Coulomb repulsion ($\propto Z^2$) increases more rapidly than nuclear binding energy ($\propto$A) resulting into symmetric or asymmetric fission products. In the symmetric case, the mass distribution is centered around one mean value ($\approx$ A/2) whereas for asymmetric mass distribution, light and heavy fragments are observed, represented through a double-humped structure in the fission region. On the contrary for relatively lighter intermediate mass systems, light particles (LPs ; A_2≤4) emission is yet an important decay process and hence competition between LPs and fission fragments is observed. Further, for very light mass nuclei (lying in the range A_{CN}≤80), LPs form the dominant decay mode accompanied with small contribution of IMFs with almost negligible yield of fission fragments.

In recent past, the theoretical description of decay processes involving precise identification of CN residue have been employed which subsequently exhibit the LPs and fission dynamics using available statistical approaches. The emission of light particles is well described by Hauser Feshbech (HF) [11] statistical codes e.g., PACE [39] while the fission fragments emission in form of IMFs and HMFs has been studied using BUSCO code [40] or the Extended Hauser-Feshbach scission-point model [12]. Apart from these approaches, few other fission models [13], have also been used that are based on either the scission-point [41] or saddle-point configuration in the GEMINI code or the saddle-point transition-state model (TSM) [13, 14]. Also, analytical super asymmetric fission (ASAF)

model has been used for cluster decay and α-decay half-lives of superheavy nuclei [42]. However, in the present work, as an alternate to these models, the Dynamical Cluster-decay Model (DCM), has been applied to study the decay of nuclei varying from light to superheavy mass region. It is built on collective clusterization based non statistical approach, details of which are discussed in chapter 2. With reaction cross-section being the most important quantity of interest, a characteristic study of LPs and fission cross-sections has been carried out in the present work for a wide range of nuclei. The results obtained using DCM for the decay of heavy mass nuclei $^{278,286}112^{*}$, $^{213,215,217}Fr^{*}$ [18,19] and $^{201}Bi^{*}$ [20] are presented in chapters 3 and 5. The decay processes and dynamics observed in intermediate mass nuclei, $^{150,158}Tb^{*}$ [21] and $^{96}Tc^{*}$ [20], are discussed in chapters-4 and 5 and the decay of light mass $^{66}As^{*}$ [22] and $^{40}Ca^{*}$, $^{39}K^{*}$ nuclei [22] are covered in chapter-6.

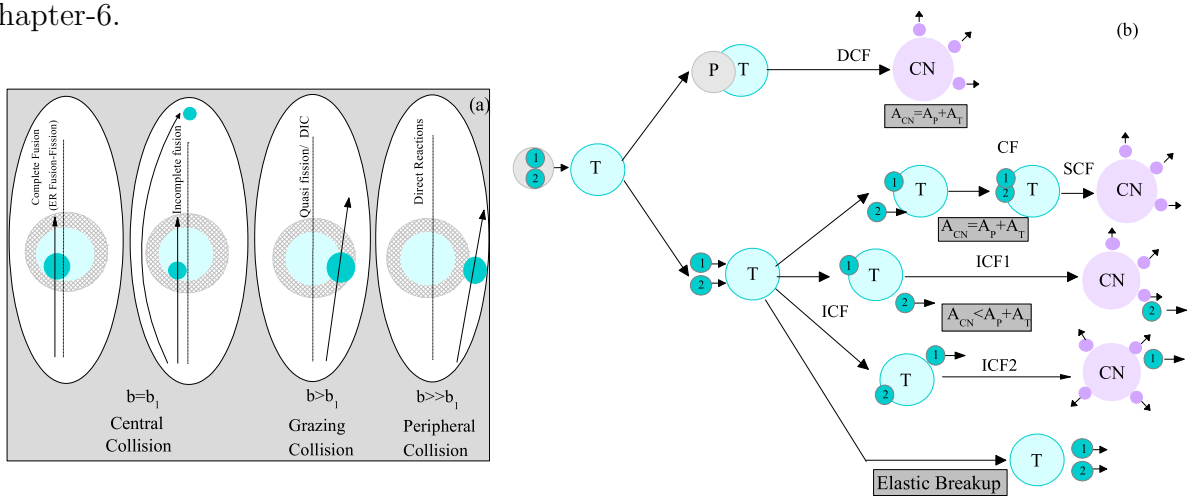

Figure 1.2 (a)Pictorial representation of collision trajectories observed during interaction of projectile with target nucleus in heavy ion reactions. (b) Various ways through which weakly bound projectile fuses with the target nucleus giving rise to complete fusion and incomplete fusion processes [35].

In order to vitalise our knowledge about HIRs, it becomes mandatory to analyze the mechanisms that play crucial role during and after the collision. The occurrence of these processes in reference to the trajectory of colliding reaction partners and impact parameter

(b) is represented in Fig.1.2 (a). Sketching the interaction potential and grading the trajectories on the basis of impact parameter, it may be observed that for central collisions with negligible or very small impact parameter, complete amalgamation of projectile and target nucleus takes place giving rise to direct complete fusion (DCF). However, for loosely bound nuclei, the barrier observed due to higher centrifugal potential prevents complete fusion of projectile with the target nucleus and gives rise to a different mechanism called incomplete fusion (ICF), which is discussed ahead. At relatively larger impact parameter, the collisions involving only glancing interaction between the two nuclei may result into the formation of nCN which may subsequently lead to mechanisms like quasi-fission (QF) and deep inelastic collision (DIC) (refer Sec.1.3). Besides this, at still large impact parameter for peripheral collisions, the process like elastic scattering comes into picture.

In reactions involving loosely bound nuclei, having low break-up threshold, the composite projectiles may break directly or sequentially, in early stages of the interaction under the influence of Coulomb and nuclear field of the target. Following breakup, the fusion of one or more fragments with the target nucleus may be observed, giving rise to incomplete fusion (ICF) or sequential fusion (SF) respectively, the former being the topic of interest in this thesis. The pictorial representation of the projectile break-up and modes of fusion is given in Fig.1.2 (b). In ICF, the light particle emitted from the projectile after break-up (also called spectator) goes uninteracted while the remanent nucleon cluster fuse with the target, giving rise to 'reduced' CN. It is also referred as break-up fusion, massive transfer, pre-compound emission or prompt emission of particles. The fraction of ICF is mainly correlated with the center-of-mass velocity and mass asymmetry in the reaction partners [43]. However in certain exceptional cases, ICF process has also been noticed for reactions involving tightly bound nuclei [44] having an impact on the complete fusion cross-sections.

From systematic analysis it has been observed that fusion of incident nuclei having high α-break-up threshold results in suppression of complete fusion and consequently the ICF contribution comes into picture. The angular momentum (ℓ) also plays a significant role in shaping the interaction trajectories which are useful in deciding the limit to complete fusion and onset of ICF [45]. With ℓ-states lower than the critical angular momentum, ℓ_{crit} the projectile fully transfers its momentum and complectly fuses with the target. On the other hand, for $\ell \geq \ell_{crit}$ the centrifugal potential dominates the attractive nuclear potential due to which the complete fusion of the projectile is hindered leading to ICF [46]. Thus investigating its effect in the form of centrifugal potential and hence the rotational energy is of great importance and relevance for overall understanding of nuclear dynamics involving loosely bound projectiles. In framework of DCM, the appropriate energy correction in reference to break-up of projectile and angular momentum distribution has been considered to study the relevant nuclear structure and dynamic aspects of ICF. The explicit analysis of ICF mechanism in reference to ^{201}Bi* and ^{96}Tc* [20] nuclei is carried out in chapter 5.

1.3 Non-Compound Nucleus Reactions

Interestingly, with persistent efforts giving rise to varying reaction conditions one seeks to understand the changing nature and mechanisms observed in collision of projectile and target nuclei over a wide range of incident energies. For many years, a reaction was assumed to be either direct process [47] occurring rapidly or a CN process which takes much longer time to obtain full statistical equilibrium. This sharp categorization turned inadequate when evidences for nCN processes were obtained having interaction time shorter than the CN lifetime but long enough for the exchange of mass or energy.

Perhaps the simplest quantitative difference between the CN and nCN mechanisms is the time of interaction. As an exception to CN, the nCN mechanism retains the history of its formation, thus bringing the entrance channel properties into picture. In such processes strong forces compete ferociously with complete fusion of projectile and the energy is redistributed only among few constituent nucleons. The nCN mechanisms like QF and DIC studied in the present work are discussed ahead.

The QF [48] process, is observed when interacting ions re-separate through large mass transfer into fission like fragments, similar to the entrance channel configuration. This may be attributed to the high fusion barrier as compared to projectile energy because of which the composite system decays in very small time scale (as compared to formation of equilibrated CN) in order to attain near mass symmetry. The QF occurs for more compact fission barrier as compared to the entrance channel contact configuration and is governed by dissipation of kinetic energy and mass transfer in the entrance channel. It is observed mostly in symmetric reactions, for cases where the mean fissility of reacting systems (X_m) exceeds 0.72, charge product (Z_1Z_2) exceeds 1600 and mass asymmetry is less than the Businaro-Gallone point. However, exceptions to each of these has also been observed [49]. The experimental signatures for QF are wider mass distribution, mean fragment mass, angle co-relation and fairly large fission fragment anisotropy. The deformation and orientation degrees of freedom also play a significant role as deformed targets with tip-to-tip collision may give rise to QF while, the side collisions may result into fusion-fission phenomenon [50]. Since the binary decay fragments obtained through fusion-fission and QF may overlap, distinguishing their contribution is a tedious job and requires dynamical model for discrete understanding. The presence of QF not only influences the CN formation and hence the ER cross section, but also inhibits the formation of superheavy elements [51]. The study of heavy and superheavy nuclei formed in symmetric

reactions are of great interest for understanding this nCN process. The DCM, having ability to study the decay of heavy mass nuclei has been applied to study the fission and QF contribution for the $^{213,215,217}Fr^{*}$, and $^{278,286}112^{*}$ nuclei, the results for which are presented in chapter 3.

Another nCN process considered in the study of nuclear reaction dynamics is DIC, where the projectile and the target nuclei stick together for sufficiently long time and involve substantial rearrangement of nucleons in the incoming channel. The interaction time for the composite system formed in DIC bridges the gap between CN and QF process. It is generally observed in reactions involving light mass nuclei, for partially damped waves near the grazing angle and with product masses similar to projectile and target mass. Since the composite system in DIC is not trapped in the pocket of the nucleus-nucleus potential, it is not characterized by the full momentum transfer. In the present work DCM has been applied to study the decay of light mass $^{40}Ca^{*}$,$^{39}K^{*}$ nuclei, showing contribution of DIC in addition to fusion-fission fragments and is discussed in Chapter 6.

In HIRs, the interplay between ion-ion potential (nuclear potential) and the frictional forces controlling damping of kinetic energies [52] and angular momentum decide whether fusion or faster decay may occur. To differentiate between the CN and the nCN processes is also a tedious task and thus the study of a composite nucleus is of great importance as it provides a comprehensive picture of the dynamics involved in a reaction. A schematic representation of the formation and characteristic decay paths of CN and nCN processes (QF and DIC) is depicted in Fig.1.3. It is evident that the equilibrated CN formation is not an immediate process and can be viewed as composite system proceeding through complete fusion in the pocket of potential. The long-lived, excited and rotating CN decays though the intermediate scission and saddle points into separated fragments. Contrarily, for ncN the composite system resides outside the pocket and lives for relatively small

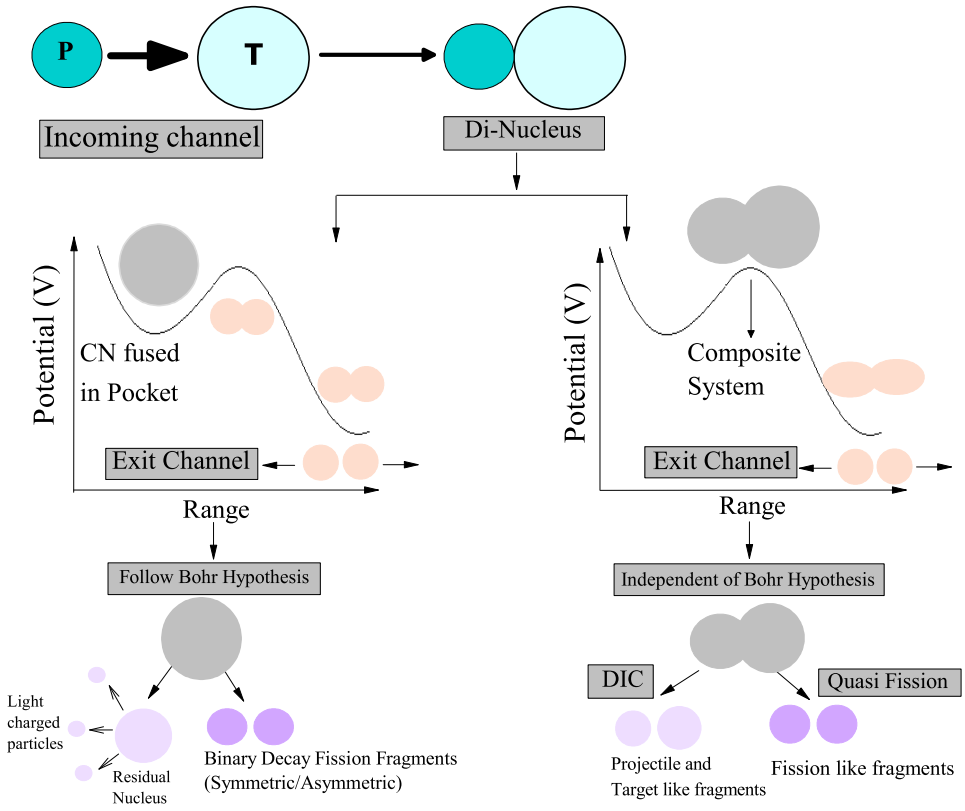

Figure 1.3 Different stages observed in formation and decay mechanisms for the reactions involving CN and nCN processes.

time, short enough for the formation of statistical equilibrium, thus retaining its formation path and re-separates after the exchange of energy or mass. The decay paths involved in HIRs are strongly influenced by the deformation and orientations degrees of freedom. For deep and enhanced understanding of reaction dynamics, these factors and their influence on the decay mechanism can not be neglected. Thus for adequate understanding of nuclear structure and related reaction dynamics one needs to include the static or dynamic deformations along with appropriate orientation degree of freedom, which have been successfully included in framework of DCM. It may be noted that for QF and DIC processes, the preformation probability is treated in a way different from CN mechanism. Moreover, for QF all the angular momentum states upto ℓ_{max} have been considered whereas for DIC only limiting values lying between ℓ_{crit} to ℓ_{max} have been taken into account.

1.4 Motivation of the present work

Every small step carried out and every effort done is quite crucial to progress our understanding of the nucleus, the existing matter and the universe as a whole. Horizon of human mind and of science is increased by solving puzzles posed by day to day experimentations. However, the experimental observations may be of no significant worth, if not substantiated theoretically. Thus, continuous efforts in experimental techniques and theoretical models have been carried out in order to expand our existing knowledge. In this thesis, the dynamical cluster-decay model (DCM) has been employed to study the CN and nCN decay mechanisms observed in nuclei lying in different mass regions of the periodic table. The DCM is based on well known quantum mechanical fragmentation theory (QMFT) [53, 54] and gives descent estimate of various decay products formed in HIRs. It is noteworthy that investigating the features of decay mechanisms observed through CN or nCN processes proves to be of immense help in growing our knowledge of nuclear structure, nuclear reaction and associated aspects. In framework of DCM, the decay in form of LPs, IMFs, HMFs and symmetric or asymmetric fragments have been studied for $^{278,286}112^{*}$, $^{213,215,217}Fr^{*}$, $^{201}Bi^{*}$,$^{150,158}Tb^{*}$,$^{96}Tc^{*}$,$^{66}As^{*}$,$^{40}Ca^{*}$ and $^{39}K^{*}$ nuclei. The work carried out in this thesis is attributed to the investigation of decay mechanisms under the influence of extreme conditions of temperature, excitation energy, deformations and orientations with concentration laid on (i)studying the structure effects caused by the iso-spin (N/Z) ratio (ii) role of angular momentum, effecting the moment of inertia and accountable for separating the CN and nCN contributions (iii) identifying the masses corresponding to given charge contributing towards the decay of peculiar light systems and (iv) studying the dynamics of reactions induced by neutron and proton halo nuclei. The present study sheds light on the theoretical aspects and signatures of various processes such as QF, DIC, ICF, in addition to the CN decay for the heavy, intermediate

and light mass region. The description of the mass-distribution and the potential energy surfaces play a significant role for overall analysis of reaction dynamics, details of which are discussed in chapter 2.

1.5 Organization of thesis

This thesis is organized in following way:

Chapter 2, provides the relevant details of the dynamical cluster decay model, DCM [16–26] which is based on the quantum mechanical (dynamical) fragmentation theory (QMFT) [53, 54]. In this chapter, the stationary state Schrödinger equation having Coulomb, proximity and centrifugal potentials as input, is solved to estimate the preformation probability of decaying fragments. Besides this, the detailed description of barrier penetrability P is discussed on the basis of WKB approach. The role of temperature and angular momentum effect, deformation and orientation degree of freedom is addressed wherever applicable. The relevant structural information and various other decay properties of the hot (excited) and rotating nuclei are addressed using collective cluterization approach. The application of DCM to CF, ICF and nCN processes is analyzed for a wide mass range of nuclear mass, details of which are discussed in the succeeding chapters.

In **Chapter 3**, the DCM is applied to attain a complete picture of decay cross-sections of the odd mass Fr isotopes. To extend the decay analysis of ^{18}O+^{197}Au $\rightarrow^{215}$Fr*, ER cross-sections are estimated using the systematics obtained from ^{19}F+ ^{194,198}Pt $\rightarrow^{213,217}$Fr* reactions. Also, the fission cross-section for the later are predicted at higher energies. Further the behavior of fission fragment anisotropies for the ^{213,217}Fr* isotopes are addressed using collective cluterization approach of DCM [18]. It is observed that the sticking (I_S) limit of moment of inertia is favorable to account for the decay cross-sections while for

the fission fragment anisotropies the non-sticking (I_{NS}) limit of moment of inertia is more suitable. Further, with the variation of fragmentation potential $V(\eta)$, preformation probability P_0 and decay barrier height for ^{215}Fr* nucleus formed in ^{19}F+^{196}Pt and ^{18}O+^{197}Au reaction channels, it is observed that the decay of ^{215}Fr* is independent of the choice of entrance channel. Apart from this, the ER and fission cross-sections are also predicted for ^{211}Fr* and ^{219}Fr* isotopes. In addition to this, the role of isospin (N/Z ratio of CN) and shell closure is explored for all the decaying Fr isotopes with mass number varying from A=211-219. The detailed analysis of temperature, angular momentum effects, preformation factor, and barrier modification, etc., is worked out in context of the reactions under investigation and the results are found in good agreement with the experimental observations [55].

Besides an exclusive analysis of Fr isotopes, DCM is also been applied to explore the effect of orientation degree of freedom for decay of superheavy isotopes, ^{278}112* and ^{286}112* [19]. The fission cross-sections are calculated for the use of hot (equatorial) compact and cold (polar) elongated orientations and it is observed that the calculated cross-sections match nicely with the experimental data using hot configuration but the same are overestimated for the use of cold orientation approach at deep sub-barrier region being more for neutron-deficient ^{278}112* nucleus, in agreement with experimental results [56].

After studying the decay mechanism of heavy mass nuclei, the dynamics of intermediate mass ^{150,158}Tb* nuclei formed in ^{6}Li +^{144,152}Sm reactions is explored in **Chapter 4**. In reference to recent experiments [57], DCM is applied to examine the role of static (β_2(0)) and dynamic (β_2(T)) quadrupole deformations along with the effect of hot (equatorial) compact and cold (polar) elongated orientations in the decay of ^{150,158}Tb* nuclei [21]. To look for the deformation and orientation effects, the variation of fragmentation potential, pre-formation probability, and barrier modification is studied. Also, the possible

role of shell effects of the decaying fragments is explored which suggests the involvement of some competing process in addition to the CN decay. The experimentally observed 28% suppression [57] in fusion cross-section for ^{158}Tb* nucleus is addressed through ICF process.

Chapter 5, deals with the application of DCM to reactions exhibiting complete and incomplete fusion processes observed in ^{20}Ne and ^{6}Li induced reactions [20] in reference to experimental work [58]. In the decay of ^{201}Bi* nucleus formed through complete fusion, the role of higher deformations is been observed by fitting the ER cross-section by considering spherical choice of fragmentation, with inclusion of quadrupole (β_2) deformations within optimum orientations and using deformation effects up to haxedecapole (β_2-β_4) within compact orientation approach. For the ICF process, the original projectile ^{20}Ne is segregated into four dominant channels, ^{4}He, ^{8}Be,^{14}N, ^{16}O and contribution through each of these channels is calculated by applying the necessary energy correction. The results are found to be in agreement with the systematics of Morgenstern et al. [45] that provides a correlation between fraction of ICF and center-of-mass velocity with mass asymmetry in the entrance channel. Further, to study the role of angular momentum (ℓ) in dynamics of ^{96}Tc* the role of sticking (I_S) and the non-sticking (I_{NS}) limit of moment of inertia is investigated with inclusion of quadrupole (β_2) deformation within optimum orientation approach. It is observed that sticking (I_S) limit is relatively more favorable at above barrier energies. Additionally, the role of ℓ is also observed in disentangling the contribution of CF and ICF processes. The contribution of CF has been calculated for all partial waves upto ℓ_{crit} while higher ℓ-values upto ℓ_{max} are considered for competing ICF process.

Chapter 6 converges the application of DCM to light mass nuclei $^{66}As^{*}$ formed in proton-halo ^{8}B induced reaction and ^{40}Ca*, ^{39}K* nuclei formed in ^{12}C+^{28}Si and ^{11}B+^{28}Si, ^{12}C+^{27}Al channels [22]. In reference to the measured fusion excitation functions [59] the

decay of $^{66}As^*$ in form of LPs, IMFs and fission fragments is studied for the use of spherical, quadrupole (β_2) and haxedecapole (β_2-β_4) deformations. The inclusion of deformations is shown to influence the decay path of $^{66}As^*$ nucleus as for spherical fragmentation, LPs seem to be dominant decay channel followed by IMFs at all energies across the barrier. However, with inclusion of deformations, IMFs dominate at below barrier energy and LPs at above barrier. Also the prediction of cross-sections is made at higher incident energies. Further, the decay of ^{40}Ca* and ^{39}K* nuclei is studied where the identification of complex fragments contributing towards the decay are identified using DCM in reference to the measured charge spectrum [60] by considering spherical choice of fragmentation.

Finally **Chapter 7** concludes the over all work of the thesis. Also the significance of this work and scope for its extension in future is discussed briefly.

Bibliography

[1] A. W. Steiner, M. Prakash, J. M. Lattimer, and P. J. Ellis, Phys. Rep. **411**, 325 (2005); M. Kutschera, Phys. Lett. B **340**, 1 (1994).

[2] H. Becquerel, C. Rendus **122**, 420 (1896).

[3] E. Rutherford, Philosophical Magazine **21**, 669 (1911); E. Rutherford, Philosophical Magazine **24**, 669 (1912);E. Rutherford, Philosophical Magazine **27**, 488 (1914).

[4] N. Bohr, and J.A. Wheeler, Phys. Rev. **56**, 426 (1939).

[5] M. G. Mayer, Phys. Rev. **75**, 1969 (1949); O. Haxel, D. Jensen, and H. E. Suess, Phys. Rev. **75**, 1766 (1949).

[6] V. M. Strutinsky, Nucl. Phys. A **95**, 420 (1967); V. M. Strutinsky, Nucl. Phys. A **122**, 1 (1968).

[7] A. K. Jain, et.al., Rev. Mod. Phys. **62**, 2 (1990).

[8] A. Bohr and B. R. Mottleson, Nuclear Structure Vol. II: Nuclear Deformations World Scientiific ISBN 9810239807 (1998).

[9] S. Weinberg, Rev. of Mod. Phys. **52**, 3 (1980).

[10] H. Yukawa, Proc. Phys. Math. Soc. Japan **17**, 48 (1935); L. Rosenfeld, *Nuclear Forces* published by Amsterdam/New York North-Holland/Interscience, (1948).

[11] W. Hauser, H. Feshbach, Phys. Rev. **87**, 366 (1952).

[12] T. Matsuse, C. Beck, R. Nouicer, and D. Mahboub, Phys. Rev. C **55**, 1380 (1997).

[13] S. J. Sanders, A. Szanto de Toledo, and C. Beck, Phys. Rep. **311**, 487 (1999).

[14] L. G. Moretto, Nucl. Phys. A **247**, 211 (1975); S. J. Sanders, D. G. Kovar, B. B. Back, C. Beck, D. J. Henderson, R. V. F. Janssens, T. F. Wang and B. D. Wilkins, Phys. Rev. C **40**, 2091 (1989); S. J. Sanders, Phys. Rev. C **44**, 2676 (1991).

[15] S.S. Malik and R.K. Gupta, Phys. Rev. C **39**, 1992 (1989); R.K. Gupta, edited by C. Beck , Clusters in nuclei, in Lecture Notes in Physics, **vol. 1** (818), p. 223 Springer-Verlag, Berlin, Heidelberg, (2010).

[16] R.K.Gupta, edited by W.Greiner and R.K.Gupta, Heavy Elements and Related New Phenomenon, **Vol.II**, World Scientific, Singapore, p.536,(Chapter14) (1999).

[17] R. K. Gupta, M. Balasubramaniam, R. Kumar, N. Singh, M. Manhas, and W. Greiner, J. Phys. G: Nucl. Part. Phys. **31**, 631 (2005);R. K. Gupta, M. Manhas, and W. Greiner, Phys. Rev. C **73**, 054307 (2006).

[18] G. Sawhney, G. Kaur, M. K. Sharma, and R. K. Gupta, Phys. Rev. C **88**, 034603 (2013).

[19] K. Sandhu, G. Kaur, and M. K. Sharma, Nucl. Phys. A **921**, 114 (2014).

[20] G. Kaur and M. K. Sharma, Nucl. Phys. A **884**, 36 (2012); G. Kaur, N. Grover, K. Sandhu, and M. K. Sharma, Nucl. Phys. A **927**, 232 (2014).

[21] G. Kaur and M. K. Sharma, Phys. Rev. C **87**, 044601 (2013).

[22] G. Kaur, D. Jain, R. Kumar, M. K. Sharma, Nucl. Phys. A **916**, 260 (2013); G. Kaur, and M. K. Sharma, Int.J.Mod.Phys.E **23**, 10 (2014).

[23] B. B. Singh, G. Kaur, M. K. Sharma, and R. K. Gupta, Proceedings of DAE symposium on nuclear physics, Andhra University, (Vishakhapatnam), Vol. **56**, 514 (2011); *ibid* Proceedings of DAE symposium nuclear physics, Delhi University, Delhi, Vol. **57**, 550 (2012) available on line at http://www.sympnp.org/proceedings.

[24] M. K. Sharma and G. Kaur, Pramana- J. of Phys. **82**, 5, pp 919 (2014); G. Kaur and M. K. Sharma, AIP Conference Proceedings **1524**, 155 (2013).

[25] B.B.Singh,M.K.Sharma, R.K.Gupta, and W.Greiner,Int.J.Mod.Phys.E **15**, 699 (2006); B.B.Singh, M.K.Sharma, and R.K.Gupta, Phys.Rev.C **77**, 054613 (2008).

[26] G.Sawhney, M.K.Sharma, Eur.Phys.J.A **48**, 57 (2012); Gudveen Sawhney, R. Kumar, and M. K. Sharma, Phys.Rev.C **86**, 034613 (2012).

[27] J. Cugnon and C. Volant, Z. Phys. A **334**, 435 (1989); J. Cugnon, D. Kinet, and J. Vandermeulen, Nucl. Phys. A **379** , 553 (1982); J. Cugnon, Phys. Rev. C **22**, 1885 (1980);J. Aichelin, Phys. Rep. Vol **202**, pg- 233-360 (1991).

[28] J. W. Negele, Rev. Mod. Phys. **54**, 913 (1982).

[29] I.Slaus, Y.Akaishi and H.Tanaka, Phys. Rep. **173**, 257 (1989);G. A. Miller, M. K. Nefkens, and I. Slaus, Phys. Rep. **194**, 1 (1990).

[30] J. M. Lattimer, M. Prakash, Phys. Rep. **333**, 121 (2000); J. M. Lattimer et. al. Astrophys. J. **550**, 426 (2001);M. Prakash et al., Phys. Rep. **280**, 1 (1997). S. Kubis and M. Kutschetra, Nucl. Phys. A 720, 189 (2003).

[31] S.N. Ghoshal, Phys. Rev. **80**, 939 (1950);J.R. Grover,J. Gilat, Phys. Rev. **157**, 802 (1967); J. M. DAuria, et.al., Phys. Rev. **174**, 1409 (1968); P. Wong, P. Daly, N.T.Porile, Nucl. Phys. A **151**, 549 (1970); D. M. Montgomery, N. T.Porile, Phys.

Rev. C **2**, 595 (1970);L. C. Vaz, C. C. Lu, J. R. Huizenga,Phys. Rev. C **5**, 463 (1972);J. Bisplinghoff, J. Ernst, R. Löhr, T. Mayer-Kuckuk, P. Meyer, Nucl. Phys. A **269**, 147 (1976).

[32] V. F. Weisskopf, P. H. Ewing, Phys. Rev. **57**, 472 (1940).

[33] P.E. Hodgsona, E. Betak, Phys. Rep. **374**, 1 (2003).

[34] I. Tanihata et al., Phys. Rev. Lett. **55**, 2676 (1985); I. Tanihata et al., Phys. Lett. B **160**, 380 (1985).

[35] L.F. Cantoa, P.R.S. Gomes, R. Donangelo, and M.S. Husseinc, Phys. Rep. **424**, 1 (2006).

[36] N. Takigawa, H. Sagawa, Phys. Lett. B **265**, 23 (1991).

[37] P.R.S. Gomes, et.al., Nucl. Instrum. Methods Phys. Res. A **280**, 395 (1989); P.R.S. Gomes, et.al., Phys. Rev. C **49**, 245 (1994);P.R.S. Gomes, et.al., Braz. J. Phys. **35**, 902 (2005).

[38] O.Hahn, F.Strassmann, Naturewissenchaften **27**, 203 (1939); L.Meitner, O. R. Frisch, Nature **143**, 239 (1939); R. Vandenbosch, Nucl. Phys. A **502** lc (1989); D. Hilscher, I.I. Gontchar and H. Rossner, Phys. Atomic Nuclei **57**, 1187 (1994).

[39] A. Gavron, Phys. Rev. C **21**, 230 (1980).

[40] J. Gomez del Campo, R. L. Auble, J. R. Beene, M. L. Halbert, H. J. Kim, A. DOnofrio, and J. L. Charvet, Phys. Rev. C **43**, 2689 (1991); Phys. Rev. Lett. **61**, 290 (1988).

[41] R. J. Charity, M. A. McMahan, G. J.Wozniak, R. J. McDonald, L. G. Moretto, D. G. Sarantites, L. G. Sobotka, G. Guarino, A. Pantaleo, L. Fiore, A. Gobbi, and K.D. Hildenbrand, Nucl. Phys. A **483**, 371 (1988).

[42] D.N. Poenaru,R.A. Gherghescu,W. Greiner, Rom. Journ. of Phys. **58**, 9 1157 (2013).

[43] S. Pirrone, S.Aiello, N.Arena, Seb.Cavallaro, S.Femino et.al., Phys. Rev. C **55**, 2482 (1997).

[44] A. Mukherjee, S. Roy, M.K. Pradhan, M.Saha Sarkar et.al., Phys. Lett. B **636**, 91 (2006).

[45] H. Morgenstern, W. Bohne, W.Galster, K.Grabisch, and A.Kyaowski, Phys. Rev. Lett **52**, 1104 (1984); H. Morgenstern, et al., Z. Phys. A **313**, 39 (1983).

[46] P. P. Singh *et. al.*, Phys. Rev. C **80**, 064603 (2009).

[47] S.T.Butler, Phys. Rev. 80, 1095 (1950); S.T.Butler, Proc. R.Soc. A **208**, 559 (1950); G. R. Satchler, J. A. Spiers, Proc. Phys. Soc. London A **65**, 980 (1952); N. Austern, S. T.Butler, H. McManus,Phys. Rev. **92**, 350 (1953). ; J.R. Oppenheimer, M. Phillips, Phys. Rev. **48**, 500 (1935).

[48] B.B. Back, et.al., Phys. Rev. C **32**, 195 (1985); Phys. Rev. C **33**, 385 (1986); C. Ngo, Prog. Part. Nucl. Phys. **16**, 139 (1986); W.J. Swiatecki, Phys. Ser. **24**, 113 (1981); S. Bjornholm and W.J. Swiatecki, Nucl. Phys. A **391**, 471 (1982); W.Q. Shen, et.al., Phys. Rev. C **36**, 115 (1987); J. Toke, et.al., Nucl. Phys. A **440**, 327 (1985);J. P. Blocki et al., Nucl. Phys. A **459**, 145 (1986); P. Armbruster, Annu. Rev. Nucl. Part. Sci. **50**, 411 (2000).

[49] A. Saxena, et.al., Phys. Rev. C **49**, 932 (1994); L. M. Pant, et.al., Phy. Rev. C **54**, 2037 (1996); T. K. Ghosh et al., Phys. Rev. C **79**, 054607 (2009); R. G. Thomas

et al., Phys. Rev. C **77**, 034610 (2008); E. Prasad et al., Phys. Rev. C **81**, 054608 (2010); G. N. Knyazheva et al., Phys. Rev. C **75**, 064602 (2007).

[50] D.J. Hinde, M. Dasgupta, J.R. Leigh, J.P. Lestone, J.C. Mein, C.R. Morton, J.O. Newton, and H. Timmers, Phys. Rev. Lett. **74**, 1295 (1995).

[51] E. Prasad,K. M. Varier, N. Madhavan et.al., Phys. Rev. C **84**, 064606 (2011).

[52] V.V. Volkov, Phys. Rep. **44**, 93 (1978); U.W. Schroeder, J.R. Huizenga, in: D.A. Bromley (Ed.), Treatise on Heavy Ion Science, Plenum Press, New York, p. 115 (1984).

[53] J. Maruhn and W. Greiner, Phys. Rev. Lett. **32**, 548 (1974).

[54] R. K. Gupta, W. Scheid, and W. Greiner, Phys. Rev. Lett. **35**, 353 (1975).

[55] K. Mahata, S. Kailas, A. Shrivastava, A. Chatterjee, P. Singh, S. Santra, and B. S. Tomar, Phys. Rev. C **65**, 034613 (2002);V. Singh, B. R. Behera, M. Kaur, A. Jhingan, P. Sugathan, D. Siwal, M. Oswal, S. Goyal, K. P. Singh, A. Saxena, and S. Kailas, in Proceedings of the Department of Atomic Energy Symp. on Nucl. Phys. **57**, 400 (2012).

[56] K. Nishio, S. Mitsuoka, I. Nishinaka, H. Makii, *et.al.*, Phys. Rev. C **86**, 034608 (2012).

[57] P. K. Rath, *et. al.*, Nucl. Phys. A **874**, 14 (2012);P. K. Rath, S. Santra, N. L. Singh, R. Tripathi, *et.al.*, Phys. Rev. C **79**, 051601(R) (2009)

[58] R.Tripathi , K.Sudarshan, A. Goswami, R. Guin, and A.V. Reddy, Phys.Rev. C **74**, 014610 (2006);H. Kumawat, V. Jha, V. V. Parkar, B. J. Roy, *et.al.*, Phys. Rev. C **86**, 024607 (2012).

[59] E. F. Aguilera *et al.,* Phys. Rev. Lett. **107**, 092701 (2011).

[60] S. Kundu, C. Bhattacharya, K. Banerjee, T. K. Rana, et al., Phys. Rev. C **85**, 064607 (2012).

Chapter 2

Methodology

2.1 Introduction

The detailed study and interpretation of various decay processes proves to be of tremendous help in understanding the nuclear structure, reaction dynamics, underlying nuclear forces and in expanding the applications of nuclear physics from nucleosynthesis to reactor science. In order to attain a clear picture of the decay mechanisms and associated features such as energy distribution, potential energy surfaces, mass distribution etc,. one needs to understand the dynamical evolution of incoming and outgoing channels. A complete description of decay processes involved and the fragments obtained through decay of hot and rotating composite system, requires a comprehensive dynamical study of nuclear reactions using a theoretical approach where the numerical convergence of the experimental observations may be obtained through reliable computing. Interminable attempts have been made through different groups around the globe, to understand the decay properties using various theoretical approaches such as, the statistical models for examining the decay patterns of compound nuclei formed in heavy ion reactions. However, with time some competing non-statistical approaches have also been implied to study the dynamics

of a nuclear system. In the present work, the decay mechanisms and related aspects have been studied using the collective clusterization approach, which has an advantage over the available competing statistical models as it treats all the decay precesses on equal footing as collective mass motion of preformed fragments or clusters through the interaction barrier.

For the study executed in this thesis, the dynamical cluster decay model (DCM) [1–13], based on the well known Quantum Mechanical Fragmentation Theory, (QMFT) [14–21] has been applied to numerous nuclear systems pertaining from heavy to light mass region spread over a wide range of incident center-of-mass (c.m.) energies, across the Coulomb barrier. It is worth mentioning that QMFT (based on the two center shell model), is a unified description of two body channel heavy ion collisions, used as an average two body potential in Strutinsky macro-microscopic method [22]. Interestingly, it is the only theory, given antecedent to experiments, that considers the fragments to be pre-born prior to the decay of the compound nucleus thus bringing out the applicability of the quantum concept of probability in addition to the role of shell effects in formation and decay of nuclear systems.

The dynamical cluster decay model (DCM), formulated using QMFT is discussed in Sec.2.2, followed by the stationary state Schrödinger wave equation in Sec.2.3. The fragmentation potential used as input to Schrödinger equation is presented in Sec.2.4. Further, the preformation probability P_0 obtained as solution to Schrödinger equation and the penetration probability P are explained in Sec.2.5 and 2.6 respectively. The barrier modification, an inbuilt feature of DCM is explained in Sec.2.7. Lastly, the application of DCM to incomplete fusion and non-compound nucleus is discussed in Sec.2.8.

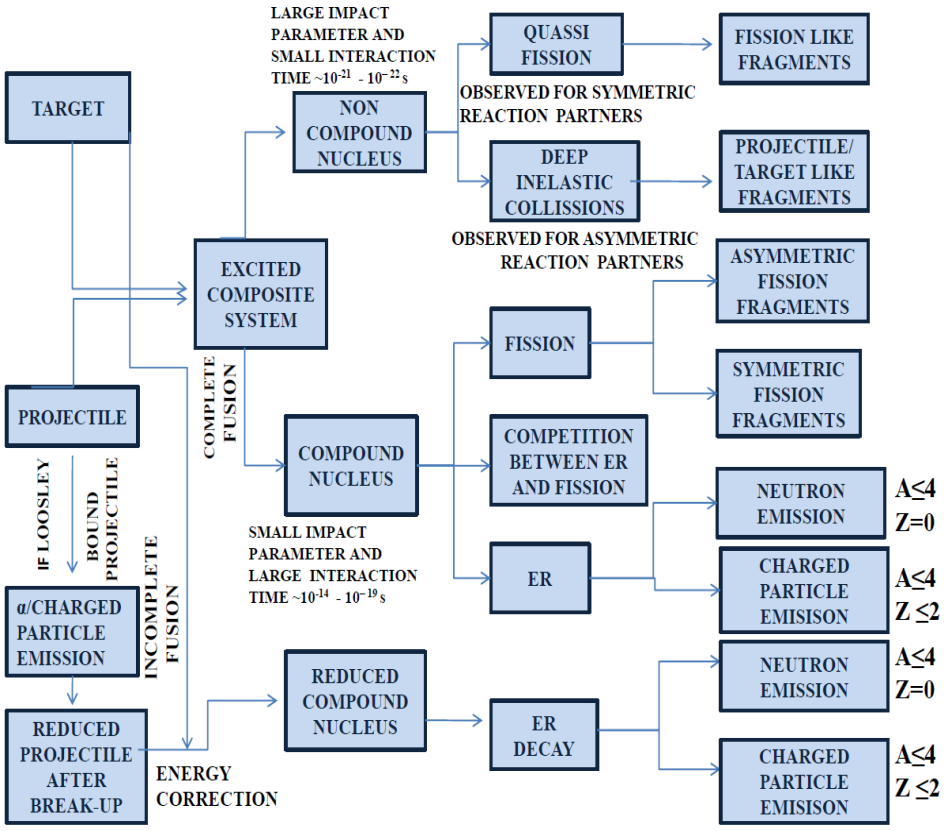

Figure 2.1 A schematic representation of various decay processes observed in low energy heavy ion reactions studied in framework of dynamical cluster-decay model.

2.2 The Dynamical Cluster-decay Model Framed Using Quantum Mechanical Fragmentation Theory

The dynamical cluster decay model (DCM) [1–13], has been successfully applied to explore the decay properties of a large number of hot and rotating (i.e. temperature $T\neq0$ and angular momentum $\ell\neq0$) nuclear systems. The emission of light particles (LPs; Z$\leq$2 and A $\leq$4), intermediate mass fragments (IMFs; 2$\leq$Z$\leq$10 and 5$\leq A\leq$20), heavy mass fragments (HMFs) and symmetric/asymmetric fission fragments have been studied through DCM, where deformation and orientation degrees of freedom is duly incorporated. A schematic

representation of various decay processes studied through DCM is shown in Fig. 2.1. Starting from the left, the figure shows projectile and target nuclei which completely fuse together to form a composite system in excited state. For the reactions with small impact parameter of incoming cannel and large interaction time, the composite system equilibrates in all degrees of freedom, giving rise to an equilibrated compound nucleus (CN). On the other hand, for reactions with large impact parameter and small interaction time, a non-compound nucleus (nCN) is formed. Depending upon the reaction conditions and energy involved the nCN is observed in various processes such quasi-fission (QF) and deep inelastic collision (DIC). In this thesis, DCM is adequately applied to study the decay of both CN and nCN mechanisms in the form of evaporation residues and fission fragments for the decay of heavy, intermediate and light mass nuclei. However, for reactions involving loosely bound nuclei, the emission of α/charged particle from the projectile nucleus before interaction with the target nucleus is observed. Following this, the reduced projectile obtained after break-up, fuses with the target nucleus giving rise to incomplete fusion (ICF) process and is represented through lower blocks in the figure. The decay of reduced CN formed via ICF is studied using DCM by applying relevant energy correction which is discussed in Sec.2.8.

The DCM is based on the quantum mechanical (or dynamical) fragmentation theory [14–21] which is worked out in terms of following collective variables:

(i)The relative separation coordinate R between the two nuclei or fragments (or, equivalently, the length parameter $\lambda = L/2R_0$, where L is length and R_0 is radius of an equivalent spherical nucleus).

(ii) The deformation co-ordinates $\beta_{\lambda i}$ (λ=2,3,4... and i=1,2) of the colliding nuclei.

(iii) The orientation degrees of freedom $\theta_i (i = 1, 2)$ of the deformed nuclei.

(iv)The azimuthal angle ϕ between the principal planes of the two colliding nuclei.

(v)The neck parameter ε, defined by the ratio $\varepsilon = E_0/E'$ for the interaction region $R < R_1 + R_2$ (R_i (i=1, 2) is the radius of the two nuclei). Here E_0 is the actual height of the barrier and E' is fixed barrier of the two center oscillator. A broad neck formation is represented as $\epsilon = 0$ whereas, $\epsilon = 1$ shows that the neck is fully squeezed in, corresponding to the asymptotic region ($R > R_1 + R_2$).

(vi) Mass and charge fragmentation co-ordinates [14, 15, 20] which for the two body channels with separated nuclei (fragments) are defined by the mass, charge and neutron asymmetry [15] coordinates as

$$\eta_A = \frac{A_1 - A_2}{A}; \qquad \eta_Z = \frac{Z_1 - Z_2}{Z}; \qquad \eta_N = \frac{N_1 - N_2}{N} \tag{2.1}$$

Here $A = A_1 + A_2$, $Z = Z_1 + Z_2$, $N = N_1 + N_2$ are respectively the mass number, charge and neutron numbers of the compound system while A_i, Z_i and $N_i (i = 1, 2)$ correspond to the mass, charge and neutron number of two fragments. However, it is sufficient to treat only two of them as dynamical co-ordinates since they are related as

$$\eta = \frac{Z}{A}\eta_Z + \frac{N}{A}\eta_N \tag{2.2}$$

The η_Z and η_N coordinates give the associated charge and neutron distribution effects. The limiting values of η are $0 \leq |\eta| \leq 1$ and thus allows unified description of a few-nucleon, multi-nucleon (cluster) transfer, large-mass transfer, the complete fusion ($|\eta| = 1$) of nuclei and the symmetric ($\eta = 0$), asymmetric and super-asymmetric fission of a compound nucleus.

In DCM, the co-ordinates η and R of fragmentation theory characterize, respectively,

(i) the nucleon-division (or exchange) between outgoing fragments, and

(ii) the transfer of kinetic energy of incident channel ($E_{c.m.}$) to internal excitation (total excitation or total kinetic energy, TXE or TKE) of the outgoing channel.

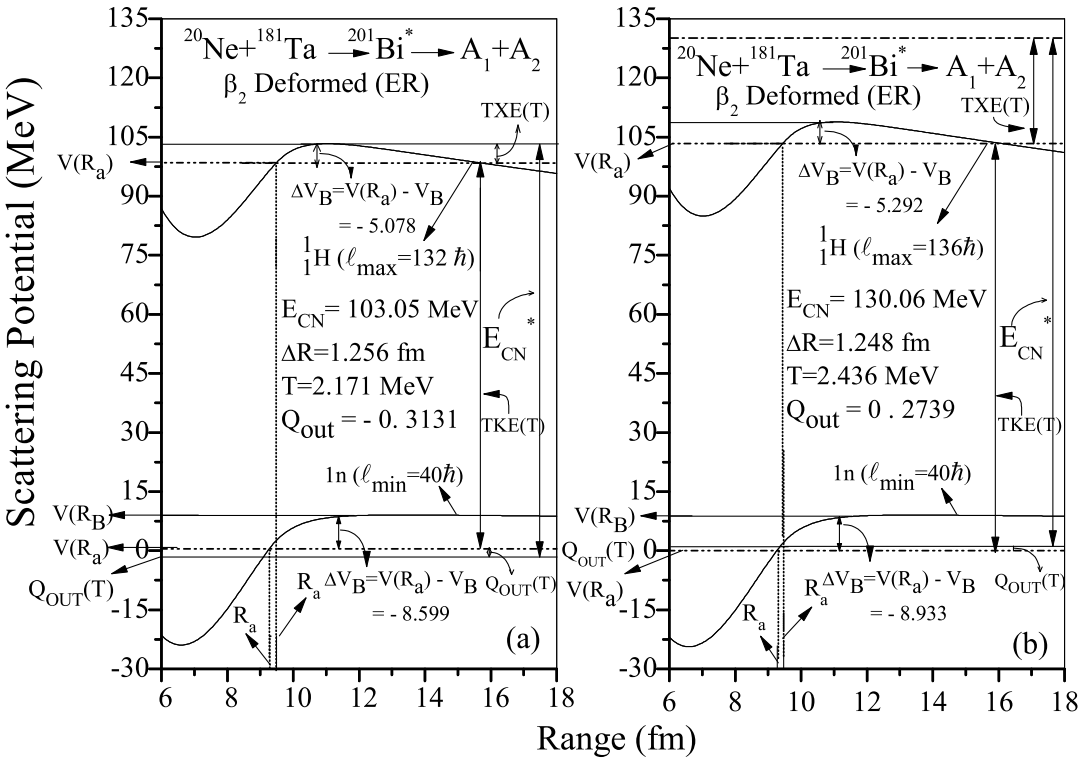

Figure 2.2 (a) The variation of scattering potential as a function of range (R) for the decay of $^{201}Bi^*$ system for (a) negative Q_{out} (b) positive Q_{out}.

The energy transfer for a negative Q_{out} (see. Fig.2.2a) is expressed as

$$E^*_{CN} =\mid Q_{out} \mid + TKE(T) + TXE(T) \tag{2.3}$$

For a positive Q_{out} (see Fig. 2.2b), the Eq. (2.3) is written as

$$E^*_{CN} + Q_{out} = TKE(T) + TXE(T) \tag{2.4}$$

The excitation energy, E^*_{CN}=$E_{c.m.}$ + Q_{in} of the compound nucleus is related to the temperature T (in MeV) through a semi-empirical statistical relation as:

$$E^*_{CN} = aT^2 - T \tag{2.5}$$

where a = A/9 to A/11 depending on the mass of the compound nucleus. It may be noted that Q_{in} is the entrance channel Q-value given by $B_1 + B_2 - B_{CN}$ where B's are the binding energies, and can be positive or negative and hence could be accordingly added or subtracted, depending on the nature and energy of target projectile combination.

Using the decoupled approximation to η- and R-motions (discussed in Sec.2.3), DCM defines the decay cross-section, in terms of partial waves, as

$$\sigma = \sum_{\ell=0}^{\ell_{max}} \sigma_\ell = \frac{\pi}{k^2} \sum_{\ell=0}^{\ell_{max}} (2\ell+1) P_0 P; \qquad k = \sqrt{\frac{2\mu E_{c.m.}}{\hbar^2}} \tag{2.6}$$

Here the preformation probability (P_0) refers to η-motion and the penetrability (P) to R-motion. Apparently, for ℓ=0 (s-wave) $\sigma_0 = \frac{\pi}{k^2} P_0 P$, which is an equivalent of decay constant $\lambda = \nu_0 P_0 P$ (or decay half-life $\mathrm{T}_{1/2} = ln2/\lambda$) with ν_0 as the barrier assault frequency. In other words, σ_0 and λ differ through a constant only.

It is worth mentioning that, DCM works as a two step model, where the first phase involves pre-formation of the fragments or clusters in the parent nucleus, followed by penetration of fragments through the barrier in the second phase. A significant information about the nuclear structure properties at compound nucleus state enters the model via quantum mechanical preformation probability P_0 (also known as the spectroscopic factors) of the decaying fragments or clusters formed in the mother nucleus. It gives relative probability of all channels, through which an excited compound nucleus can decay and explains the emission of evaporation residue (ER), intermediate mass fragments (IMF), heavy mass fragments (HMF), symmetric and asymmetric fission fragments (FF) from the excited compound nucleus. The preformation probability is calculated by solving stationary Schrödinger equation in mass fragmentation coordinate. The procedure of calculating preformation probability based on solution of Schrodinger equation is discussed in Sec.2.3

2.3 Stationary State Schrödinger Wave Equation

In terms of the collective coordinates of QMFT, the Hamiltonian can be written as

$$H = K(\mathbf{R}, \beta, \varepsilon, \eta, \eta_Z; \dot{\mathbf{R}}, \dot{\beta}, \dot{\varepsilon}, \dot{\eta}, \dot{\eta}_Z) + V(\mathbf{R}, \beta, \varepsilon, \eta, \eta_Z). \tag{2.7}$$

Here K, V refer to kinetic energy, potential energy respectively and β stands for $\beta_{\lambda 1}$ and $\beta_{\lambda 2}$; λ=2,3,4.... For the potential $V(\eta, \eta_Z, R)$, minimized in the η_Z co-ordinate, Schrödinger wave equation in terms of mass parameters η and relative separation co-ordinate R can be written as:

$$H(\eta, R)\psi(\eta, R) = E(\eta, R)\psi(\eta, R) \tag{2.8}$$

with the Hamiltonian,

$$H(\eta, R) = K(\eta) + K(R) + K(\eta, R) + V(\eta) + V(R) + V(\eta, R) \tag{2.9}$$

The coupling term of the kinetic energy $K(\eta, R)$, proportional to $\frac{\partial^2}{\partial\eta\partial R}$, is neglected here, since the coupled cranking masses are very small [14, 15], ($\mathrm{B}_{R\eta} \ll (B_{RR}B_{\eta\eta})^{1/2}$ and $\mathrm{B}_{R\eta_Z} \ll (B_{RR}B_{\eta_Z\eta_Z})^{1/2}$). Same is true for the coupling term of potential energy $V(\eta, R)$.

Therefore, in a decoupled approximation [21], the Schrödinger equation (2.8) can be solved for which the Hamiltonian takes the form:

$$H = -\frac{\hbar^2}{2\sqrt{B_{\eta\eta}}}\frac{\partial}{\partial\eta}\frac{1}{\sqrt{B_{\eta\eta}}}\frac{\partial}{\partial\eta} - \frac{\hbar^2}{2\sqrt{B_{RR}}}\frac{\partial}{\partial R}\frac{1}{\sqrt{B_{RR}}}\frac{\partial}{\partial R} + V(\eta) + V(R) \tag{2.10}$$

For exploring the static properties of nuclear system the potential energy alone is sufficient, however, in the dynamical fragmentation theory the potential energy surfaces and the mass parameters defining kinetic energy both form an essential tool in describing the nuclear dynamics. The mass parameters B_{ij}, defining the kinetic energy term K in the above Eq. (2.10) are either the cranking masses calculated consistently using the Asymmetric Two-Center Shell Model ($ATCSM$) or the classical hydrodynamical masses of Kröger and Scheid model [23] based on the hydrodynamical flow, which are shown to have good agreement with microscopic cranking calculations. For decoupled Hamiltonian (shown in 2.10), Schrödinger wave equation (Eq. 2.8) can be separated for the two co-ordinates η and R as follows,

$$\left[-\frac{\hbar^2}{2\sqrt{B_{\eta\eta}}}\frac{\partial}{\partial\eta}\frac{1}{\sqrt{B_{\eta\eta}}}\frac{\partial}{\partial\eta}+V(\eta)\right]\psi^{\nu}(\eta)=E^{\nu}_{\eta}\psi^{\nu}(\eta) \tag{2.11}$$

and

$$\left[-\frac{\hbar^2}{2\sqrt{B_{RR}}}\frac{\partial}{\partial R}\frac{1}{\sqrt{B_{RR}}}\frac{\partial}{\partial R}+V(R)\right]\psi^{\nu}(R)=E^{\nu}_{R}\psi^{\nu}(R) \tag{2.12}$$

with

$$\psi(\eta,R)=\psi(\eta)\psi(R) \qquad and \qquad E=E_{\eta}+E_{R} \tag{2.13}$$

The states $\psi^{\nu}(\eta)$ are the vibrational states in the potential $V(\eta)$ and are labelled by the quantum numbers ν=0,1,2,.. etc. The calculations in this thesis have been carried out using Eq. (2.11) in η co-ordinate whose potential energy component in form of fragmentation potential is discussed ahead.

2.4 The Fragmentation Potential $V(\eta)$

The temperature dependent collective potential energy or the fragmentation potential $V(\eta,R,T)$, appearing in Eq. (2.11), is calculated as,

$$\begin{aligned} V(\eta,R,T) &= -\sum_{i=1}^{2}B_i(A_i,Z_i,\beta_{\lambda i},T)+V_c(R,Z_i,\beta_{\lambda i},\theta_i,\phi,T) \\ &+ V_p(R,A_i,\beta_{\lambda i},\theta_i,\phi,T)+V_{\ell}(R,A_i,\beta_{\lambda i},\theta_i,\phi,T) \end{aligned} \tag{2.14}$$

The charges Z_i are fixed by minimizing the potential V(η) in the η_Z coordinate at each η-value. It is evident from this equation that DCM duly incorporates the deformation (β) and orientation (θ) degrees of freedom which are highly desirable for comprehensive understanding of structure and related dynamics of deformed nuclei having extreme shapes with higher multi-pole deformations (λ= 2, 3, 4). Deformed nuclei can be oriented in same plane (coplanar) or in different plane (non-coplanar), however the present study is confined to coplanar orientation only. Fig. 2.3 shows a schematic configuration of two

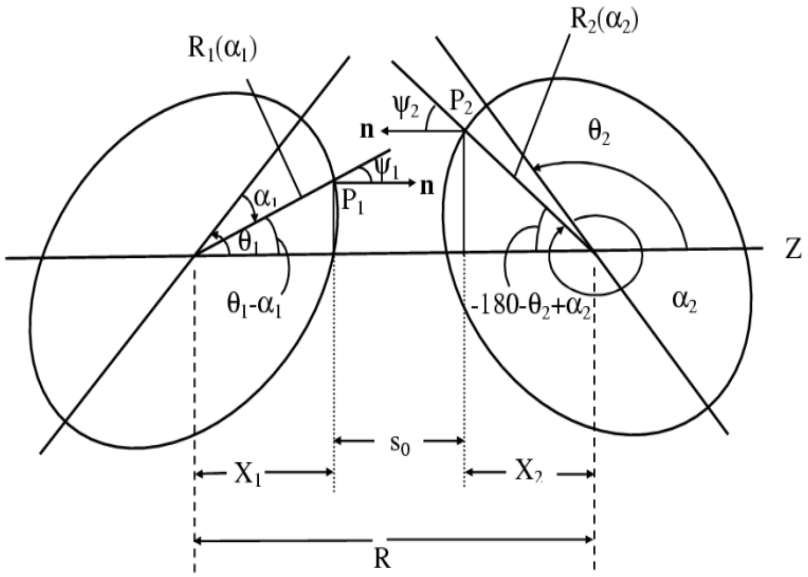

Figure 2.3 Illustration of two coplanar, axially symmetric deformed and oriented nuclei for various θ_1 and θ_2 values lying in range 0^0 to 180^0 [24]. The θ's are measured in anti-clockwise direction from the colliding axis and the angle α's in clockwise direction from the symmetry axis.

coplanar ($\phi = 0^0$), axially symmetric deformed and oriented nuclei. The angle between the symmetry axis and the axis of collision is defined as angle of orientation, θ_i and is measured in anti-clockwise direction from the axis of collision. The values of θ_1 and θ_2 vary from 0^0 to 180^0. While α_i is the angle that radius vector $R_i(\alpha_i)$ of the colliding nuclei makes with symmetry axis and is measured in clockwise direction from the symmetry axis of the nuclei.

For consideration of deformed and oriented reaction product, the fragmentation potential $V(\eta)$, is calculated at a fixed distance $R = R_1 + R_2 + \Delta R$, with

$$R_i(\alpha_i, T) = R_{0i}(T)[1 + \sum_{\lambda} \beta_{\lambda i} Y_{\lambda}^{(0)}(\alpha_i)] \tag{2.15}$$

and

$$R_{0i}(T) = [1.28A_i^{1/3} - 0.76 + 0.8A_i^{-1/3}] \times (1 + 0.0007T^2) \tag{2.16}$$

In the Eq. (2.14), B_i's (i=1,2) are binding energies of the two nuclei, taken from the experimental data of Audi-Wapstra [25]. Wherever the experimental B's are not

available, the theoretical binding energies of Möller *et al.* [26] are used. Note that within the Strutinsky renormalization procedure [22], the macroscopic (liquid drop) and the microscopic (shell correction) parts are contained, which allow us to define the binding energy (B) of a nucleus at temperature (T) as the sum of liquid drop energy $V_{LDM}(T)$ and shell correction $\delta U(T)$ i.e

$$B(T) = V_{LDM}(T) + \delta U exp\left(- \frac{T^2}{{T_0}^2} \right) \tag{2.17}$$

The T dependent liquid drop part of the binding energy $V_{LDM}(T)$ is taken from Davidson *et al.* [27], based on the semi-empirical mass formula of Seeger [28], as

$$\begin{aligned} V_{LDM}(A,Z,T) &= \alpha(T)A + \beta(T)A^{\frac{2}{3}} + \left(\gamma(T) - \frac{\eta(T)}{A^{\frac{1}{3}}}\right)\left(\frac{I^2 + 2 \mid I \mid}{A}\right) \\ &\quad + \frac{Z^2}{R_0(T)A^{\frac{1}{3}}}\left(1 - \frac{0.7636}{Z^{\frac{2}{3}}} - \frac{2.29}{[R_0(T)A^{\frac{1}{3}}]^2}\right) + \delta(T)\frac{f(Z,A)}{A^{\frac{3}{4}}}, \end{aligned} \tag{2.18}$$

For $T = 0$, Seeger [28] obtained the constants, by fitting all even-even nuclei and 488 odd-A nuclei available at that time, as $\alpha(0) = -16.11\text{MeV}, \beta(0) = 20.21\text{MeV}$, $\gamma(0) = 20.65\text{MeV}, \eta(0) = 48.00\text{MeV}$ with the pairing energy $\delta(0) = 33.0\text{MeV}$ [29]. For large amount of data available now on ground-state binding energies, these constants of $V_{LDM}(T = 0)$ are re-fitted to get the experimental binding energies for Audi Wapstra Tables of 1995 [1,2,30] and 2003 [3,25] where shell corrections are determined from Myers and Swiatecki [31]. The T-dependence in the constants of Eq. (2.18) is obtained from Fig.1 of Davidson et al. [27], achieved by fitting to the canonical ensemble average of the excitation energy of over 300 nuclei for T$\leq$4 MeV, extrapolated linearly for higher temperatures.

At higher energies, the main contribution of binding strength comes from the liquid

drop part as the shell corrections in Eq. (2.17) are considered to vanish exponentially for higher excitation energies (note that T_0=1.5 MeV). The shell corrections play an important role in determining nuclear strength or equivalently nuclear masses because the smooth liquid drop formula shows large deviation with respect to the experimental masses. In general, the microscopic shell correction, along with the liquid drop part, give a proper description of the binding energy of the nucleus. However, there are still some open questions in the light mass region because the shell model is not adequately established for such nuclei. For this reason, the macro-microscopic calculations of Möller *et al.* [26] are tabulated for $Z \geq 8$ only. Alternatively, one can use the empirical shell correction method of Myers-Swiatecki [31] which again is not satisfactory for light nuclei ($Z \leq 16$). Gupta and collaborators have modified this empirical method and obtained a possible description of the shell corrections for the light as well as heavy mass region [2,3]. The Coulomb (V_C), Proximity (V_P) and angular momentum (V_ℓ) dependent parts of the fragmentation potential (Eq. (2.14)) are discussed in the following sub-sections.

2.4.1 The Repulsive Coulomb potential

Coulomb potential describes the force of repulsion between two interacting nuclei due to their charges and acts along the line joining them. The Coulomb potential for two interacting spherical nuclei is given as

$$V_c = \frac{Z_1 Z_2 e^2}{R} \tag{2.19}$$

For interacting deformed and oriented nuclei, different authors [32–35] have given different expressions. In DCM, the Coulomb potential for two interacting hot, deformed and oriented nuclei is taken from [32] and reads as:

$$V_c(Z_i, \beta_{\lambda i}, \theta_i, T) = \frac{Z_1 Z_2 e^2}{R(T)} + 3Z_1 Z_2 e^2 \sum_{\lambda, i=1,2} \frac{R_i^{\lambda}(\alpha_i, T)}{(2\lambda+1)R(T)^{\lambda+1}} Y_{\lambda}^{(0)}(\theta_i) \left[\beta_{\lambda i} + \frac{4}{7}\beta_{\lambda i}^2 Y_{\lambda}^{(0)}(\theta_i)\right], \quad (2.20)$$

with $Y_{\lambda}^{(0)}(\theta_i)$ as the spherical harmonics function and R_i is taken from Eq. (2.15).

2.4.2 The Attractive Nuclear Proximity Potential

When two nuclear surfaces approach each other within a small distance, comparable to the surface thickness of interacting nuclei ($\approx 2fm$), or when a nucleus is at the verge of dividing into two fragments, then the two surfaces face each other across a small crevice. In both cases, the surface energy term alone could not give rise to the strong attraction that is observed when the two surfaces are brought in close proximity. Such additional attractive forces are called proximity forces and the additional potential due to these forces is called the proximity potential.

Blocki *et al.* [36] have reanalyzed and extended a theorem, originally due to Deryagin [37], according to which the force between two gently curved surfaces in close proximity is proportional to the interaction potential per unit area between the two flat surfaces. Based on the pocket formula of Blocki, the expression for spherical nuclei is given by

$$V_P(s_0) = f(sh., geo.)\Phi(s_0) = 4\pi \bar{R}\gamma b \Phi(s_0). \quad (2.21)$$

Where $\overline{R}$ is the mean curvature radius of the reaction partners, characterizing the gap and is given by

$$\overline{R} = \frac{R_1 R_2}{R_1 + R_2} \quad (2.22)$$

γ is the specific nuclear surface tension given by

$$\gamma = 0.9517\left[1 - 1.7826\left(\frac{N-Z}{A}\right)^2\right] MeVfm^{-2} \tag{2.23}$$

The diffuseness of the nuclear surface b, is given by

$$b = \left[\pi/2\sqrt{3}\ln 9\right]_{t_{10-90}} \tag{2.24}$$

where t_{10-90} is the thickness of the surface in which the density profile changes from 90% to 10%. The value of b$\sim$1 fm and the minimum separation distance s_0 is defined in units of b as s_0/b.

The universal function $\Phi(s_0)$, is independent of the shapes of nuclei or the geometry of nuclear system, but depends on the minimum separation distance s_0 and is defined for negative (the overlap region), zero (touching configuration) and positive values of s_0 as,

$$\Phi(s_0) = \begin{cases} -\frac{1}{2}(s_0 - 2.54)^2 - 0.0852(s_0 - 2.54)^3 \\ -3.437exp(-\frac{s_0}{0.75}) \end{cases} \tag{2.25}$$

respectively, for $s_0 \leq 1.2511$ and $s_0 \geq 1.2511$.

Further, the proximity potential [32] for hot deformed nuclei is given as

$$V_p(A_i, \beta_{\lambda i}, \theta_i, T) = 4\pi\bar{R}(T)\gamma b(T)\Phi(s_0(T)) \tag{2.26}$$

Here, the temperature dependence of b is given by

$$b(T) = 0.99(1 + 0.009T^2) \tag{2.27}$$

For the axially symmetric shapes, the nuclear radius parameter (to all higher multipole orders λ=2,3,4,....) is given by Eqs. (2.15) and (2.16). In terms of the radii of curvature R_{i1} and R_{i2} in the principal planes of curvature of each of the two nuclei (i=1,2) at the points of closest approach, the mean curvature radius $\bar{R}$ for deformed, oriented nuclei is given by

$$\begin{aligned} \frac{1}{\bar{R}^2} &= \frac{1}{R_{11}R_{12}} + \frac{1}{R_{21}R_{22}} + \left[\frac{1}{R_{11}R_{21}} + \frac{1}{R_{12}R_{22}}\right] sin^2\phi \\ &+ \left[\frac{1}{R_{11}R_{22}} + \frac{1}{R_{21}R_{12}}\right] cos^2\phi \end{aligned} \tag{2.28}$$

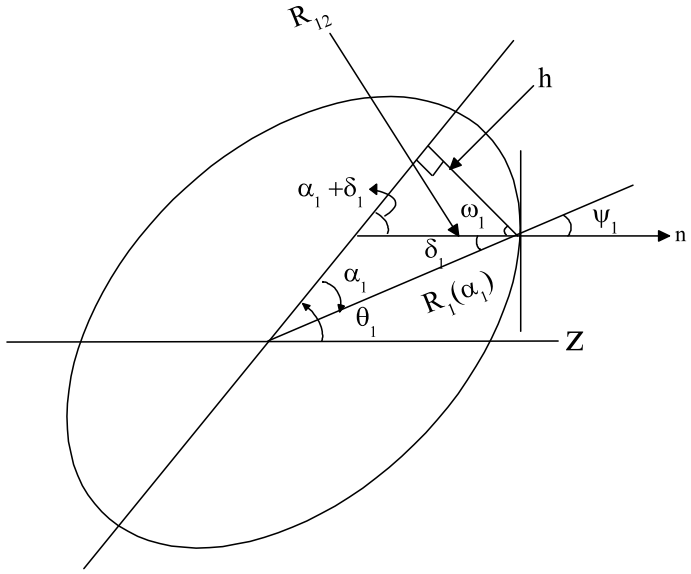

Figure 2.4 The nuclear radius parameter $R_1(\alpha_1)$ and the geometry associated with the principal radius of curvature $R_{12}(\alpha_1)$ for an axially symmetric (quadrupole) deformed and oriented nucleus.

Here, ϕ is the azimuthal angle between the principal planes of curvature of two nuclei (for co-planar nuclei ϕ=0^0). The four principal radii of curvature are

$$\begin{aligned} R_{i1}(\alpha_i) &= \frac{\left[R_i^2(\alpha_i) + R_i'^2(\alpha_i)\right]^{3/2}}{R_i^2(\alpha_i) + 2R_i'^2(\alpha_i) - R_i(\alpha_i)R_i''(\alpha_i)} \\ R_{i2}(\alpha_i) &= \frac{R_i(\alpha_i) sin\alpha_i}{cos(\pi/2 - \alpha_i - \delta_i)} \end{aligned} \tag{2.29}$$

where, $R_i'(\alpha_i)$ and $R_i''(\alpha_i)$ are the first and second order derivatives of $R_i(\alpha_i)$ with respect to α_i, respectively. For the derivation of the radius of curvature R_{i1}, see [38] and it follows from Fig. 2.4, and Ref. [39], that $R_{i2} = h/cos\omega_i$, with $h = R_i(\alpha_i)sin\alpha_i$ and $\omega_i = \pi/2 - \alpha_i - \delta_i$. Also, for **n** to be a normal vector

$$tan\delta_i = -\frac{R_i'(\alpha_i)}{R_i(\alpha_i)}. \tag{2.30}$$

Note that $R_{i1}(\alpha_i) = R_{i2}(\alpha_i)$, respectively, for $\alpha_1 = 0^0$ or 180^0 and $\alpha_2 = 180^0$ or 360^0. For deformed and oriented nuclei, the minimum distance s_0, (defined in Fig. 2.3) for a fixed R, is given as

$$s_0 = R - R_1 - R_2 \tag{2.31}$$

where R_i is defined in Eq. (2.15). With the projections X_i along the Z-axis given as

$$\begin{aligned} X_1 &= R_1(\alpha_1)cos(\theta_1 - \alpha_1) \\ X_2 &= R_2(\alpha_2)cos(180 + \theta_2 - \alpha_2) \end{aligned} \tag{2.32}$$

the Eq. (2.31) takes the form,

$$s_0 = R - X_1 - X_2 \tag{2.33}$$

and the minimization conditions on s_0,

$$\frac{\partial s_0}{\partial \alpha_1} = \frac{\partial s_0}{\partial \alpha_2} = 0, \tag{2.34}$$

resulting in

$$\begin{aligned} \tan(\theta_1 - \alpha_1) &= -\frac{R_1'(\alpha_1)}{R_1(\alpha_1)} \\ \tan(180 + \theta_2 - \alpha_2) &= -\frac{R_2'(\alpha_2)}{R_2(\alpha_2)}. \end{aligned} \tag{2.35}$$

Comparing Eqs. (2.30) and (2.35), we get

$$\begin{aligned} \delta_1 &= \theta_1 - \alpha_1 \\ \delta_2 &= 180 + \theta_2 - \alpha_2, \end{aligned} \tag{2.36}$$

to be used in Eq. (2.29). Thus, for the given θ_1 and θ_2, X_1 and X_2 are obtained for the angles α_1 and α_2 satisfying the minimization conditions shown in Eq. (2.34). It may be noted that the Eq. (2.35) refers to perpendiculars (normal vectors) at the points P_1 and P_2 in Fig. 2.3. In other words, if the distance s_0 were to be shortest, the perpendicular conditions in Eq. (2.35) must be used which would apparently give Eq. (2.32) for X_i.

The proximity potential (V_P) for deformed and oriented nuclei given by Eq. (2.26) is valid for zero (touching configuration) and positive values of s_0, but is also used for

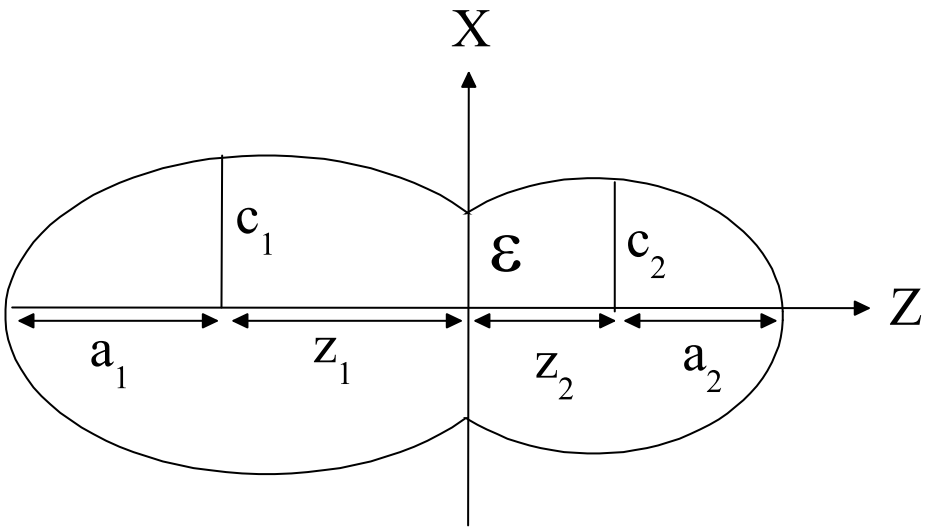

Figure 2.5 Sample nuclear shape formed in two center shell model [24].

negative s_0. As the two nuclei overlap ($s_0 < 0$) a crevice is formed and in an adiabatic approximation, the system adjusts its shape parameters such that the two colliding nuclei form a single indented body. For such a necked system, shown in Fig. 2.5, following Blocki *et al.* [36], the proximity potential is obtained by Gupta and collaborators [40, 41] as

$$V_P(s_0) = \pi\gamma b^2 \Phi_1(s_0 = 0) \frac{(c_1^2 + c_2^2 - 2\epsilon^2)}{(z_1^2 + z_2^2)} \tag{2.37}$$

where $\Phi_1(s_0 = 0)$=-2.0306 is the first moment of the universal function Φ at $s_0 = 0$, and c_i, z_i and ϵ are the shape parameters depicted in Fig. 2.5.

2.4.3 The Centrifugal Potential

The angular momentum ℓ, plays a crucial role as it governs the centrifugal potential and hence the rotational energy associated with nuclear dynamics. The entrance channel orbital angular momentum is transferred into internal degrees of freedom of the fragments. The transfer of angular momentum is induced by frictional forces acting between nuclei sliding on each other. The two nuclei sliding each other in initial stage result into non-sticking configuration. The viscous force caused due to sliding exerts a torque on each

fragment leading the system to rolling stage after which the fragments rotate rigidly in a sticking configuration [42] .

The additional energy due to the rotational motion of nucleons is defined as

$$V_\ell(R, A_i, \beta_{\lambda i}, \theta_i, T) = \frac{\hbar^2 \ell(\ell+1)}{2I(T)} \tag{2.38}$$

here I is the moment of inertia defined for sticking (I_S) and non-sticking (I_{NS}) configuration. Mostly, the decay cross sections have been estimated using sticking limit (I_s) of moment of inertia in which the rotation of two touching spheres is considered about their common center of mass. The moment of inertia for complete sticking limit I_S is given as,

$$I_s(T) = \mu R^2 + \frac{2}{5} A_1 m R_1^2(\alpha_1, T) + \frac{2}{5} A_2 m R_2^2(\alpha_2, T). \tag{2.39}$$

where $\mu(= \frac{A_1 A_2}{A_1+A_2} m)$ and m are reduced mass and nucleon mass respectively and R_i is the radius as defined in Eq. (2.15). The choice of moment of inertia in sticking limit is attributed to the use of proximity potential of Blocki et.al., [36] in DCM based calculations.

On the other hand, for the non-sticking limit of moment of inertia, given as $I_{NS}(T)$=μR^2, no intrinsic rotation of fragments is considered due to the small separation distance between them and the fragment emission process is treated as punctual. It is relevant to mention here that the experimentally extracted value of angular momentum is based on the moment of inertia in non-sticking limit [3]. In the present work, a comparative study on I_S and I_{NS} limit of moment of inertia has been made for the decay of intermediate mass ^{96}Tc* nucleus. It has been observed that I_S choice of moment of inertia with large limiting value of angular momentum, is more favorable in view of the use of proximity interaction (nuclear surface $\approx$ 2fm). On the other hand, non sticking limit seem appropriate to estimate the cross-section for superheavy nuclei and for fission fragment anisotropies [8, 9]. The dependence of anisotropy on different quantities is explored through DCM within SSPM approach [43]. The fission fragment anisotropy A is related

to the total ℓ value (equivalently ℓ_{max}) of the CN, the effective moment-of-inertia I_{eff} of the fissioning nucleus in the transition state (at the saddle point), and the temperature T at the saddle point, as

$$A = 1 + \langle \ell^2 \rangle / 4K_0^2, \tag{2.40}$$

with

$$K_0^2 = T \times I_{eff}/\hbar^2, \tag{2.41}$$

Here I_{eff} is calculated by using the finite-range rotating liquid drop model [44] with T being the temperature of the fissioning nucleus. The value of ℓ_{max} depends on the use of I_S or I_{NS} in the ℓ-dependent potential V_ℓ (Eq. 2.38).

It is worth mentioning that, for a fixed η i.e for a given target projectile (A_1, A_2) combination, the scattering potential $V(R)$, defined as the sum of Coulomb, proximity and angular momentum-dependent potentials, where temperature, deformation and orientation effects are duly included is given by;

$$\begin{aligned} V(R, \ell, T) &= V_c(R, Z_i, \beta_{\lambda i}, \theta_i, \phi, T) + V_p(R, A_i, \beta_{\lambda i}, \theta_i, \phi, T) \\ &+ V_\ell(R, A_i, \beta_{\lambda i}, \theta_i, \phi, T) \end{aligned} \tag{2.42}$$

Fig. 2.2 shows the scattering potential for the decay of $^{201}Bi^*$ nucleus in form of evaporation residue at two different energies for negative and positive Q_{out} values shown in parts (a) and (b) respectively. The inner radius R_a and the separation parameter R, are also marked in the figure.

After an overview of the input quantities used in Schrödinger equation, it would be of further interest to address the preformation probability obtained as solution of Schrödinger equation and the barrier penetration probability based on WKB approach. A brief account of preformation probability (P_0) and barrier penetrability (P) is discussed respectively in Sec.2.5 and 2.6.

2.5 Preformation Probability (solution of the stationary Schrödinger equation)

Once the Hamiltonian of Eq. (2.10) is established, the Schrödinger equation in mass fragmentation co-ordinate η (Eq. (2.11) can be solved numerically, ($|\psi^{\nu}(\eta)|^2$), which gives the formation probability (P_0) of decaying fragments as

$$P_0(A_2) \propto |\psi^{\nu}(A_2)|^2 \tag{2.43}$$

with ν=0,1,2,3... referring to ground state (ν=0) and excited state solution, at a fixed R=R$_a$, the inner radius of the penetration path defined in Sec.2.7 and shown in Fig. 2.2. For the nuclear ground state processes such as spontaneous fission or cluster decay, and to have complete adiabaticity, only the lowest vibrational state $\nu = 0$ is occupied. Then, the mass (or charge) distribution yield, proportional to the probability $|\psi^{(0)}(\eta)|^2$ (or $|\psi^{(0)}(\eta_Z)|^2$) of finding a certain mass (or charge) fragmentation η (or η_Z) at a position R on the decay path, when scaled to, say, mass A_2 of one of the fragments ($d\eta = \frac{2}{A}$) is given by:

$$P_0 = |\psi_R^{(0)}(A_2)|^2 \frac{2}{A} \sqrt{B_{\eta\eta}(A_2))} \tag{2.44}$$

However, if the system is excited or we allow interaction between various degrees of freedom, higher values of ν would also contribute. These enter via the excitation of higher vibrational states, and through the temperature dependent potential V and masses B_{ij}.

The effect of adding temperature on potential V and masses B_{ij} is to reduce the shell effects in them, resulting finally in the liquid drop potential V_{LDM} and smoothed (averaged) masses $\bar{B}_{ij}$ for the systems to be very hot. The possible consequences of such excitations are included here by assuming a Boltzmann like occupation of excited states

$$|\psi(\eta)|^2 = \sum_{\nu=0}^{\infty} |\psi^{\nu}(\eta)|^2 \exp\left(-\frac{E_{\eta}^{\nu}}{T}\right) \tag{2.45}$$

Note that we are dealing here with a directly measurable quantity, the mass (or charge) asymmetry, which works dynamically as mass (or charge) transfer coordinate. Thus, the calculated yields $P_0(A_i)$ (or $P_0(Z_i)$) are directly comparable with experiments. The nuclear shape, once minimized in the neck ε and deformation coordinates β_1 and β_2 at a given R ($\approx R_{saddle}$), remains fixed for both the mass and charge distributions of fission or decay fragments. After having an idea about formation probability of decaying fragments at CN state, further interest is to analyze the barrier penetration probability of such fragments formed in the collective clusterization process. This barrier penetration probability P is explained in the next section.

2.6 Penetration Probability

Once the fragments or clusters are preformed, their penetration probability P across the interaction barrier can be calculated by using the WKB approximation. For R-motion, instead of solving the Schrödinger Eq. (2.12), we use the WKB approximation to calculate the penetration probability P. For each η-value, the potential $V(R)$ for $R \geq R_t$ is calculated by using Eq. (2.42) and for $R < R_t$ it is parameterized simply as a polynomial of degree two in R, so that

$$V(R) = \begin{cases} a_1 R + a_2 R^2 & for \quad R_0 \leq R \leq R_t \\ V_c + V_p + V_\ell & for \quad R \geq R_t \end{cases} \tag{2.46}$$

The constants a_i ($i = 1, 2$) occurring in the polynomial, are determined by using the following boundary conditions.

1. At $R = R_0$, $V(R) = Q$

2. At $R = R_t$, $V(R) = V(R_t)$

The inner radius (entry point) R_a is chosen at $R_a = R_t + \Delta R$, where $R_t = R_1 + R_2$ and the outer radius (exit point) taken at R_b, corresponds to Q-value of the reaction, i.e., $V(R_b) = Q$. For a heavy cluster decaying into the excited states of the daughter nucleus [45], P is given as,

$$P = P_i P_b, \tag{2.47}$$

where P_i and P_b are calculated by using WKB approximation, as

$$P_i = \exp\left[-\frac{2}{\hbar}\int_{R_a}^{R_i}\{2\mu[V(R) - V(R_i)]\}^{1/2}dR\right] \tag{2.48}$$

and

$$P_b = \exp\left[-\frac{2}{\hbar}\int_{R_i}^{R_b}\{2\mu[V(R) - Q]\}^{1/2}dR\right] \tag{2.49}$$

This means that the tunneling begins at $R = R_a$ and terminates at $R = R_b$, with $V(R_b) =$ Q-value for ground state decay. The integrals of the Eqs. (2.48) and (2.49) are solved analytically by parameterizing the above calculated potential $V(R)$, as prescribed in [41, 46]. This procedure is followed for the ground state decay however for the decay from an excited (hot) compound nucleus with total excitation energy TXE of decaying fragments, we consider $V(R_a) = V(R_b) = Q_{eff} = TKE + Q_{out}$

For P=P_b given by Eq. (2.49), where Q is replaced by Q_{eff} and the limits of integration are from R_a to R_b, P takes the form,

$$P = exp[-\frac{2}{\hbar}\int_{R_a}^{R_b}\{2\mu[V(R) - Q_{eff}]\}^{1/2}dR] \tag{2.50}$$

The barrier characteristics exhibiting entry and exit points of barrier tunneling process and consequent emergence of barrier modification is addressed next Sec.2.7.

2.7 Barrier Characteristics

For the decay of a hot CN, we choose the inner radius (entry point) as

$$R_a(T) = R_t + \Delta R(\eta, T) \tag{2.51}$$

where

$$R_t = R_1(\alpha_1, T) + R_2(\alpha_1, T) \tag{2.52}$$

$\Delta R(T)$ is the neck-length parameter that assimilates the neck formation effects. This method of introducing a neck length parameter is similar to that used in scission-point [47] and saddle-point [48, 49] statistical fission models. The R_i are radius vectors which are also made temperature dependent, given by Eqs.(2.15 and 2.16).

The corresponding potential $V(R_a)$ acts like an effective Q-value, Q_{eff}, for the decay of the hot CN at temperature T, to two exit-channel fragments observed in ground state (T=0), defined by

$$\begin{aligned} Q_{eff}(T) &= B(T) - [B_L(T=0) + B_H(T=0)] \\ &= TKE(T) = V(R_a(T)) \end{aligned} \tag{2.53}$$

with B's as the respective binding energies.

The above defined decay of a hot CN into two cold (T=0) fragments, via Eq. (2.53), could apparently be achieved only by emitting some light particle (s) (LPs), like n, p, α, or γ-rays of energy

$$\begin{aligned} E_x &= B(T) - B(0) = Q_{eff}(T) - Q_{out}(T=0) \\ &= TKE(T) - TKE(T=0) \end{aligned} \tag{2.54}$$

which is zero for the g.s. decay, like for cluster radioactivity [50]. Note that the second equality in Eq. (2.54) is not defined for a negative $Q_{out}(T=0)$ system since the negative TKE(T=0) has no meaning. Apparently, Eq. (2.54) w.r.t (2.53) suggest that the emission of light-particles starts early in the decay process. The excitation energy TXE(T) (not treated here), is used in the secondary emission of light particles from

the fragments which are otherwise in their ground states with TKE(T=0) in the radial motion. Thus, by defining $Q_{eff}(T)$ as in Eq. (2.53), we treat the LP emission at par with the heavy fragments, such as intermediate mass fragments (IMFs), heavy mass fragments (HMFs) and fission fragments. It is relevant to mention here that, in this model a non-statistical dynamical treatment is attempted for not only the emission of HMFs but also of multiple LPs, understood as the statistically evaporated particles in a CN emission. It may be reminded here that the statistical model interpretation of LPs, IMFs, HMFs and fission fragments is worked out independently [47–49]- [51–53] , whereas DCM description is based on collective clusterization process treating LPs and heavy fragments on equal footing.

In terms of $Q_{eff}(T)$, the outer radius R_b satisfies

$$V(R_a, \ell) = V(R_b, \ell) = Q_{eff}(T, \ell) = TKE(T) \tag{2.55}$$

with the ℓ-dependence of R_a defined by

$$V(R_a) = Q_{eff}(T, \ell = 0), \tag{2.56}$$

i.e the decay path, defined in Eq. (2.55) for each ℓ, begin at R_a, fixed for the ℓ=0 case and it means that R_a is same for all ℓ-values, given by the above Eq. (2.56), and that $V(R_a, \ell)$ acts like an effective Q-value, $Q_{eff}(T, \ell)$, given by the total kinetic energy $TKE(T)$. Then, using Eq. (2.55), $R_b(\ell)$ is given by the ℓ-dependent scattering potentials, at fixed T for coplanar nuclei, as in Eq. (2.42), which is normalized to the exit channel binding energy $B_L(T) + B_H(T)$. After having a comprehensive analysis of entry and exit point of barrier tunnelling process, it is of further interest to account for the barrier modification aspect which originates from the inclusion of neck elongation Δ R.

As we know that the overestimation of cross-sections within coupled channel calculations at sub barrier energies is termed as the fusion hindrance. This phenomena of hinderance may be attributed to several reasons such as low binding energy of the pro-

jectile, shell structure of projectile and target, halo nuclei involved in a reaction, or due to presence of some competing direct or non-compound nucleus process. The explanation of one or more of these causes requires the adequate modification of the barrier profile i.e. barrier modification, which is supported well within DCM in terms of its index of barrier lowering, ΔV_B. This property of 'lowering of barriers' (without modifying the depth of potential pocket) at sub-barrier energies arises in DCM in a simple way via its neck-length parameter, ΔR. The choice of inner radius R_a, (equivalently, ΔR) for the best fit to the data corresponds to the effects of "barrier lowering" defined for each decay channel for each ℓ, as the difference between $V_B(\ell)$ and $V(R_a, \ell)$ i.e., the barrier height and the actually used barrier, as

$$\Delta V_B(\ell) = V(R_a, \ell) - V_B(\ell). \tag{2.57}$$

It may be noted that, ΔV_B for each ℓ is defined as a negative quantity as the actual barrier height is effectively lowered (illustrated in Fig. 2.2). It is worth noting in Fig. 2.2 that, ΔV_B is higher for lower angular momentum value. Though not plotted here, but ΔV_B decreases with increase in energy, being large at lower energies. This aspect is discussed in the subsequent chapters.

2.8 DCM for incomplete fusion and non-compound nucleus processes

So far it has been discussed that in DCM the deformation and orientation degrees of freedom have been explicitly included along with temperature and angular momentum effects and is capable of producing the cross-sections for various CN decay processes over a wide range of nuclei varying from heavy to light mass region. However, in recent years,

DCM has also been applied to study the reactions invovling incomplete fusion (ICF) and non-compound nucleus processes such as quasi-fission (QF), deep inelastic collision (DIC) etc. The pursual with these processes demands incorporation of characteristic features of incomplete fusion (ICF) and non-compound nuclear dynamics in the framework of DCM.

As discussed in chapter 1, the incomplete fusion process is observed for nuclei having relatively low binding energy, responsible for break-up of projectile. To obtain the energy associated with projectile obtained after break-up, appropriate energy correction to the fragile projectile is applied, by considering the incident lab energy, E_{Lab} to be shared equally among all nucleons of projectile. Consequently, the energy of each nucleon of the incident projectile can be estimated, through which the energy of the new projectile obtained after breakup may be obtained. If A^P represents the mass number of projectile before break-up, then the energy of the projectile would be

$$E_{Projectile} = \frac{E}{A} * A^P \tag{2.58}$$

Further considering the velocity of ejectile same as original projectile, the energy of ejectile particle having mass A^E can be obtained as

$$E_{Ejectile} = \frac{E}{A} * A^E \tag{2.59}$$

Hence the energy of new projectile obtained after break-up process with mass number A^P_{ICF} becomes

$$E^P_{ICF} = \frac{E}{A} * A^P - \frac{E}{A} * A^E \tag{2.60}$$

The application of DCM using energy correction for ICF process has been discussed in chapter 4 and 5. Also, the angular momentum ℓ plays a crucial role in the decay mechanism involved. It has been observed that ℓ_{crit} defined in terms of the bombarding energy $E_{c.m.}$, reduced mass μ, the inner radius (entry point) R_a of the entrance channel η_{in} as,

$$\ell_c = R_a\sqrt{2\mu[E_{c.m.} - V(R_a, \eta_{in}, \ell = 0)]}/\hbar, \tag{2.61}$$

is important for disentangling the ICF and CF processes. This is because above ℓ_{crit}, the centrifugal potential suppresses the attractive nuclear potential, due to which the complete fusion of the projectile is hindered, giving rise to the break-up of the projectile and hence the incomplete fusion. Thus for ^{96}Tc* nucleus the CF process is studied for $\ell \leq \ell_{crit}$ and ICF is considered for $\ell > \ell_{crit}$ upto ℓ_{max}, which is defined at a point where the light-particle cross-section $\sigma_{LP}(\ell) \rightarrow 0$ or the preformation probability becomes negligibly small.

Apart from ICF, a non-compound nucleus process known as deep inelastic collision (DIC) is also observed for ℓ values above ℓ_{crit}. Moreover, DIC process also retains the memory of entrance channel as explained in chapter 1. Thus in DCM the preformation probability P_0 is considered unity and distributed equally among the projectile like and target like decaying fragments observed through DIC process which for the CN case is different for different decay fragments. Chapter 6 represents the DIC results investigated for the light mass $^{40}Ca^*$ and $^{39}K^*$ system.

Apart from these processes, another nCN mechanism studied using DCM is Quasi-fission (QF) which unlike ICF and DIC processes is studied for all the ℓ-values varying from ℓ=0$\hbar$ to ℓ_{max}. Also, the orientation degree of freedom is observed to influence the QF contribution. In framework of DCM, the role of orientation on the QF process is studied in chapter 3. The application of DCM to various nuclei exhibiting different decay processes is discussed in the chapters ahead.

Bibliography

[1] R. K. Gupta, R. Kumar, N. K. Dhiman, M. Balasubraniam, W. Scheid, and C. Beck, Phys. Rev. C **68**, 014610 (2003).

[2] M. Balasubramaniam, R. Kumar, R. K. Gupta, C. Beck, and W. Scheid, J. Phys. G **29**, 2703 (2003).

[3] B. B. Singh, M. K. Sharma, and R. K. Gupta, Phys. Rev. C **77**, 054613 (2008).

[4] R. K. Gupta, M. Balasubramaniam, R. Kumar, D. Singh, and C. Beck, Nucl. Phys. A **738**, 479c (2004); R. K. Gupta, M. Balasubramaniam, R. Kumar, D. Singh, C. Beck, and W. Greiner, Phys. Rev. C **71**, 014601 (2005).

[5] B. B. Singh, M. K. Sharma, R. K. Gupta, and W. Greiner, Int. J. Mod. Phys. E **15**, 699 (2006).

[6] S. Kanwar, M. K. Sharma, B. B. Singh, R. K. Gupta, and W. Greiner, Int. J. Mod. Phys. E **18**, 1453 (2009); S. K. Arun, R. Kumar, and R. K. Gupta, J. Phys. G: Nucl. Part. Phys. **36**, 085105 (2009).

[7] M. K. Sharma, S. Kanwar, G. Sawhney, R. K. Gupta, and W. Greiner, J. Phys. G: Nucl. Part. Phys. **38**, 055104 (2011); D. Jain, R. Kumar, M. K. Sharma, and R. K. Gupta, Phys. Rev. C **85**, 024615 (2012).

[8] M. K. Sharma, G. Sawhney, R. K. Gupta, and W. Greiner, J. Phys. G: Nucl. Part. Phys. **38**, 105101 (2011); M. K. Sharma, G. Sawhney, S. Kanwar, and R. K. Gupta, Mod. Phys. Lett. A **25**, 2022 (2010).

[9] G. Sawhney and M. K. Sharma, Eur. Phys. J. A **48**, 57 (2012); M. K. Sharma, S. Kanwar, G. Sawhney, and R. K. Gupta, Phys. Rev. C **85**, 064602 (2012); G. Sawhney, R. Kumar, and M. K. Sharma, Phys. Rev. C **86** (2012) 034613.

[10] M. Kaur, R. Kumar, and M. K. Sharma, Phys. Rev. C **85**, 014609 (2012).

[11] M. Kaur and M. K. Sharma, Phys. Rev. C **85**, 054605 (2012); M. Kaur, M. K. Sharma and Raj K. Gupta, Phys. Rev. C **86**, 064610 (2012).

[12] M. Kaur and Manoj K. Sharma, *International Conference On Recent Trends in Nuclear Physics-2012*, published in AIP conf. proc. **1524**, pp.151-154 (2013).

[13] K. Sandhu, M. K. Sharma, and R. K. Gupta, Phys. Rev. C **85**, 024604 (2012); G. Kaur and M. K. Sharma, Nucl. Phys. A **884**, 36 (2012); G. Kaur and M. K. Sharma, Phys. Rev. C **87**, 044601 (2013).

[14] J. Maruhn and W. Greiner, Phys. Rev. Lett. **32**, 548 (1974).

[15] R. K. Gupta, W. Scheid, and W. Greiner, Phys. Rev. Lett. **35**, 353 (1975).

[16] A. Săndulescu, R. K. Gupta, W. Scheid, and W. Greiner, Phys. Lett. B **60**, 225 (1976); R. K. Gupta, A. Săndulescu, and W. Greiner, Phys. Lett. B **67**, 257 (1977); Rev. Roum. Phys. **23**, 51 (1978).

[17] S. Yamaji, W. Scheid, H. J. Fink, and W. Greiner, Z. Phys. A **278**, 69 (1976); S. Yamaji, W. Scheid, H. J. Fink, and W. Greiner, J. Phys. G: Nucl. Phys. **2**, L189

(1976); S. Yamaji, K. H. Ziegenhain, H. J. Fink, W. Greiner, and W. Scheid, J. Phys. G: Nucl. Phys. **3**, 1283 (1977).

[18] R. K. Gupta, A. Săndulescu, and W. Greiner, Z. Naturforsch, **32a**, 704 (1977); R. K. Gupta, C. Pirvulescu, A. Săndulescu, and W. Greiner, Z. Phys. A **283**, 217 (1977); Sovt. J. Nucl. Phys. **28**, 160 (1978); R. K. Gupta, Z. Phys. A **281**, 159 (1977).

[19] A. Săndulescu, H. J. Lustig, J. Hahn, and W. Greiner, J. Phys. G: Nucl. Phys. **4**, L279 (1978); H. J. Lustig, J. A. Maruhn, and W. Greiner, J. Phys. G: Nucl. Phys. **6**, L25 (1980).

[20] H. J. Fink, W. Greiner, R. K. Gupta, S. Liran, J.H. Maruhn, W. Scheid, and O. Zohni, in Proceedings of Int. Conf. on Reaction between Complex Nuclei, Nashville, (Amsterdam: North Holland), **21**, pages 2 (1974).

[21] R. K. Gupta, IANCAS Bull. (India), **6**, 2 (1990).

[22] V. M. Strutinsky, Nucl. Phys. A **95**, 420 (1967).

[23] H. Kröger and W. Scheid, J. Phys. G **6**, L85 (1980).

[24] R. K. Gupta, N. Singh, and M. Manhas, Phys. Rev. C **70**, 034608 (2004).

[25] G. Audi, A. H. Wapstra and C. Thiboult, Nucl. Phys. A **729**, 337 (2003).

[26] P. Möller, J. R. Nix, W. D. Myers, and W. J. Swiatecki, At. Data Nucl. Data Tables **59**, 185 (1995).

[27] N. J. Davidson, S. S. Hsiao, J. Markram, H. G. Miller, and Y. Tzeng, Nucl. Phys. A **570**, 61c (1994).

[28] P. A. Seeger, Nucl. Phys. **25**, 1 (1961).

[29] S. DeBenedetti, Nuclear Interactions (New York: Wiley) (1964).

[30] G. Audi and A. H. Wapstra, Nucl. Phys. A **595**, 4 (1995).

[31] W. Myers and W. J. Swiatecki, Nucl. Phys. **81**, 1 (1966).

[32] R. K. Gupta, M. Balasubramaniam, R. Kumar, N. Singh, M. Manhas and W. Greiner, J. Phys. G: Nucl. Part. Phys. C **31**, 631 (2005).

[33] M. Münchow, D. Hahn and W. Scheid, Nucl. Phys. A **388**, 381 (1982).

[34] M. J. Rhoades-Brown, V. E. Oberacker, M. Seiwert and W. Greiner, Z. Phys. A **310**, 287 (1983).

[35] C. Y. Wong, Phys. Rev. Lett. **31**, 766 (1973).

[36] J. Blocki, J. Randrup, W. J. Swiatecki, and C. F. Tsang, Ann. Phys. (NY) **105**, 427 (1977).

[37] Deryagin, Kolloid Z. **69**, 155 (1934).

[38] A. Gray, *Modern Differential Geometry of Curves and Surfaces with Mathematica*, 2nd Edition, CRC Press, Boca Raton, 1997, p.89.

[39] M. Seiwert, W. Greiner, V. Oberacker, and M.J. Rhoades-Brown, Phys. Rev. C **29**, 477 (1984).

[40] N. Malhotra and R. K. Gupta, Phys. Rev. C **31**, 1179 (1985).

[41] S. Kumar and R. K. Gupta, Phys. Rev. C **55**, 218 (1997).

[42] P. Glassel, R. S. Simon, R. M. Diamond, R. C. Jared, I. Y. Lee, L. G. Moretto, J. O. Newton, R. Schmitt and F. S. Stephens, Phys. Rev. Lett. **38**,7 (1977)

[43] R. Vandenbosch and J. R. Huizenga, *Nuclear Fission* (Academic: New York) (1973).

[44] A. J. Sierk, Phys. Rev. C **33**, 2039 (1986).

[45] M. Greiner and W. Scheid, J. Phys. G: Nucl. Phys. **12** L229 (1986).

[46] S. S. Malik and R. K. Gupta, Phys. Rev. C **39**, 1992 (1989).

[47] T. Matsuse, C. Beck, R. Nouicer, and D. Mahboub, Phys. Rev. C **55**, 1380 (1997).

[48] S. J. Sanders, D. G. Kovar, B. B. Back, C. Beck, D. J. Henderson, R. V. F. Janssens, T. F. Wang, and B. D. Wilkins, Phys. Rev. C **40**, 2091 (1989).

[49] S. J. Sanders, Phys. Rev. C **44**, 2676 (1991).

[50] R. K. Gupta and W. Greiner, Int. J. Mod. Phys. E, Suppl. **3**, 335 (1994).

[51] J. Gomez del Campo, R.L. Auble, J.R. Beene, M.L. Halbert, H.J. Kim, A. D'Onofrio, and J.L. Charvet, Phys. Rev. C **43**, 2689 (1991); Phys. Rev. Lett. **61**, 290 (1988).

[52] R. J. Charity, M. A. McMahan, G. J. Wozniak, R. J. McDonald, L. G. Moretto, D. G. Sarantites, L. G. Sobotka, G. Guarino, A. Pantaleo, L. Fiore, A. Gobbi and K. D. Hildenbrand, Nucl. Phys. A **483**, 371 (1988).

[53] C. Beck, R. Nouicer, D. Disdier, G. Duchêne, G. de France, R.M. Freeman, F. Haas, A. Hachem, D. Mahboub, V. Rauch, M. Rousseau, S.J. Sanders, and A. Szanto de Toledo, Phys. Rev. C **63**, 014607 (2001).

Chapter 3

Dynamics of heavy mass nuclei using collective clusterization approach

3.1 Introduction

In heavy-ion fusion reactions, the compound nucleus (CN) is formed at a particular excitation energy (E^*_{CN}) with a broad range of angular momentum varying from ℓ=0$\hbar$ to ℓ_{max}. It is generally believed that decay of CN is independent of its mode of formation, except for the requirement of various conservation laws, and it can decay in a number of ways depending on the incident energy of projectile, the deformations and the shape orientations of both projectile and target nuclei. In general, the decay of CN goes through processes like evaporation residue (ER), intermediate mass fragments (IMF) and fusion-fission (ff), described by various theoretical models, like the statistical evaporation [1–5] and fission model [6, 7], the thermodynamical Dubna model of heated CN [8–10], and the dynamical cluster-decay model [11–23], used here. Interestingly, either different combinations of the above mentioned decay processes or any one of them is found to occur in different mass regions of compound nuclei. In this chapter the decay of Fr isotopes and Z=112 isotopes

is investigated respectively in heavy and superheavy mass region to address ER and ff decay channels. The results of this study are published in [24, 25].

For heavy mass region, the odd-mass ^{213,215,217}Fr* isotopes [20–22] have been recently studied over a wide center-of-mass (c.m.) energy range of 48 to 94 MeV, using the DCM with deformation and orientation effects included in it. For the measured decay paths of compound systems ^{213,217}Fr*, formed in ^{19}F+^{194,198}Pt reactions at $E_{c.m.}$= 80-94 MeV [26], the fission anisotropy data for ^{217}Fr* (with neutron number N=130) shows nice comparison with the statistical saddle-point model (SSPM), but the same is not true for ^{213}Fr* (with N=126), showing significant deviations between measured and SSPM calculated anisotropies. This anomaly in fission anisotropy for ^{213}Fr* is believed by the authors [26] to be associated with either the magic N=126 shell of the CN or presence of non-compound nucleus (nCN) component, like the quasi-fission (QF). On the other hand, the DCM calculated [20] ff cross-sections (as well as the ER cross-sections) match the available data [26] nearly exactly, with QF contribution of only ∼4-10% (of ff cross-sections for the lowest to highest energy) for ^{213}Fr* and 8-10% for ^{217}Fr* nucleus. However, the fission anisotropy data [26] itself was not analyzed on the DCM for ^{213,217}Fr* systems, and the same is worked out in this chapter. It is worth noting that DCM is based on collective clusterization picture where the magic shell effects of CN do not come in to play. Instead, a small hump/ shoulder is observed [20] in calculated fragment preformation yields, which arises due to deformed shell closure of light fragment Z_2=36 and spherical shell closure of heavy fragment Z_1=50, which is relatively more pronounced in the decay of N=126 ^{213}Fr* isotope than in N=130 ^{217}Fr* nucleus. Besides this, the ^{215}Fr* system studied within DCM [21, 22] in reference to an older data of [27] is formed via two different reaction channels ^{11}B+^{204}Pb and ^{18}O+^{197}Au, at two different center-of-mass energy ranges of $E_{c.m.}$=47.97 - 60.24 and 71.17 - 88.66 MeV, respectively. In agreement with experimental

data and statistical model (PACE2) calculations, the DCM confirms the entrance channel independence of the decay of ^{215}Fr* isotope [21, 22].

In this chapter, the earlier work of odd-mass ^{213,215,217}Fr* isotopes [20–22] has been extended to a complete study of decay cross-sections (both ER and ff) and fission fragment anisotropies for the reactions ^{18}O+^{197}Au$\rightarrow^{215}$Fr* and ^{19}F+^{194,198}Pt$\rightarrow^{213,217}$Fr* at full range of $E_{c.m.}$ = 48 - 106 MeV, based on the three experiments of Refs. [26–28], using the collective clusterization approach of DCM. The detailed analysis of temperature, angular momentum effects, preformation factor, and barrier modification, etc., is worked out in context to the reactions under investigation. In addition, the role of isospin (N/Z ratio of CN) is further explored for decay of Fr isotopes with mass number varying from A=211-219, i.e., the above study extended to two other odd-mass isotopes ^{211,219}Fr*. The motivation of this study is to look for the possible role of shell effects of decaying fragments in above mentioned Fr isotopes. A comparison of the earlier studied potential energy surfaces for ^{213,217}Fr* with those of ^{211,215,219}Fr* isotopes could reveal the effects of the underlying shell closure in all the decaying Fr isotopes studied here.

In addition to the decay pattern of Fr isotopes, this chapter also presents the impact of hot and cold orientation in the dynamics of superheavy Z=112 isotopes. For advancement in synthesis of superheavy nuclei, the usual cold fusion process involving symmetric reaction partners was replaced by hot fusion process involving highly asymmetric reaction partners. Consequently, the adoption of hot fusion process involving deformed actinide targets rather than spherical targets such as ^{208}Pb and ^{201}Bi, provide an opportunity to study the decay properties of more n-rich transfermium isotopes.

At above Coulomb barrier energies the orientation of prolate deformed target explores the opportunity, that projectile may hit the equatorial part of target and form most compact configuration on way to compound nucleus formation. However, in sub-barrier

region the hot (equatorial) compact collisions may be substituted by the cold collisions, where elongated (polar) configuration may result into re-separation of reaction partners, giving rise to the quasi-fission phenomenon [12, 29]. With this understanding, the DCM has been applied to investigate the effect of orientation degree of freedom across the Coulomb barrier for $^{278,286}112^{*}$ isotopes formed in $^{40,48}Ca+^{238}U$ reaction [30]. In the following, the details of calculations and results obtained for Fr and Z=112 isotopes are presented in Sec.3.2 and a summary of the results is discussed in Sec.3.3.

3.2 Calculations

This section is divided into three sub-sections. In Sec.3.2.1, the calculations are presented for the decay of $^{213,215,217}Fr^{*}$ isotopes formed in $^{19}F+^{194}Pt$, $^{18}O+^{197}Au$ and $^{19}F + ^{198}Pt$ reactions respectively, over a wide range of available incident energies [26–28]. It is important to note that the selected range of energies correspond to above as well as below Coulomb barrier energy (the barrier lies around ∼84 MeV for $^{19}F+^{194,198}Pt$ channels and 87 MeV for $^{18}O+^{197}Au$ channel). Using DCM, the yields of evaporation residues are predicted for the decay of $^{213,215,217}Fr^{*}$ nuclei and fission data are addressed for $^{213,217}Fr^{*}$ systems, at energies not covered in earlier work [20–22]. Also, the channel independence of $^{18}O+^{197}Au$ and $^{19}F+^{196}Pt$ reactions is investigated and fission fragment anisotropies are calculated for the $^{19}F+^{194,198}Pt$ reactions in addition to "barrier modification" effects at sub-barrier energies. Further, in Sec.3.2.2 the shell closure effects of the decay fragments and their N/Z dependence is explored for $^{211-219}Fr^{*}$ isotopes. Finally, the role of hot (equatorial) compact and cold (polar) elongated configuration is analysed for $^{278,286}112^{*}$ nuclei in Sec.3.2.3.

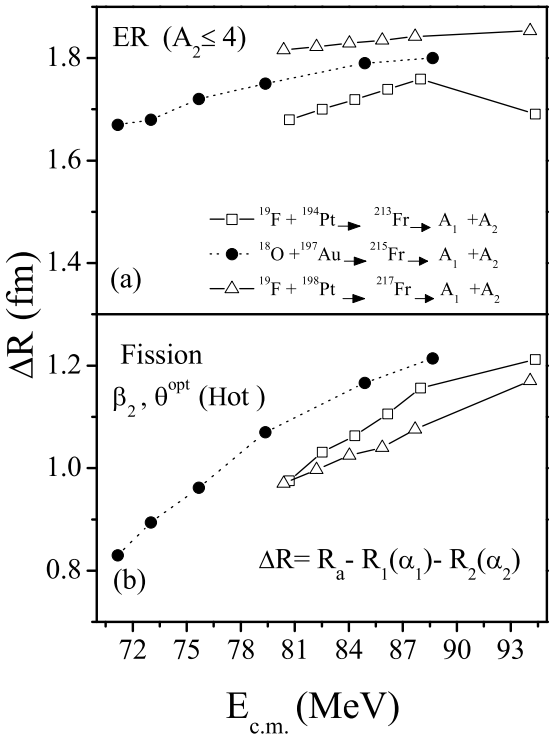

Figure 3.1 Variation of neck-length parameter ΔR with $E_{c.m.}$, obtained for (a) ER and (b) fission of compound systems ^{213,215,217}Fr*, for use of quadrupole (β_2)-deformed decay products.

3.2.1 ER and ff excitation functions and fission anisotropies in decay of Fr isotopes

First of all, we look for the energetically favored light particles (LPs), the evaporation residues (ER's), predicted by DCM for the compound nucleus ^{215}Fr* formed in ^{18}O+^{197}Au reaction and study their behavior with respect to angular momentum ℓ, and finally sum over ℓ up to ℓ_{max}. Since σ_{ER} are measured for ^{213,217}Fr* systems [26] but not for ^{215}Fr* [27], calculations are made within the DCM by using different neck-length parameters ΔR at different $E_{c.m.}$ (equivalently, E^*_{CN} or T values), assuming that ΔR for the case of ^{215}Fr* lies in between that for the ^{213}Fr* and ^{217}Fr* nuclei. Also, the range of energies being different for ^{215}Fr*, as compared to ^{213,217}Fr* isotopes, the ΔR values at lower energies are obtained by extrapolating the fitted ΔR [20] values of ^{213,217}Fr* in respect of the data of [26].

Table 3.1 The characteristic properties like the neck-length parameter ΔR and maximum angular momentum ℓ_{max}, together with cross-sections of channels contributing towards the evaporation residue (ER) cross-section and the total ER cross-section σ_{ER} predicted on the DCM for ^{215}Fr* compound nucleus formed in ^{18}O+^{197}Au reaction at various $E_{c.m.}$'s.

$E_{c.m.}$	E^*_{CN}	T	ℓ_{max}	ΔR	1n	2n	3n	^4H	σ^{Total}_{ER}
(MeV)	(MeV)	(MeV)	($\hbar$)	(fm)	(mb)	(mb)	(mb)	(mb)	(mb)
71.17	39.10	1.300	132	1.67	53.40	1.09	4.29×10^{-3}	3.24×10^{-2}	54.48
73.00	40.94	1.330	132	1.68	57.02	1.98	2.89×10^{-3}	1.67×10^{-2}	59.00
75.67	43.60	1.372	132	1.72	83.20	2.01	1.01×10^{-2}	1.13×10^{-1}	85.40
79.37	47.30	1.428	132	1.75	101.90	2.76	1.46×10^{-2}	3.60×10^{-4}	104.68
84.89	52.82	1.508	133	1.79	138.00	3.80	5.12×10^{-2}	3.02×10^{-4}	142.00
88.66	56.59	1.560	134	1.80	150.00	4.91	4.17×10^{-2}	6.20×10^{-4}	155.00

For a complete and comprehensive analysis of the decay paths of all the three ^{213,215,217}Fr* isotopes, Fig. 3.1 shows the variation of ΔR with $E_{c.m.}$, ranging from 71 to 94 MeV, for ER (Fig. 3.1(a)) and fission (Fig. 3.1(b)) processes, taking the deformed choice of decay fragments. The neck-length variations of ^{213,217}Fr* isotopes (shown in Fig. 6 of [20]) are used here to estimate the ΔR for evaporation residue path of ^{215}Fr*. For both the ER and fission processes, we notice a linear increase in ΔR with increase of $E_{c.m.}$, except at the highest one energy for ER in ^{213}Fr* system. Note that different ΔR's for the two processes of ER and ff mean that they occur in different time scales and evolve differently subject to the nature of dynamics of compound nucleus formed. As expected from the earlier calculations for ^{213,217}Fr* compound systems [20], the predicted ER channel for ^{215}Fr* requires larger ΔR in comparison to ff, as is depicted in Fig. 3.1 (compare two dotted lines), indicating that ER emission occurs earlier than the fission.

The above results are more explicitly given in Table 3.1 where the calculated contributions of ER cross-section and other parameters of the DCM are presented for ^{215}Fr*

Table 3.2 The DCM calculated fission cross-sections consisting of asymmetric mass window A_2=72-94 for ^{213}Fr* and A_2=78-94 for ^{217}Fr* (plus their complementary fragments), compared with new experimental data [28] at higher three energies. Also tabulated are the predicted ER cross sections σ_{ER} along with other characteristic quantities.

$E_{c.m.}$	E^*_{CN}	T	ℓ_{max}	$\Delta R_{fission}$ (fm)		$\sigma_{fission}$ (mb)		ΔR_{ER} (fm)	σ_{ER} (mb)
(MeV)	(MeV)	(MeV)	($\hbar$)	Extrap.	Fitted	DCM	Expt.	Extrap.	DCM
				^{19}F+^{194}Pt$\rightarrow^{213}$Fr$^* \rightarrow A_1 + A_2$					
100.27	66.97	1.703	134	1.20	1.20	622	626	1.54	8.00
102.99	69.69	1.737	135	1.28	1.22	763	765	1.50	4.89
106.61	73.31	1.781	136	1.31	1.31	857	860	1.56	11.42
				^{19}F+^{198}Pt$\rightarrow^{217}$Fr$^* \rightarrow A_1 + A_2$					
97.40	60.50	1.605	135	1.21	1.16	371	378	1.87	216
102.80	65.89	1.674	136	1.29	1.11	523	523	1.89	229
106.56	69.65	1.720	138	1.35	1.20	660	670	1.87	241

system only (for ^{213,217}Fr*, see [20]). It may be noted here that major contribution to total ER cross-section in these calculations comes from mass 1 fragment, i.e., $1n$, contributing almost 97% of σ_{ER} for all the available energies. This happens because, in DCM, $1n$ channel is, in general, preformed strongly in CN [15], in comparison to other light particles in the exit channel. Also, it is important to note that, as compared to σ_{ER} here in Table 3.1, the earlier calculations [21, 22] resulted in a nearly negligible σ_{ER} for use of ΔR_{fiss}, i.e., from fits to fission cross-sections. An experimental verification of the predicted σ_{ER} component in ^{18}O+^{197}Au reaction is thus called for.

Next, in view of earlier work on ^{213,217}Fr* systems [20], the results of calculation done using DCM for the data [28] available for the above said compound systems formed in ^{19}F+^{194,198}Pt reactions are presented. Fission cross-sections data are available at three higher energies [28], in addition to the ones reported by Mahata *et al.* [26] and used in [20], for the same reactions. However, the ER contribution is missing in this recent

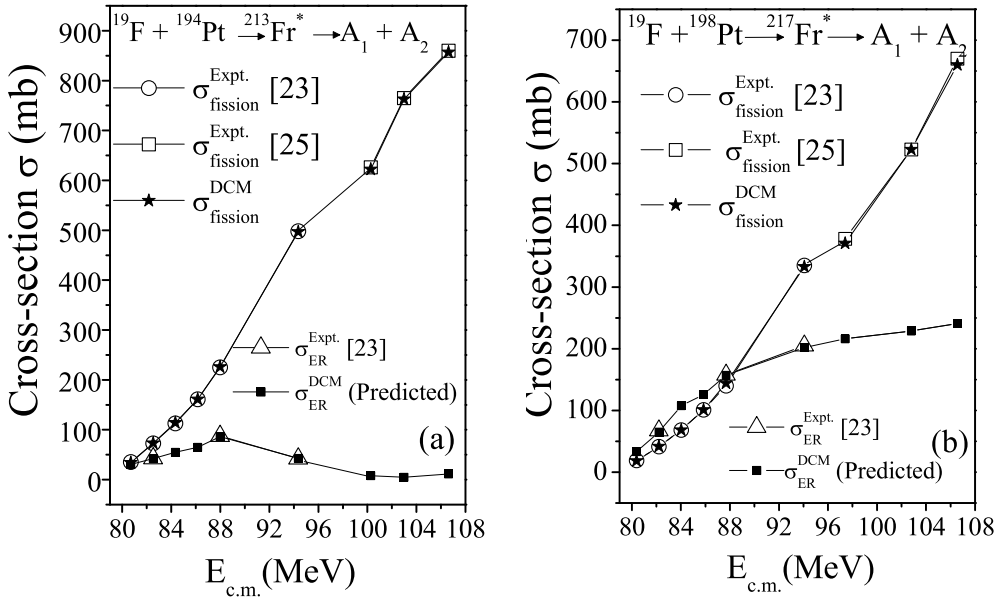

Figure 3.2 Comparison of DCM-based calculated cross sections with the experimental data for ER and fission processes in (a) ^{213}Fr* and (b) ^{217}Fr* compound system. The figure is an extension of our previous work [20] to higher three energies in reference to new $\sigma_{fission}$ data of [28] added to earlier data from [26]. σ_{ER} are also from [20], with predictions added for the highest three energies.

data [28], contrary to the measurements of Mahata *et al.* [26]. Since the earlier work [20] involved simultaneous fitting of both ER and fission cross-sections, the same approach has been carried forward here for the present calculations. For this purpose, the previously obtained neck-length, ΔR values in Fig. 3.1 are extrapolated for both the ER and fission processes in ^{213,217}Fr* nuclei. It is observed that for ΔR values in the neighborhood of extrapolated ΔR's (within a variation of <0.1 fm), the reported fission cross-sections can be easily fitted within the DCM calculations. In other words, the new data on fission cross-sections [28] is nicely reproduced within the DCM approach for the extrapolated ΔR values within a certain variance of the order of 0.1 fm. These results are presented in Table 3.2, together with the available experimental data and other calculated quantities and fitted parameters. Noting that, in the earlier experiment [26], a significant contribution of σ_{ER} is measured for both the compound systems ^{213,217}Fr*, and that σ_{ER} for ^{213}Fr* is relatively small, compared to ^{217}Fr*, at all measured energies, it is observed that the

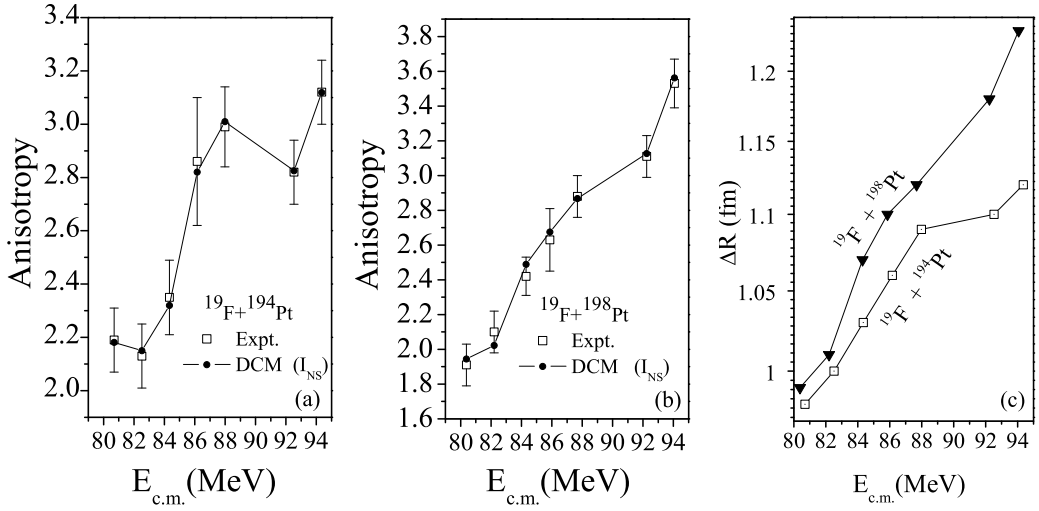

Figure 3.3 The DCM calculated fission anisotropy, compared with the experimental data [26] for (a) ^{19}F+^{194}Pt and (b)^{19}F+^{198}Pt reaction, using non-sticking limit I_{NS} of moment-of-inertia. Panel (c) shows the anisotropy-fitted neck-length parameter ΔR for the same two reactions at various $E_{c.m.}$ values.

predictions of σ_{ER} at higher energies in Table 3.2 also support this result. Fig. 3.2 depicts the complete result of σ_{ER} and $\sigma_{fission}$ calculations for ^{213,217}Fr*, i.e., Fig. 5 of [20] extended to include the present calculations in reference to recent data [28] at three higher energies. From Fig. 3.2 (and Table 3.2) it is evident that DCM based fission cross-sections σ_{fision} compare nicely with the experimental data [26,28] and the predicted ER cross-sections σ_{ER} at the highest three energies fit in to the systematics at lower energies for both the experiment and calculations [20, 26]. An experimental verification of these predictions would be of further interest.

As a next step, the behavior of fission fragment anisotropy for the reactions ^{19}F+^{194,198}Pt forming compound systems ^{213,217}Fr* is studied, in order to check the consistency of results obtained earlier [21, 22] for ^{215}Fr*. One may also notice that all the calculations presented above for ER and fission cross-sections are performed for the sticking moment-of-inertia I_S, where the ℓ_{max} is fixed for $\sigma_{LPs} \to 0$. Consequently, the ℓ_{max} involved in the reaction dynamics has much higher values, relative to ones for use of the non-sticking limit I_{NS}. It has been observed earlier [21, 22] that the sticking limit (I_S) is

Table 3.3 The fission anisotropies calculated within the use of non-sticking limit of moment-of-inertia I_{NS} in the framework of DCM, for ^{213,217}Fr* compound systems formed in ^{19}F+^{194,198}Pt reactions at various $E_{c.m.}$'s, compared with the experimental data [26].

$E_{c.m.}$ (MeV)	E^*_{CN} (MeV)	T (MeV)	ℓ_{max} ($\hbar$)	ΔR (fm)	Anisotropy A DCM	Expt.
			^{19}F+^{194}Pt$\rightarrow^{213}$Fr*			
80.69	47.39	1.436	24	0.98	2.18	2.19
82.51	49.21	1.463	24	1.00	2.15	2.13
84.34	51.04	1.489	26	1.03	2.32	2.35
86.16	52.86	1.515	32	1.06	2.82	2.86
87.98	54.68	1.541	33	1.09	3.01	2.99
92.53	59.23	1.603	33	1.10	2.82	2.82
94.35	61.05	1.627	34	1.12	3.11	3.12
			^{19}F+^{198}Pt$\rightarrow^{217}$Fr*			
80.38	43.47	1.376	21	0.99	1.94	1.91
82.20	45.30	1.391	22	1.01	2.02	2.10
84.40	47.12	1.418	27	1.07	2.48	2.42
85.86	48.95	1.445	28	1.10	2.67	2.63
87.68	50.77	1.472	29	1.12	2.86	2.88
92.24	55.34	1.535	35	1.18	3.12	3.11
94.06	57.16	1.560	38	1.23	3.56	3.53

more appropriate for obtaining fusion-fission cross-sections, whereas I_{NS} is preferred for the fission anisotropy calculations.

Figs. 3.3(a), 3.3(b) and Table 3.3 show the variation of DCM-calculated fission fragment anisotropies within the SSPM approach [6] for the reactions ^{19}F+^{194,198}Pt, as a function of $E_{c.m.}$, compared with the experimental data [26]. Interestingly, DCM calculated anisotropies for use of I_{NS} limit of moment-of-inertia show nice agreement with the data. In general, the experimental numbers for total angular momentum ℓ_{max} are based on the moment-of-inertia calculated by using non-sticking (I_{NS}=μR^2) approach where the use of reduced mass alone corresponds to the supposition that the emission of fragment is prompt [23]. As a further check, it is noticed that the anisotropy-fitted ΔR, plotted in Fig. 3.3(c), for both the reaction channels, vary almost as a smooth function of $E_{c.m.}$,

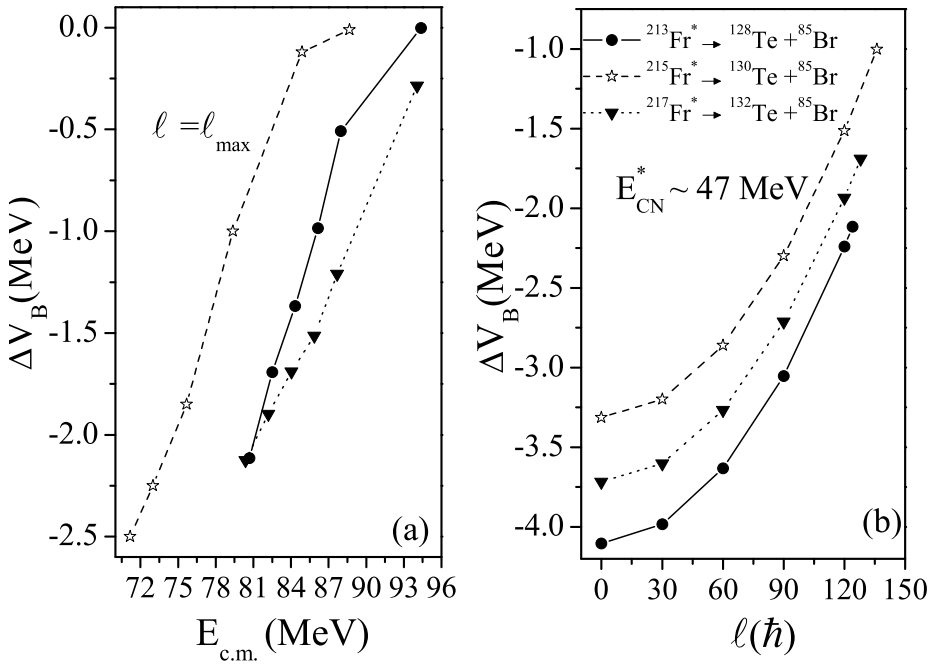

Figure 3.4 (a) The barrier-lowering parameter ΔV_B as a function of $E_{c.m.}$ for the decay of ^{213,215,217}Fr* to most probable ^{128,130,132}Te+^{85}Br fragments at ℓ=ℓ_{max}. (b) Variation of ΔV_B as a function of angular momentum ℓ ($\hbar$) at comparable $E^*_{CN}\sim$ 47 MeV using β_2-deformed choice of fragments.

showing a similar behavior as in the case of fission (refer, Fig. 3.1). This simply means that the variation of ΔR with $E_{c.m.}$ is independent of the use of I_S or I_{NS}, and a closer look of Fig. 3.3 suggests that the neck-length parameter ΔR follows the variation pattern of fission fragment anisotropy. For ^{213,217}Fr* systems, due to the use of I_{NS} approximation the anisotropies are fitted at a much smaller ℓ_{max} values, presented in Table 3.3. This observation is consistent with the earlier result of Ref. [21, 22] for ^{215}Fr*, which implies the fact that moment-of-inertia plays an important role regarding the dynamics involved in heavy-ion reactions.

Another quantity of interest is the variation of barrier modification parameter ΔV_B, plotted as a function of $E_{c.m.}$ in Fig. 3.4(a). This property of 'barrier lowering' at sub-barrier energies is an in-built property of the DCM which has a direct dependence on the corresponding values of neck-length parameter (ΔR) used to fit the available data.

It is relevant to mention here that ΔV_B is plotted for the decay of $^{213,215,217}Fr^*$ nuclei to most probable fission fragments $^{128}Te+^{85}Br$, $^{130}Te+^{85}Br$ and $^{132}Te+^{85}Br$, respectively, for the deformed choice of fragments. It is observed from Fig. 3.4(a) that at a given $E_{c.m.}$ value, the barrier modification ΔV_B is least for $^{215}Fr^*$ followed by $^{213}Fr^*$ and $^{217}Fr^*$. No direct isospin (N/Z ratio) dependence on ΔV_B is observed possibly due to the fact that $^{215}Fr^*$ and $^{213,217}Fr^*$ experiments were performed independently, over different range of energies. Also ΔV_B is calculated at different ℓ-values upto the ℓ_{max} in Fig. 3.4(b) for all the three reaction channels at E^*_{CN} ~47 MeV. It is evident that ΔV_B keeps on increasing with a decrease in ℓ value and is observed to be least at higher angular momentum value. This observation clearly indicates the importance of ΔV_B at lower ℓ-values, particularly at below barrier region.

Apparently, the $^{215}Fr^*$ isotope is formed in three different entrance channels [27, 28], using ^{11}B, ^{18}O and ^{19}F projectiles, whereas $^{213,217}Fr^*$ systems are formed due to ^{19}F based reactions only [26]. Although a comparative analysis of ^{11}B and ^{18}O channels in the context of $^{215}Fr^*$ system was worked out earlier [21, 22], in this chapter the reactions involving ^{19}F beam have been addressed. Thus exploration of the behavior of ^{19}F entrance channel in context of $^{215}Fr^*$ nucleus is of prime interest in the present set of calculations. In the following, a comparative analysis is made for the decay of $^{215}Fr^*$ formed in $^{19}F+^{196}Pt$ [28] and $^{18}O+^{197}Au$ [21, 22] reaction channels at a comparable excitation energy E^*_{CN} ~47 MeV (T=1.429 MeV) in reference to available data. The variation of fragmentation potential $V(\eta)$, preformation probability P_0, and decay barrier height are investigated in order to reveal useful information about the dynamics involved in the reactions under consideration.

Fig. 3.5(a) shows the variation of fragmentation potential for the decay of $^{215}Fr^*$ into various mass fragments at different ℓ-values, in reference to the fission cross-section

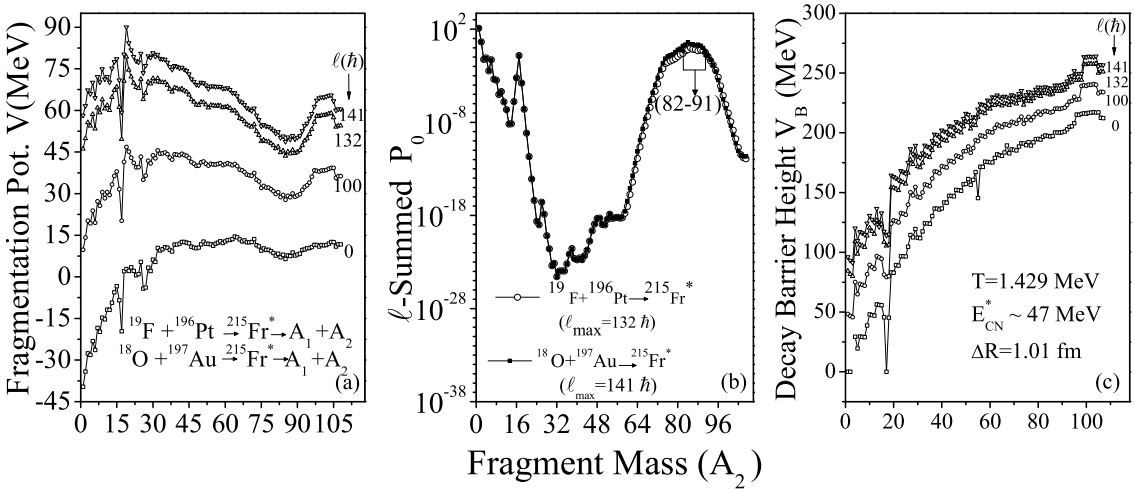

Figure 3.5 (a) The variation of fragmentation potential as a function of light-fragment mass number A_2, at different ℓ-values, for ^{19}F+^{196}Au (ℓ_{max}=132 $\hbar$) and ^{18}O+^{197}Pt (ℓ_{max}=141 $\hbar$) channels forming ^{215}Fr* system at a comparable excitation energy. (b) The ℓ-summed fragment preformation probability P_0 plotted at ℓ_{max} values for the two reactions. Panel (c) is same as for Panel (a) but for the decay barrier height V_B.

data [27, 28] of ^{19}F+^{196}Pt and ^{18}O+^{197}Au reactions at $E^*_{CN} \sim 47$ MeV. Note that for both the reactions, an asymmetric fission window, arising due to deformed (β_2) choice of fragments seems in opertaion, where fragments in the mass range A_2=82-91 (plus complementary heavy fragments) contribute toward fission process. This fission fragment window is same as taken for comparative analysis of ^{11}B and ^{18}O channels in [21, 22]. The ΔR values, obtained to fit the available data, are 0.96 fm and 1.07 fm [21, 22], respectively, for the ^{19}F+^{196}Pt and ^{18}O+^{197}Au entrance channels. Since the two values are very close to each other, an average i.e., ΔR=1.01 fm has been taken to fit the fission cross section data. From Fig. 3.5(a), it is observed that although the characteristic behavior of potential energy surfaces is different at lower versus higher ℓ-values, the structure of the fragmentation potential does not change much in going from ℓ=132 $\hbar$ (the ℓ_{max} value for ^{19}F+^{196}Pt) to 141 $\hbar$ (the ℓ_{max} value for ^{18}O+^{197}Au). This observation clearly indicates that the decay of ^{215}Fr* is almost independent of the choice of entrance channel, like for ^{11}B and ^{18}O beams in [21, 22]. At lower ℓ-values, as expected, the contribution of ER

is more prominent than the fission fragments, which otherwise start appearing only at higher ℓ-values.

Based on the fragmentation potential in Fig. 3.5(a), the summed up preformation probability P_0 over ℓ-values, as a function of light mass fragment A_2 for both the reaction channels at two different $E_{c.m.}$'s forming the same CN at about the same E^*_{CN} ($\sim$ 47 MeV) is depicted in Fig. 3.5(b). The ℓ-summed P_0 means the sum of probabilities of a fragment that is preborn in the CN prior to the decay process, over all contributing angular momentum states up to ℓ_{max}. It is relevant to mention here that, in the DCM, cross sections follow the trend of preformation probability P_0 [21, 22], which means that structure effects are contained only in P_0. From Fig 3.5(b) it is observed that the summed values of P_0 over ℓ are almost similar for both the reactions, which further indicates no significant signature of entrance channel effects.

To investigate further, in Fig. 3.5(c) the barrier heights $V_B(A_2)$ is plotted at different ℓ's for the decay of ^{215}Fr* nucleus formed in the above mentioned reaction channels. It is clear from this figure that V_B increases and hence the decay probability decreases with decrease in mass asymmetry, in agreement with the earlier calculations of Refs. [21,22] for the case of heavy nuclear system having fission as its prominent decay channel. On the other hand, the decay barrier heights almost overlap each other for ℓ_{max}=132 and 141$\hbar$, i.e., independent of whether the compound nucleus ^{215}Fr* is formed from ^{19}F+^{196}Pt or ^{18}O+^{197}Au entrance channel. In other words, the DCM based calculations governed via fragmentation profile, preformation factor and decay barrier height etc., suggest that the decay of ^{215}Fr* is independent of the choice of entrance channel effects.

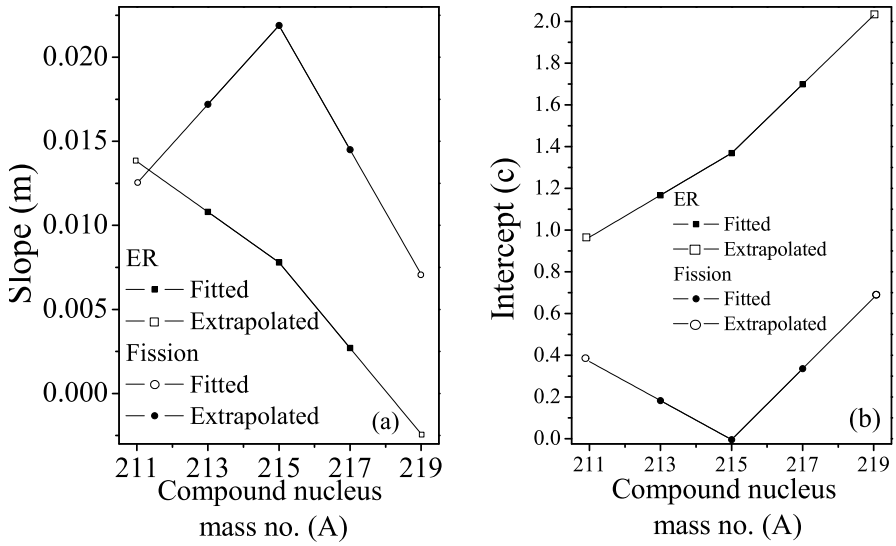

Figure 3.6 (a) Slope and (b) intercept as a function of compound nucleus mass number A for straight line fit of ΔR as a function of E^*_{CN}. Filled symbols are fitted values and open symbols are extrapolated values.

3.2.2 Role of shell effects in decay fragments of Fr isotopes

In the earlier work [20], shell closure effects of the decay fragments are shown to play an important role in context to fragmentation process of ^{213,217}Fr* nuclei. In the present study the decay of ^{215}Fr*, as well as the two neighboring isotopes ^{211,219}Fr* formed in the proposed reactions ^{19}F+^{192}Pt and ^{19}F+^{200}Pt are calculated in order to carry out a comprehensive analysis of the possible shell closure effect of decaying fragments. In other words, the isospin (N/Z ratio) effects of various mass distributions is worked out by exploring the behavior of preformation factor for $^{211-219}$Fr* isotopes.

In reference to experimental data [26, 27], the common compound nucleus excitation energy E^*_{CN} for all the three ^{213,215,217}Fr* systems is same ($\sim$47 MeV). Therefore, a comparative study of the decay mechanism of various odd-mass Fr isotopes is carried out at E^*_{CN} $\sim$47 MeV. In order to predict the ER and fission cross-sections for new isotopes ^{211}Fr* and ^{219}Fr*, the slope (m) and intercept (c) values obtained via straight line fits of the ΔR values of ^{213}Fr*, ^{215}Fr* and ^{217}Fr* (shown in Fig. 3.1) are extrapolated using the

Table 3.4 DCM predicted evaporation residue cross sections (σ_{ER}) and fission cross sections ($\sigma_{fission}$) for ^{211,219}Fr* isotopes at the extrapolated ΔR values and common excitation energy E^*_{CN} ∼47 MeV.

Compound Nucleus	$E_{c.m.}$ (MeV)	T (MeV)	ℓ_{max} ($\hbar$)	ΔR_{fiss} (fm)	$\sigma_{fission}$ (mb)	ΔR_{ER} (fm)	σ_{ER} (mb).
^{211}Fr*	81.84	1.437	118	0.95	22.93	1.61	5.06
^{219}Fr*	84.38	1.410	123	1.00	16.48	1.86	3.86

equation

$$\Delta R = mE^*_{CN} + c \tag{3.1}$$

The straight line fits to both the ER and fission processes are obtained in the following form of polynomials,

for ^{213}Fr: $\Delta R^{ER} = 0.0108E^*_{CN} + 1.1674$; $\Delta R^{fission} = 0.0172E^*_{CN} + 0.1826$;

for ^{215}Fr: $\Delta R^{ER} = 0.0078E^*_{CN} + 1.369$; $\Delta R^{fission} = 0.0219E^*_{CN} - 0.0044$;

and for ^{217}Fr: $\Delta R^{ER} = 0.0027E^*_{CN} + 1.6992$; $\Delta R^{fission} = 0.0145E^*_{CN} + 0.3354$.

Fig. 3.6 shows a plot of the slope m (Fig. 3.6(a)) and intercept c (Fig. 3.6(b)), and their extracted values, for ER and fission fits obtained above, as a function of the CN mass number A. Here the filled symbols represent m and c values for ^{213,215,217}Fr* isotopes, and the open symbols represent the extrapolated values for ^{211,219}Fr* isotopes. Using the extrapolated values of m and c in Eq. (3.1), at the same $E^*_{CN} \sim 47$ MeV, the values of neck length parameter ΔR are obtained, and used in turn to calculate σ_{ER} and $\sigma_{fission}$ for ^{211,219}Fr*. The results so obtained are given in Table 3.4 where one may see that the DCM predicts the contribution of ER as well as fission cross-sections for ^{211,219}Fr* rather small, compared to observed experimental data [26, 27] for ^{213,215,217}Fr* isotopes.

Finally, in order to analyze the role of magic shells in mass distributions, the fragment formation yields P_0 are calculated and presented in Fig. 3.7 at the two extreme ℓ values

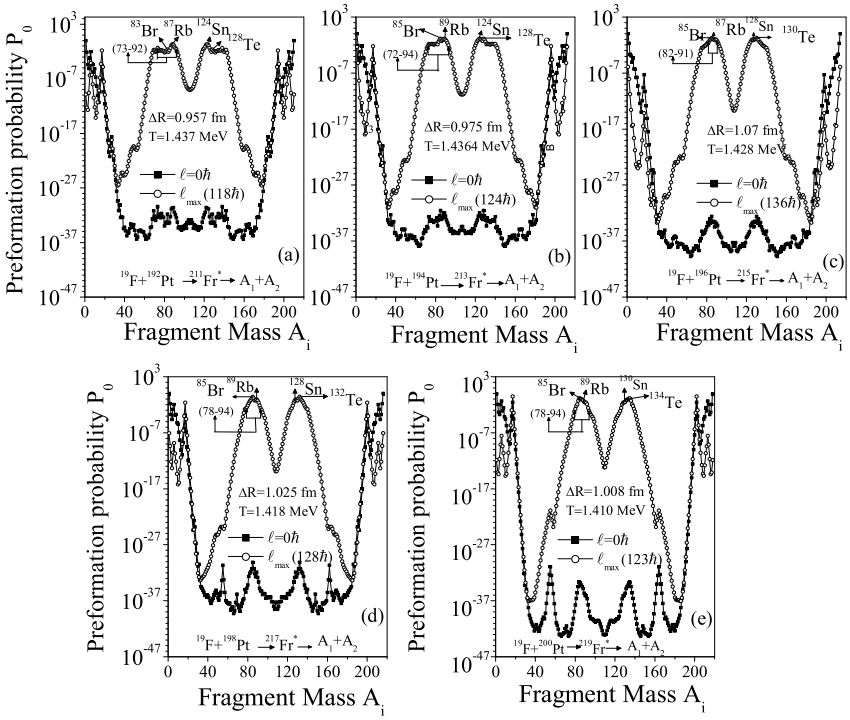

Figure 3.7 Fragment preformation probability P_0 plotted as a function of fragment mass A_i ($i = 1, 2$) for different compound systems (a) ^{211}Fr*, (b) ^{213}Fr*, (c) ^{215}Fr*, (d) ^{217}Fr*, and (e) ^{219}Fr* at E^*_{CN}∼47 MeV, showing the presence of shell effects in all cases.

for the decay of various isotopes of Fr at a similar excitation energy E^*_{CN}∼47 MeV . The shell effects, in all the odd-mass Fr isotopes $^{211-219}$Fr*, arise due to the deformed closed shell around light-fragment charge Z_2=36 (actually at Z_2=35 and 37), and spherical shell closure around heavy-fragment charge Z_1=50 (actually at Z_1= 52 and 50). This is explicitly marked in Fig. 3.7 in terms of two strong maxima (or, equivalently, double minima in Fig. 1 of fragmentation potential $V(A_2)$ in [20]) and as a hump/ shoulder for both the light and heavy-mass fragments. This hump seems to be a slightly more dominant for ^{211}Fr* (with neutron number N=124) followed by ^{213}Fr* (N=126) decay and goes on decreasing with the increase in N/Z ratio. The above observation enables us to conclude that shell closure effect of the decay fragments play an important role in all the above studied Fr isotopes.

It is relevant to remind here that the authors of experimental works [31, 32] were

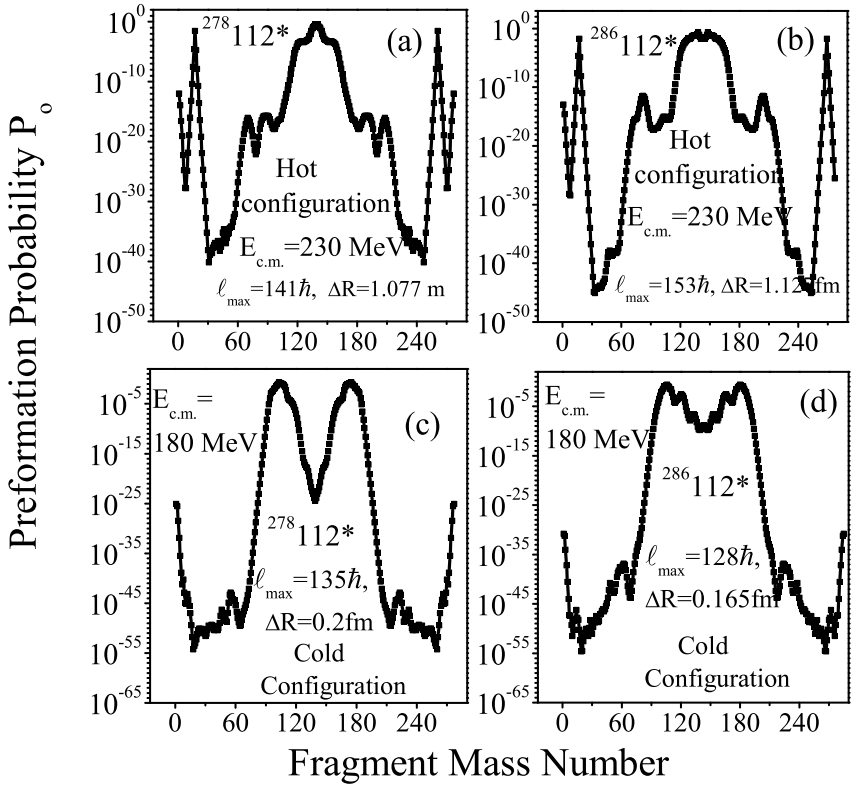

Figure 3.8 Variation of preformation probability P_0 as a function of fragment mass A_i (i = 1, 2) for different compound systems ^{40,48}Ca+^{238}U→ ^{278,286}112* at (a,b) highest energy, $E_{c.m.}$=230 MeV using hot equatorial orientation and (c,d) at sub-barrier energy $E_{c.m.}$=180 MeV for the use of cold polar orientation.

interested in exploring the shell effects of compound nucleus ^{213}Fr*, an evident result of N=126 magicity in this CN. However, the DCM allows us to study the shell effects in decay products only, and hence, there is no way to study the role of magic proton/ neutron number of the CN in this model. Another important observation is that for all the Fr isotopes studied here, the fission pattern remains the same, i.e., asymmetric and the fragments in the mass range A_2=72-94 seem to be contributing towards fission process. However, one may note that no individual fragments are identified in the available experiments [26, 27]. Furthermore, it is generally believed that shell effects are washed away at higher excitation energies, which means that it will be of further interest to investigate the gradual variation of shell effects with the CN excitation energy.

Table 3.5 The DCM calculated fission cross-sections for ^{40,48}Ca + ^{238}U reactions. Also tabulated are the neck-length parameter Δ R, ℓ_{max} and the overestimated cross-sections representing quasi-fission contribution for below barrier energies using cold polar orientation.

$E_{c.m.}$ (MeV)	ΔR_{fiss} (fm)	ℓ_{max} ($\hbar$)	$\sigma^{DCM}_{fission}$ (mb)	σ^{DCM}_{QF} (mb)	$\sigma^{Expt.}_{Fusion}$ (mb)
		^{40}Ca+^{238}U$\rightarrow^{278}$112*			
195	0.488	140	39.6	-	39.91
190	0.302	138	16.9	-	16.39
185	0.190	136	13.5	10.98	2.52
180	0.200	135	13.8	13.8	0.294
		^{48}Ca+^{238}U$\rightarrow^{286}$112*			
190	0.533	121	19.7	-	19.8
185	0.100	129	4.18	2.03	2.15
180	0.165	128	4.86	4.728	0.132

3.2.3 Role of Hot Equatorial and Cold Polar orientation

Next, DCM has been applied to investigate the role of hot (equatorial) compact and cold (polar) elongated orientation in context to superheavy Z=112 isotopes. Fig. 3.8 illustrates variation of preformation probability as a function of fragment mass A_2 at above barrier energy for the use of hot (equatorial) compact orientation (panel a,b) and at sub-barrier energy using cold (polar) elongated configuration (panel c,d). The calculations are done in reference to recent experiment [30] by taking quadrupole (β_2) deformations into account. Comparing Fig. 3.8 (a,b) with 3.8 (c,d), it is observed that at above barrier energies, the hot configuration results into symmetric structure of fission fragments while in sub-barrier region, owing to the preferred cold orientation the preformation probability P_0 change drastically showing the suppression in magnitude of symmetric fragments and dominance of asymmetric fragments. This suggests that for cold orientation, fusion is perhaps not the only process and some competing mechanism such as quasi-fission may

also be observed. Consequently, for the use of cold orientation, the DCM calculated fission cross-sections in sub-barrier region are over-estimated in comparison to the experimental data as shown in Table 3.5. The enhanced fission cross-section signifies the presence of quasi-fission contribution which is more for neutron deficient ^{278}112 nucleus.

3.3 Summary

Summarizing, in order to focus on the missing aspects of both the evaporation residue, fusion-fission processes and the fission fragment anisotropies, the study of odd-mass nuclear systems ^{213,217}Fr* formed in ^{19}F+^{194,198}Pt reactions and ^{215}Fr* formed in ^{18}O+^{197}Au and more recently in ^{19}F+^{196}Pt reaction [20–22] is extended. The methodology used here is based on the dynamical cluster-decay model (DCM) where effects of both the deformations and orientations of nuclei/ fragments are included, with deformations taken upto β_2, and 'optimum' orientations.

The ER cross-sections are predicted for ^{215}Fr* nucleus over a wide range of incident center-of-mass energy. In addition, the fission cross-sections are very well accounted and the contribution of ER cross-sections is predicted in reference to the latest data [28] available for ^{213,217}Fr* systems at higher three energies, in comparison to the earlier measurements of Mahata *et al.* [26]. Furthermore, in order to check the consistency of previous results for the decay of ^{215}Fr* [21, 22], the work is extended to two different reaction channels, ^{19}F+^{196}Pt and ^{18}O+^{197}Au. On comparing the results of calculations at a comparable excitation energy E^{*}_{CN}=47 MeV for the two reaction channels, it is observed that CN formation is independent of different entrance channels. The mass distributions of ^{211,213,215,217,219}Fr* are also worked out within the DCM, which clearly signifies the importance of shell effects of decay fragments in the odd-mass Fr isotopes, supporting the

result of earlier work [20] for ^{213,217}Fr* isotopes. Additionally, the role of hot (equatorial) compact and cold (polar) elongated orientation is studied for superheavy Z=112 isotopes and it is observed that at sub-barrier region the cold orientation results into asymmetric mass distribution which is otherwise symmetric for hot configuration. Also the fission cross-sections are over estimated for the use of cold orientation, indicating the presence of quasi-fission contribution.

It may be noted that the static $\beta_{2i}(0)$ deformations within optimum (θ_i^{opt}) orientation approach are used in the decay analysis presented in this chapter. It will be of further interest to investigate the dynamic deformations β_{2i}(T) in the decay path of composite system formed in heavy ion reactions. This work is carried out by investigating the dynamics of ^{6}Li+^{144,152}Sm reactions and the results are discussed in chapter 4.

Bibliography

[1] R. J. Charity, M. A. McMahan, G. J. Wozniak, R. J. McDonald, L. G. Moretto, D. G. Sarantites, L. G. Sobotka, G. Guarino, A. Pantaleo, F. Fiore, A. Gobbi, and K. D. Hildenbrand, Nucl. Phys. A **483**, 43 (1988).

[2] J. Gomez del Campo, R. L. Auble, J. R. Beene, M. L. Halbert, H. J. Kim, A. D'Onofrio, and J. L. Charvet, Phys. Rev. C **43**, 2689 (1991).

[3] S. J. Sanders, D. G. Kovar, B. B. Back, C. Beck, D. J. Henderson, R. V. F. Janssens, T. F. Wang, and B. D. Wilkins, Phys. Rev. C **40**, 2091 (1989).

[4] S. J. Sanders, Phys. Rev. C **44**, 2676 (1991).

[5] T. Matsuse, C. Beck, R. Nouicer, and D. Mahboub, Phys. Rev. C **55**, 1380 (1997).

[6] R. Vandenbosch and J. R. Huizenga, *Nuclear Fission*, Academic Press, New York (1973).

[7] L. G. Moretto, Nucl. Phys. A **247**, 211 (1975).

[8] G. G. Adamian, N. V. Antonenko, W. Scheid, and V. V. Volkov, Nucl. Phys. A **633**, 409 (1998) .

[9] V. I. Zagrebaev, Y. Aritomo, M. G. Itkis, Yu. Ts. Oganessian, and M. Ohta, Phys. Rev. C **65**, 014607 (2001).

[10] V. I. Zagrebaev, Yu. Ts. Oganessian, M. G. Itkis, and W. Greiner, Phys. Rev. C **73**, 031602(R) (2006).

[11] R. K. Gupta, M. Balasubramaniam, R. Kumar, N. Singh, M. Manhas, and W. Greiner, J. Phys. G: Nucl. Part. Phys. **31**, 631 (2005).

[12] R. K. Gupta, M. Manhas, W. Greiner, Phys. Rev. C **73**, 054307 (2006).

[13] R. K. Gupta, M. Balasubramaniam, R. Kumar, D. Singh, S. K. Arun, and W. Greiner, J. Phys. G: Nucl. Part. Phys. **32**, 345 (2006).

[14] R. K. Gupta, S. K. Arun, R. Kumar, and Niyti, Int. Rev. Phys. (IREPHY) **2**, 369 (2008).

[15] S. K. Arun, R. Kumar, and R. K. Gupta, J. Phys. G: Nucl. Part. Phys. **36**, 085105 (2009).

[16] G. Kaur and M. K. Sharma, Phys. Rev. C **87**, 044601 (2013).

[17] G. Kaur and M. K. Sharma, Nucl. Phys. A **884**, 36 (2012).

[18] G. Kaur, N. Grover, K. Sandhu, and M. K. Sharma, Nucl. Phys. A **927**, 232 (2014).

[19] M. Kaur, M. K. Sharma, and R. K. Gupta, Phy. Rev. C **86**, 064610 (2012).

[20] M. K. Sharma, S. Kanwar, G. Sawhney, and R. K. Gupta, Phys. Rev. C **85**, 064602 (2012).

[21] M. K. Sharma, G. Sawhney, R. K. Gupta, and W. Greiner, J. Phys. G: Nucl. Part. Phys. **38**, 105101 (2011);

[22] M. K. Sharma, G. Sawhney, S. Kanwar, and R. K. Gupta, Mod. Phys. lett. **A 25**, 2022 (2010).

[23] B. B. Singh, M. K. Sharma, and R. K. Gupta, Phy. Rev. C **77**, 054613 (2008).

[24] G. Sawhney, G. Kaur, M. K. Sharma, and R. K. Gupta, Phys. Rev. C **88**, 034603 (2013).

[25] K. Sandhu, G. Kaur, and M. K. Sharma, Nucl. Phys. A **921**, 114 (2014).

[26] K. Mahata, S. Kailas, A. Shrivastava, A. Chatterjee, P. Singh, S. Santra, and B. S. Tomar, Phys. Rev. C **65**, 034613 (2002).

[27] S. Appannababu, S. Mukherjee, N. L. Singh, P. K. Rath, G. K. Kumar, R. G. Thomas, S. Santra, B. K. Nayak, A. Saxena, R. K. Choudhury, K. S. Golda, A. Jhingan, R. Kumar, P. Sugathan, and H. Singh, Phys. Rev. C **80**, 024603 (2009).

[28] V. Singh, B. R. Behera, M. Kaur, A. Jhingan, P. Sugathan, D. Siwal, M. Oswal, S. Goyal, K. P. Singh, A. Saxena, and S. Kailas, in Proceedings of the Department of Atomic Energy Symp. on Nucl. Phys. **57**, 400 (2012).

[29] K. Nishio, H.Ikezoe, S. Mitsuoka, I. Nishinaka, Y. Nagame, Y. Watanabe, T. Ohtsuki, K. Hirose, and S. Hofmann, Phys. Rev. C **77**, 064607 (2008).

[30] K. Nishio, S. Mitsuoka, I. Nishinaka, H. Makii Y. Wakabayashi,H. Ikezoe, K. Hirose,T. Ohtsuki,Y. Aritomo, and S. Hofmann, Phys. Rev. C **86**, 034608 (2012).

[31] V. Singh, B. R. Behera, M. Kaur, P. Sugathan, K. S. Golda, A. Jhingan, J. Sadhukhan, D. Siwal, S. Goyal, S. Santra, A. Kumar, R. K. Bhowmik, M. B. Chatterjee, A. Saxena, S. Pal, and S. Kailas, Phys. Rev. C **86**, 014609 (2012).

[32] V. Singh, B. R. Behera, M. Kaur, A. Kumar, P. Sugathan, K. S. Golda, A. Jhingan, M. B. Chatterjee, R. K. Bhowmik, D. Siwal, S. Goyal, J. Sadhukhan, S. Pal, A. Saxena, S. Santra, and S. Kailas, Phys. Rev. C **87**, 064601 (2013).

Chapter 4

Decay of intermediate mass nuclei formed in ^{6}Li induced reactions

In the previous chapter, the decay processes of nuclei lying in heavy mass region were studied in context to odd-mass Fr and Z=112 isotopes respectively. The entrance channel effect, shell closure effect and anisotropy was explored for Fr isotopes while the role of hot (equatorial) compact and cold (polar) elongated orientation degree of freedom was analyzed for Z=112 isotopes. Carrying this study further, this chapter aims to inspect the dynamics of intermediate mass ^{150,158}Tb* nuclei using the dynamical cluster decay model (DCM) [1–8] It is worth mentioning that the calculations in chapter 3 involve only the static deformations [9], while in the present chapter the effect of temperature dependent dynamic deformations [10, 11] is also studied. In addition to this the role of level density parameter, N/Z ratio and effect of orientation on dynamics of intermediate mass nucleus is duly addressed. Besides this the decay cross-sections obtained through incomplete fusion (ICF) process are also studied. This work is carried out in reference to recent experiment [12,13] and is published in [14]. In the following a general introduction in reference to loosely bound projectile and deformed target is given in Sec.4.1, the results

are presented in Sec.4.2 and summarized in Sec.4.3.

4.1 Introduction

The study of reactions induced by loosely bound nuclei are of immense importance so far as the heavy ion reaction dynamics is concerned. This is because, in such reactions the fusion process has a more intricate character because of high probability of breakup, caused due to low binding energy of loosely bound nuclei (e.g. $^{6,7}Li$, ^{9}Be etc.) involved. This may be attributed to the anomalous structure of loosely bound nuclei, owing to which their behavior towards the fusion process is different from that of tightly bound nuclei. Thus, understanding the dynamics of loosely bound nuclei is of considerable importance which can be studied by systematic analysis of decay processes involved in such reactions. Moreover, for an overall picture of structure effects and the dynamics involved in such reactions, one also needs to investigate the effect of deformations and orientations of the colliding nuclei as well as the decaying fragments.

In a recent experiment [12], with the use of ^{6}Li beam on ^{152}Sm target, the fusion excitation functions have been measured for ^{158}Tb* nucleus at various incident energies varying from E_{lab}=20-40 MeV (equivalently $E_{c.m.}$ =19.2-38.5 MeV) lying across the Coulomb barrier. The complex process of fusion involving deformed light mass projectile and heavy target nucleus can be best understood via the decay study of compound nucleus formed. In view of this, the decay cross-sections for ^{158}Tb* formed in ^{6}Li +^{152}Sm reaction have been tested in framework of dynamical cluster-decay model (DCM) [1–8]. In general, the fusion cross-sections are considered to have contribution from evaporation residue, σ_{ER} consisting of multiple light particles ($A_2 \leq 4$) such as neutron, proton, alpha particle and gamma-ray etc. and from the fission cross-section, $\sigma_{fission}$ i.e., σ_{fusion}=σ_{ER}+$\sigma_{fission}$

along with contribution of some non-compound nucleus (nCN) process, if any. However, for the lanthanide system under consideration the fusion cross-sections are observed to have contribution from ER alone, while the fission contribution is negligible. Thus for ^{6}Li+^{152}Sm$\rightarrow$^{158}Tb* reaction, $\sigma_{fusion}\sim\sigma_{ER}$. Since, the projectile, target involved and the compound nucleus formed are all deformed so the role of deformations and orientations is expected to be of importance for the present system. Interestingly, DCM, having both these degrees of freedom included into it, has the ability to provide furtherance for the study of such reactions. Another interesting aspect of the reaction under consideration is the possible role of shell effects [15] in the decaying fragments. The presence of such effects suggest the involvement of some competing non-compound nucleus (nCN) process in addition to the compound nucleus decay [16]. The role of deformations and the shell closure effects is explored by making a comparative study of the decay of ^{158}Tb* nucleus with ^{150}Tb* formed in reaction induced by ^{6}Li on spherical target ^{144}Sm [13]. Besides this, suppression in measured fusion cross-sections [12] for ^{158}Tb* nucleus is associated with incomplete-fusion (ICF) process and the same is studied here.

The urge behind this study is to understand (i) the indispensable role of deformation of the colliding as well as decaying fragments. To pursue with it, the deformation effects on decaying fragments are studied by taking into account spherical and quadrupole (β_2) deformed choice of fragmentation. The specific role of static $\beta_2(0)$ and dynamic β_2(T) deformations is also explored. Apart from deformations, the role of hot (equatorial) compact and cold (polar) elongated orientations is extended to intermediate mass region.(ii) the comparative study of decay patterns of isotopes of lanthanide system i.e. ^{150,158}Tb* formed in ^{6}Li+^{144,152}Sm reactions. The main focus is to see how the shape of target nucleus influences the decay pattern of a composite system, beside having an eye on the emergence of shell closure effect of decaying fragments as experienced in case of Fr iso-

topes, discussed in chapter 3.(iii) the role of loosely bound projectile ^{6}Li which undergoes break-up and brings into account the incomplete fusion process (ICF).

4.2 Calculations

The fusion cross-sections of compound nucleus ^{158}Tb* formed in ^{6}Li +^{152}Sm reaction have been investigated recently [12] at different incident energies varying from $E_{c.m.}$ =19.2 MeV-38.5 MeV, lying across the Coulomb barrier and the same is tested using dynamical cluster-decay model (DCM). The evaporation residue decay mode forms an unambiguous tool for the study of nuclear reactions and the same is explored in this chapter, as the measured complete fusion cross-sections are mainly associated with ER contribution. For ^{6}Li +^{152}Sm reaction the role of deformations (across the barrier) and orientations (particularly at below barrier region) is studied for which the calculations have been done using spherical choice of fragmentation, with inclusion of static deformation $\beta_{2i}(0)$ and with dynamic deformed β_{2i}(T) choice of fragmentation in reference to optimum (θ_i^{opt}) orientation approach. For deformations $\beta_{\lambda i}$, the static deformations in DCM are taken from the theoretical estimates of Möller and Nix [9], and the temperature dependence in the deformations are considered via [10, 11], and are given as:

$$\beta_{\lambda i}(T) = exp(-T/T_0)\beta_{\lambda i}(0), \tag{4.1}$$

where $\beta_{\lambda i}(0)$ are the static deformations and T_0 is the temperature of nucleus at which shell effects start to vanish. Also, the optimum orientations θ_i^{opt} of the hot fusion process for β_{2i} choice of fragmentation are taken from Ref. [1].

In the following, the role of static and dynamic quadrupole deformations is discussed. The application of DCM in reference to ^{150}Tb* formed by spherical target ^{144}Sm instead of

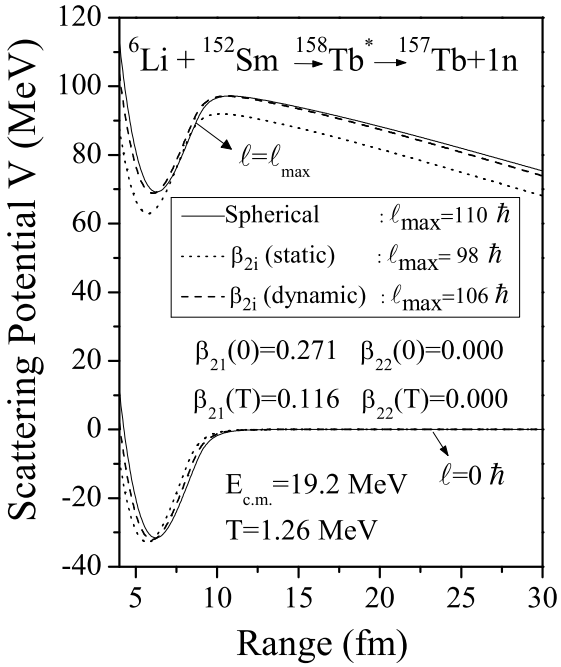

Figure 4.1 The scattering potential $V(R)$ for the decay of ^{158}Tb$^{*}\rightarrow^{157}$Tb+1n channel at extreme ℓ-values for spherical, static $\beta_2(0)$ deformed and dynamic β_2(T) deformed choice of fragmentation.

deformed target ^{152}Sm is duly addressed. In addition to the effect of target deformation, this comparison helps us to investigate the isotopic effect that is produced due to the addition of '8n' while going from ^{150}Tb* to ^{158}Tb* nucleus. Also, the shell closure effect of decaying fragments is analyzed and the role of deformed shape of target nucleus seem evident in the preformation profile of Tb isotopes. Besides this, the decay cross-sections obtained through incomplete fusion (ICF) process are also studied.

Following the experimental data [12] the ER cross-sections are addressed by considering the spherical and quadrupole deformed choice of fragmentation within the optimum orientation approach. As an extension to work presented in chapter 3, here the role of deformations in decaying fragments is studied by considering three different choices of fragmentation paths, (i) spherical path (ii) static deformed fragmentation path, in which the deformations are independent of temperature and (iii) dynamic deformations hav-

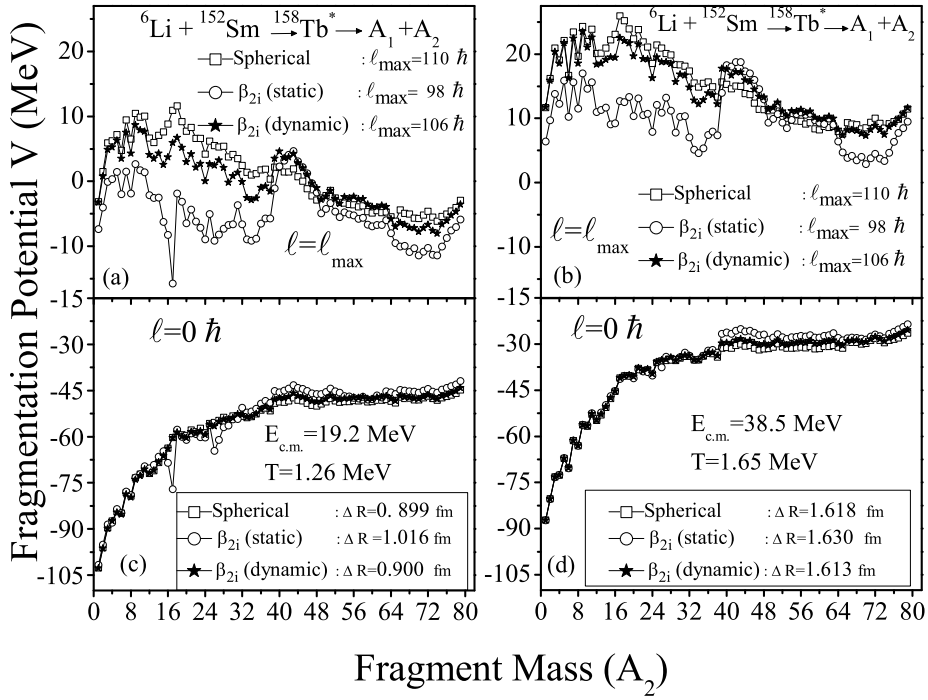

Figure 4.2 Fragmentation potential as a function of light fragment mass no. (A_2), for the decay of ^{158}Tb* nucleus formed in ^{6}Li+^{152}Sm reaction at (a,c) $E_{c.m.}$=19.2 MeV and (b,d) $E_{c.m.}$=38.5 MeV using spherical and deformed choices of fragmentation (β_2, $\theta_i^{opt.}$).

ing effect of temperature included in it. The scattering potential in Fig.4.1, plotted at $E_{c.m.}$=19.2 MeV (and T=1.26 MeV) for extreme angular momentum values, ℓ=0$\hbar$ and ℓ=ℓ_{max} shows the effect of deformation on the barrier position and barrier height. In the figure, solid lines represent spherical fragmentation, dotted lines are for static $\beta_{2i}(0)$ deformations and the dashed lines denote dynamical $\beta_{2i}(T)$ deformations. It is observed that with inclusion of static $\beta_{2i}(0)$ and dynamic $\beta_{2i}(T)$ quadrupole deformations both the barrier position as well as height get modified and hence the fusion probability gets influenced.

Fig. 4.2 shows the fragmentation potential V(A_2) minimized in mass co-ordinate η_A, for ^{6}Li+^{152}Sm→^{158}Tb* reaction at two extreme energies across the barrier i.e. at $E_{c.m.}$=19.2 MeV (T=1.26 MeV) and $E_{c.m.}$=38.5 MeV (T=1.65 MeV). In order to study the role of deformations, the fragmentation potential is plotted for spherical, static $\beta_{2i}(0)$

deformed and dynamic $\beta_{2i}(T)$ deformed choice of fragmentation. The interesting points observed from this figure are :(i) the characteristic behavior of the fragmentation potential is different at the lower versus higher ℓ-values. The behavior at maximum angular momentum value i.e. ℓ=ℓ_{max} is illustrated in Figs. 4.2(a,b) whereas Figs. 4.2(c,d) show the behavior at ℓ=0$\hbar$. It is observed that deformations play a significant role at ℓ=ℓ_{max} but, are silent at ℓ=0$\hbar$. (ii) at ℓ=ℓ_{max}, the structure of fragmentation potential is almost similar for spherical and dynamic deformation but is different for static deformation. At relative grounds the fragmentation potential is minimum and alpha structure is more prevalent for the static deformed choice of fragmentation.(iii) except for the change in magnitude of fragmentation potential, no noticeable change in the structure of V (A_2) is observed while going from lower to higher energy, for spherical and dynamical deformed fragmentation at ℓ=0$\hbar$ and ℓ=ℓ_{max}. However, with the inclusion of static deformation, small change in structure of fragments with mass A_2=14-30 is observed at higher angular momentum. Thus, it may be concluded that the fragmentation path is almost, independent of the variation in energy. Using the DCM approach, the cross-section for ER ($A_2 \leq 4$) are attained within one parameter fitting i.e. neck-length parameter $\triangle$R. This means that for different values of $\triangle$R, the reported ER cross-sections are attained for all the three choices of fragmentation. The values of ΔR for spherical and dynamic $\beta_{2i}(T)$ deformed cases are comparable to each other, being 0.899 fm and 0.9 fm at $E_{c.m.}$=19.2 MeV and 1.618 fm and 1.613 fm at $E_{c.m.}$=38.5 MeV respectively. Whereas, it is relatively higher in magnitude for static $\beta_{2i}(0)$ deformation approach being 1.016 fm at $E_{c.m.}$=19.2 MeV and 1.630 at $E_{c.m.}$=38.5 MeV.

The effect of deformed configuration is also evident from Fig.4.3 which shows variation of preformation probability P_0 as a function of fragment mass A_i. The figure clearly supports the fact that role of deformations comes into picture at higher angular momentum

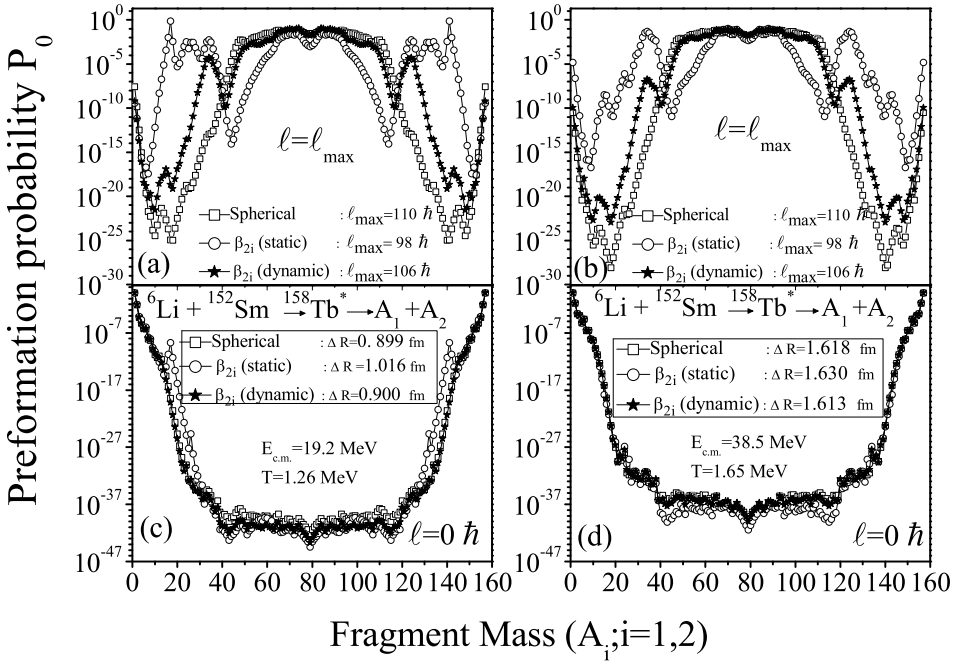

Figure 4.3 Preformation probability P_0 as a function of fragment mass, for the decay of compound system ^{158}Tb*, plotted for $\ell = 0\hbar$ and $\ell = \ell_{max}$ values, for spherical and deformed nuclei at lowest energy (parts a,c) and highest energies (parts b,d).

while it remains silent at ℓ=0$\hbar$. On a broader view, it is observed that fission fragment mass distribution is symmetric for all three choices of fragmentation for both the energies at ℓ=ℓ_{max}. However, a specific look of Figs. 4.3(a,b) shows that the mass distribution of spherical and $\beta_{2i}(T)$ is similar but that of $\beta_{2i}(0)$ is quite different. Also, the emergence of IMFs and HMFs (lying within mass range A_2=14-30) is observed for either of chosen energies across the barrier for $\beta_{2i}(0)$ choice of fragmentation. This emergence of IMFs and HMFs along with observed symmetric fragmentation indicates a possibility of fine structure effects in the decay of ^{158}Tb* nucleus. Concludingly, the inclusion of deformations and orientations effect of the decaying fragments changes the relative preformation probability P_0 quite significantly, and equivalently, the potential energy surfaces (PES).

Interestingly, in the experiment [12], at higher energies the contribution of charged particle is also indicated but not identified. The DCM based calculations identify the

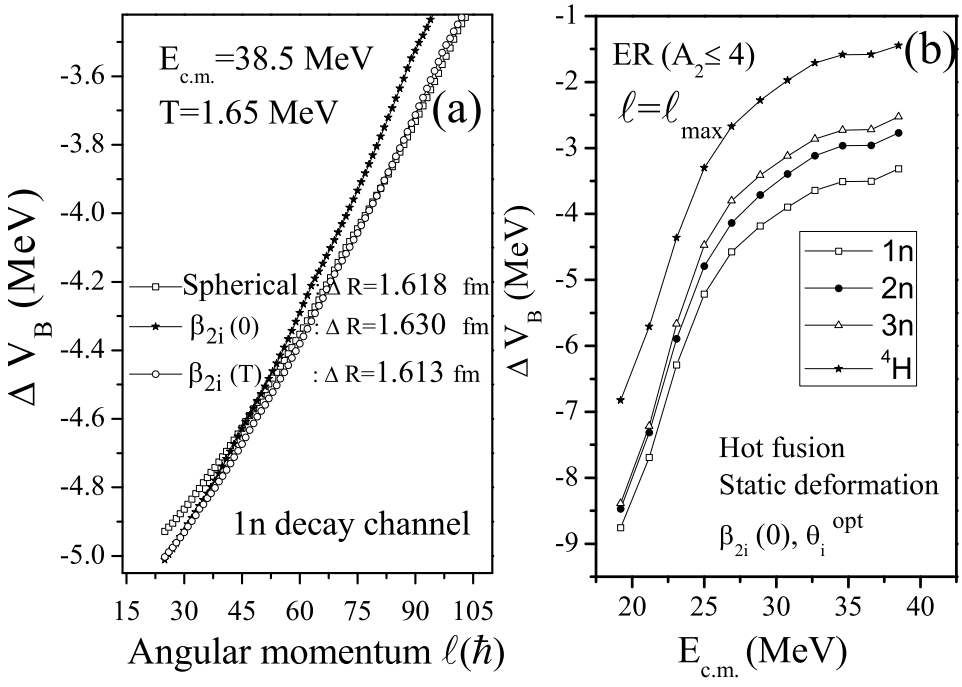

Figure 4.4 The barrier lowering parameter $\triangle V_B$ (a) as a function of angular momentum at $E_{c.m.}$=38.5 MeV. (b) as a function of center-of-mass energy $E_{c.m.}$, at ℓ=ℓ_{max}.

charged particle involved in the decay of ^{158}Tb* nucleus. The calculations suggest that ^4H charged particle, contributes about ∼1% towards the ER cross-section of ^{158}Tb* nucleus. It is relevant to mention here that in context of DCM calculations 1n channel contributes the most towards ER cross-section followed by σ_{xn} (x=2,3,4,5) and ^{4}H decay. However, if one takes relatively higher values of neck-length parameter ΔR then the reported cross-section could be achieved without including 1n cross-section. These results are discussed later in discussion of Fig.4.5.

It may be noted further that the barrier modification is an inbuilt property of DCM, that enters through neck-length parameter △R. Fig.4.4(a) shows variation of the barrier lowering parameter $\triangle V_B$ as a function of angular momentum ℓ at $E_{c.m.}$=38.5 MeV for ^{6}Li+^{152}Sm→^{158}Tb* reaction. It is to be noted that $\triangle V_B$ is negative and non-zero for all three choices of fragmentation. It is observed to be least at higher angular momentum and

Table 4.1 The decay cross-sections for evaporation residues ERs, calculated using DCM for ^{158}Tb* nucleus formed in ^{6}Li+^{152}Sm reaction with inclusion of quadrupole static ($\beta_{2i}(0)$) deformation, at all $E_{c.m.}$ values and at ℓ_{max}=98$\hbar$., compared with the experimental data of [12].

S. No.	$E_{c.m.}$ (MeV)	T (MeV)	ΔR_{ER} (fm)	σ^{DCM} (mb)	σ^{Expt} (mb)
1	19.2	1.26	1.016	0.25	0.26 ± 0.05
2	20.2	1.29	1.061	1.03	1.07 ± 0.22
3	20.7	1.30	1.115	1.62	1.77 ± 0.34
4	21.2	1.31	1.116	3.61	3.57 ± 0.45
5	21.6	1.32	1.150	6.52	6.74 ± 0.65
6	22.1	1.33	1.176	9.57	9.64 ± 0.80
7	22.6	1.34	1.219	17.10	17.30 ± 1.5
8	23.1	1.35	1.249	25.80	25.80 ± 2.1
9	23.6	1.36	1.281	38.15	39.70 ± 3.2
10	24.1	1.37	1.307	52.09	53.70 ± 4.3
11	24.5	1.38	1.340	76.50	76.80 ± 6.1
12	25.0	1.39	1.360	96.50	97.00 ± 5.7
13	26.0	1.41	1.408	150.00	151.00± 7.0
14	26.9	1.43	1.435	198.00	198.00 ± 9.0
15	28.9	1.47	1.488	304.00	304.00± 10
16	30.8	1.51	1.531	417.00	418.00± 12
17	32.7	1.54	1.570	560.00	563.00 ± 15
18	34.6	1.58	1.594	634.00	637.00 ± 16
19	36.6	1.61	1.597	705.00	705.00 ± 19
20	38.5	1.65	1.630	792.00	797.00 ± 20

keeps on increasing with decrease in ℓ-value. Hence, it can be said that independent of the deformations involved, large barrier modification is needed for lower angular momentum states. After looking at the behavior of $\triangle V_B$ at highest energy, its variation as a function of $E_{c.m.}$ for ER channels is shown in Fig. 4.4(b). This figure shows that at lower energies large barrier modification is required and it decreases as one moves from 1n to ^{4}H channel.

Since, the decay path is relatively more influenced with the inclusion of static deformation, the ER cross-sections calculated using DCM for the decay of ^{158}Tb* nucleus, with quadrupole static $\beta_{2i}(0)$ deformed choice of fragmentation, compared with the exper-

imental data, are tabulated in Table 4.1. Calculations are made for different neck-length parameter ΔR, chosen to fit the respective experimental data. Corresponding to the fitted ER cross-sections, the ΔR values are also shown in Table 4.1. It may be noted that neck-length parameter ΔR is a measure of relative separation between two decaying fragments. It's magnitude is limited within 2 fm, so as to justify the use of proximity interaction in DCM based calculations. Interestingly, for majority of compound systems formed in different mass regions [7, 8], it is observed that ΔR generally increases as a function of incident energy for CF processes.

The DCM based calculations reproduce the experimental data for all three approaches, i.e. spherical, static deformed and dynamical deformed fragmentation path successfully in terms of single fitting parameter ΔR. From Table 4.1 it may be noted that the ER contribution at all energies could reproduce the experimentally measured complete fusion cross-sections, thus giving way to the fact that fission contribution is negligible at all energies, which is in line with the experimental observation. To confirm the same, we have also calculated the fission cross-section using DCM at ΔR = 0fm and 0.5fm. The reason for taking relatively smaller values of ΔR is that the time scale of emission of fission fragments is large in comparison to that of ERs, as depicted in Fig. 3.1 for case of Fr nuclei studied in chapter 3. In framework of DCM the neck-length parameter gives a measure of time scale at which the reaction takes place, with small ΔR indicating large time scale. With this feature, the fission cross-sections were calculated for the most probable fission fragments at ΔR =0 fm and 0.5 fm and were found to be negligibly small in agreement with the experimental observation.

Experimentally, the ER (complete fusion) cross-sections have contributions from the neutron cross-sections, $\sum$xn ;x=2-5 producing residual nuclei $^{153-156}$Tb in the decay of ^{158}Tb*. After having a clear picture about ER decay channel and the effect of deforma-

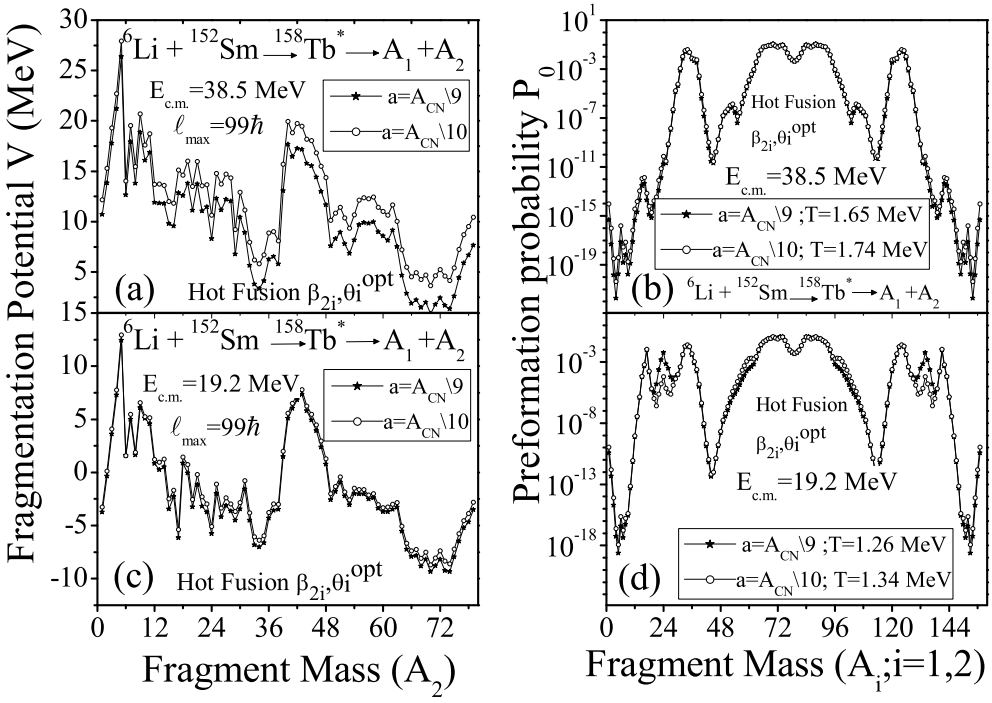

Figure 4.5 Effect of level density parameter on (a,c) fragmentation potential and (b,d) preformation probability for the neutron decay channel at both the extreme energies.

tions in it, it is of further interest to see the behavior of the potential energy surfaces corresponding to neutron cross-sections. Initially, using the level density parameter a= $A_{CN}/9$ the neutron cross-sections $\sum$xn ;x=2-5, were easily attained at below barrier energy (i.e. $E_{c.m.}$=19.2 MeV) but at the highest, above barrier energy (i.e $E_{c.m.}$ =38.5 MeV) the same could not be achieved even at maximum allowed value of neck-length parameter ΔR. Henceforth, the calculations were done with higher level density parameter a=$A_{CN}/10$ through which the cross-sections could be attained successfully at both extreme energies across the barrier.

Fig. 4.5 shows the effect of level density parameter on the fragmentation potential (part a,c) and preformation probability (part b,d) for the neutron decay channel at two extreme values of incident energies. The variation is shown only at ℓ=ℓ_{max}. With increase in level density 'a' the temperature increases and neck-length parameter for the fitted

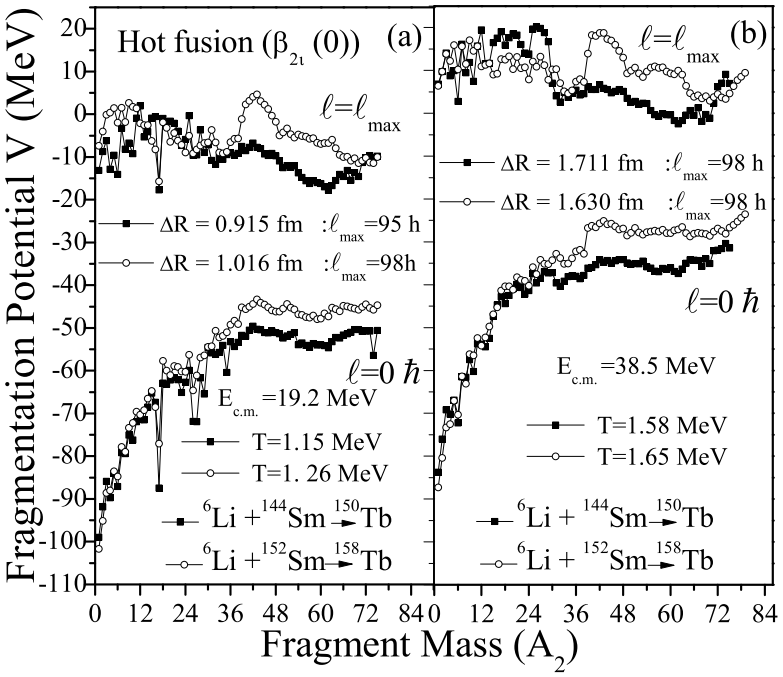

Figure 4.6 Fragmentation potential as a function of light fragment mass,A_2 for ^{150}Tb* and ^{158}Tb* channel at (a) $E_{c.m.}$=19.2 MeV and (b) $E_{c.m.}$=38.5 MeV.

neutron cross-sections decreases (from 1.172m to 1.164 fm at $E_{c.m.}$=19.2 MeV) whereas the ℓ_{max} value remains almost the same (ℓ=99$\hbar$). It is noticed that with the change in level density there is no significant change in the structure of potential energy surfaces (PES), except for an increase in magnitude of fragmentation potential observed only at highest energy. Interestingly, inspite of different contributing fragments, the mass distribution for the neutron decay channel is similar to that of evaporation residue channel (compare Fig. 4.3(a,b) with Fig 4.5(b,d)). It may be noted that neutron decay ($\sum$xn ;x=2-5) cross-section data could be addressed at relatively larger value of neck-length parameter ΔR, in the range of 1.16 fm-2.22fm, instead of 1.01fm-1.63fm for ER channel.

To explore the role of deformed shape of target nucleus and associated shell closure effects of decaying fragments, the ^{6}Li+^{144}Sm and ^{6}Li+^{152}Sm reactions are investigated at two extreme energies, across the Coulomb barrier. The experimental data for the decay of ^{150}Tb* formed in ^{6}Li+^{144}Sm reaction is taken from [13] and the ER (complete fusion)

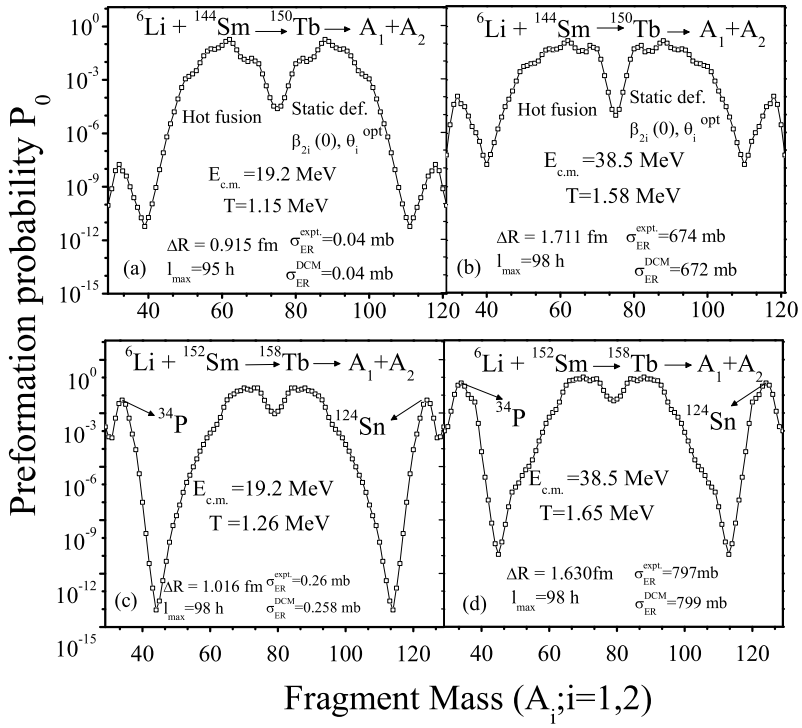

Figure 4.7 Preformation probability as a function of fragment mass,A_i for ^{150}Tb* (parts (a),(b)) and ^{158}Tb* (parts (c),(d)) channel at $E_{c.m.}$=19.2 MeV and $E_{c.m.}$=38.5 MeV for quadrupole static ($\beta_{2i}(0)$) deformation.

cross-section for the same are fitted using DCM. The calculations have been done for quadrupole static deformation $\beta_{2i}(0)$ within optimum orientation approach. The isotopic effect observed due to the addition of '8' neutrons in ^{144}Sm target can be better analyzed from Fig.4.6, where the fragmentation potential V(MeV) is plotted as a function of light fragment mass A_2. The interesting feature obtained from this figure is that there is no noticeable change in the behavior of fragmentation path in going from ^{150}Tb* and ^{158}Tb* system at ℓ=0$\hbar$ but it changes significantly at ℓ=ℓ_{max}. For the lighter system ^{150}Tb*, the fission distribution seems more asymmetric as compared to that for ^{158}Tb* nucleus. Also, the magnitude of fragmentation potential of ^{158}Tb* nucleus is relatively higher for majority of decaying fragments at both energies. A considerable change in PES is observed in going from minimum to maximum energy, which is clarified further in Fig.4.7,

showing the variation of preformation probability P_0 as a function of fragment mass A_i for ^{6}Li+^{144}Sm→^{150}Tb* and ^{6}Li +^{152}Sm→^{158}Tb* reactions at $E_{c.m.}$=19.2 MeV and $E_{c.m.}$=38.5 MeV. It is clear from this figure that the fission pattern remains the same i.e. asymmetric for both the isotopes. However, for ^{150}Tb* isotope mass distribution is relatively more asymmetric than that for ^{158}Tb* nucleus. Moreover, heavier isotope favors HMF (heavy mass fragment) contribution to a greater extent as compared to the lighter one. Thus a significant change in the HMF region is observed with the increase in the iso-spin, N/Z ratio of the decaying Tb compound systems.

In accordance with the observations of Fr nuclei studied in chapter 3, it is observed that shell effects (magic shells) also play an important role in the fragment mass distribution of ^{158}Tb* nucleus formed in ^{6}Li+^{152}Sm reaction at both the extreme energies giving rise to high preformation probability for ^{34}P (Z=15, N=19) fragment and its complement ^{124}Sn(Z=50, N=74) (see fig. 4.7(c,d)). It must be noted that this shoulder signifies importance of shell effects as ^{34}P seem to be originated due proton shell closure Z=16 and neutron shell closure N=20. Similarly, ^{124}Sn corresponds to magic proton shell closure Z=50. On the other hand, no such highly preformed peak is observed for the lighter mass, ^{150}Tb* nucleus (see fig. 4.7(a,b)). This difference in preformation probability shows that shell closure effects of decaying fragments are more prominent for deformed targets like ^{152}Sm, and are nearly absent in spherical target ^{144}Sm. It is relevant to mention here that in earlier work [8,16] similar effects were seen in the decay of ^{202}Pb formed via ^{152}Sm target and the appearance of such asymmetric peak was associated with possibility of quasi-fission. This asymmetric peak at A_2=34 (and complementary fragment A_1=124) seem to suggest that some other competing decay mechanism is in operation for ^{6}Li +^{152}Sm→^{158}Tb* reaction and is further supported by $\sim$ 28% suppression of measured fusion cross-sections in ^{158}Tb* nucleus [12].

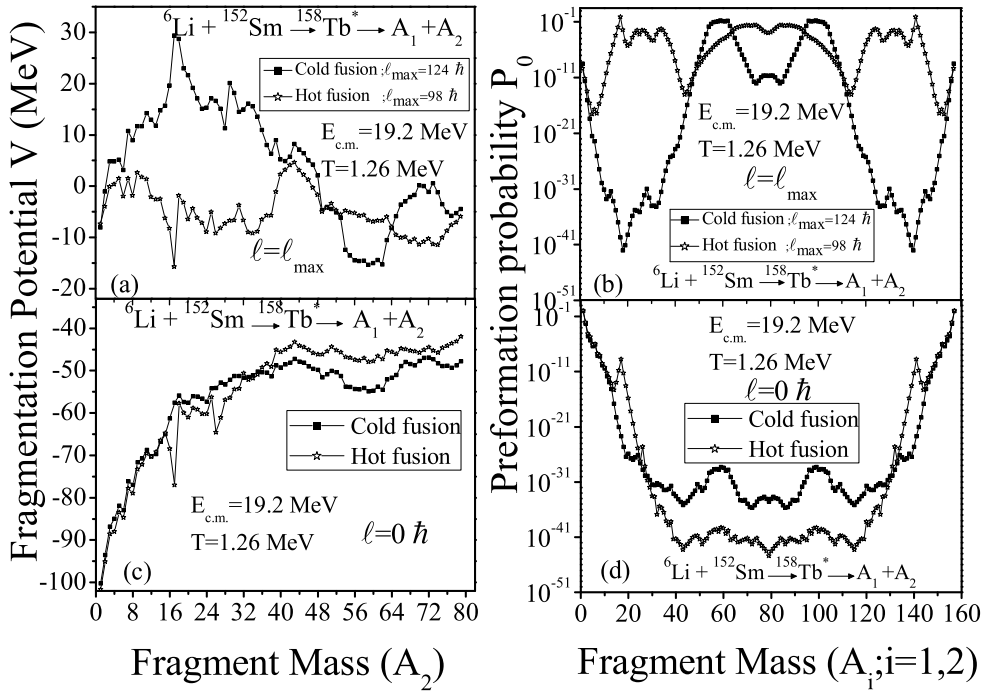

Figure 4.8 Parts(a),(c) show fragmentation potential as a function of light fragment mass no.(A_2), Parts (b),(d) show the variation of preformation probability P_0 as a function of fragment mass (A_i) for decay of ^{158}Tb* nucleus formed in ^{6}Li+^{152}Sm reaction at $E_{c.m.}$=19.2 MeV for cold polar and hot equatorial configuration.

Evidently, apart form the role of deformations, the orientation degree of freedom holds equal importance as far as heavy ion reaction dynamics is concerned. Thus, after having an insight of static and dynamic deformations and the shell closure effects, the role of orientation degrees of freedom in the decay of intermediate mass ^{158}Tb* nucleus formed in ^{6}Li+^{152}Sm reaction is invstigated. As discussed in chapter 3, for actinide targets being prolate deformed there lies a possibility that the projectile may hit the 'equatorial' region of the deformed target and hence possess the most 'compact' configuration. Interestingly, this orientation may depend on the energy of the colliding nuclei, so with the change in energy from above barrier to below barrier, change in orientation may also be observed. At below barrier energy, the probability of the projectile to hit the deformed target in 'polar' region is feasible, giving rise to 'elongated' configuration [1,17]. Since for

^{6}Li+^{152}Sm→^{158}Tb* reaction, ^{152}Sm is a prolate deformed target, so it would be of interest to see the effect of orientation at below barrier energy for this lanthanide system. In order to pursue with this, comparative analysis of equatorial and polar configurations in the decay of ^{158}Tb* nucleus has been done. The comparison of hot (equatorial) compact and cold (polar) elongated orientation is carried out by considering quadrupole static $\beta_{2i}(0)$ deformation and optimum orientation approach into account. The equatorial compact orientations have smallest interaction radius and highest barrier height, while the polar elongated orientations have largest interaction radius and lowest barrier height [1]. Fig. 4.8 (a,c) shows the variation of fragmentation potential as a function of light fragment mass (A_2) at $E_{c.m.}$=19.2 MeV for both hot (equatorial) compact and cold (polar) elongated orientations. From the figure it is clear that the effect of orientation is more pronounced at higher angular momentum, ℓ=ℓ_{max} as compared to ℓ=0$\hbar$. Interestingly, hot equatorial orientations favor symmetric fragment mass distribution whereas, for the cold polar orientations an asymmetric fragmentation is preferred. This is also supported by Fig. 4.8 (b,d) which shows preformation probability as a function of fragment mass (A_i). One may clearly see from this figure that the orientations are sensitive to the angular momentum effect. At minimum ℓ-value, i.e., ℓ=0$\hbar$ no much change is seen in preformation probability profile and hence the fragment distribution (see Fig. 4.8(c,d)). On the contrary, strong variation in mass distribution from symmetric to asymmetric fragmentation is observed in going from equatorial to polar orientations at maximum angular momentum, ℓ=ℓ_{max} (see Fig. 4.8(a,b)). These results are consistent with those observed for superheavy region, as discussed in chapter 3. The symmetric mass distribution observed at ℓ_{max} for equatorial orientation favors the IMFs and HMFs in its decay, which are highly suppressed for polar choice of orientation. The neck-length parameter ΔR and the ℓ_{max} value are different for both the cases, being higher for polar orientation (1.070 fm & 124$\hbar$) as compared

Table 4.2 The ICF decay cross-sections for 2n emission channel, calculated using DCM with static quadrupole ($\beta_{2i}(0)$) deformation for ^{154}Eu* nucleus formed in ^{2}H+^{152}Sm reaction at all corrected $E_{c.m.}$ values lying above the Coulomb barrier compared with experimental incomplete fusion (ICF) data [12]. Also, the ΔR values corresponding to the fitted cross-sections for ^{2}H channel are tabulated.

S. No.	$E_{c.m.}$ (MeV)	T (MeV)	ΔR_{2n} (fm)	σ_{ICF}^{DCM} (mb)	$\sigma_{ICF}^{EXPT.}$ (mb)
1	8.060	1.051	1.405	14.94	14.980
2	8.225	1.056	1.439	18.74	19.250
3	8.389	1.061	1.440	20.50	20.760
4	8.547	1.065	1.455	23.20	23.230
5	8.883	1.075	1.472	28.41	28.510
6	9.208	1.084	1.475	28.90	29.018
7	9.870	1.102	1.495	30.60	31.350
8	10.521	1.119	1.483	29.20	29.375
9	11.182	1.137	1.460	24.00	24.803
10	11.844	1.154	1.430	18.00	18.121
11	12.495	1.171	1.420	16.13	16.298
12	13.156	1.188	1.404	13.72	13.762

to that for equatorial orientation (1.016 fm & 98$\hbar$). From the above discussion, it may be concluded that the orientation of decaying fragments and the associated shell closure effects play an important role in the decay of intermediate mass ^{158}Tb* nucleus.

The experiment carried out to study the decay cross-sections formed in ^{6}Li+^{152}Sm$\rightarrow^{158}$Tb* reaction [12] shows that CF cross-sections are suppressed by $\sim$28%. This suppression is associated with the break-up of loosely bound projectile ^{6}Li into 2 fragments, ^{2}H and ^{4}He. Based on this result, the cross-sections of composite system formed through incomplete fusion ICF of ^{6}Li are studied by considering ^{2}H channel only. In framework of DCM the calculations for ICF are done by applying relevant and necessary energy corrections as discussed in chapter 2. The calculations are done by taking the quadrupole static ($\beta_{2i}(0)$) deformations into account. Experimentally the dominant decay mode for d-capture is the 2n emission process and cross-sections for the same have

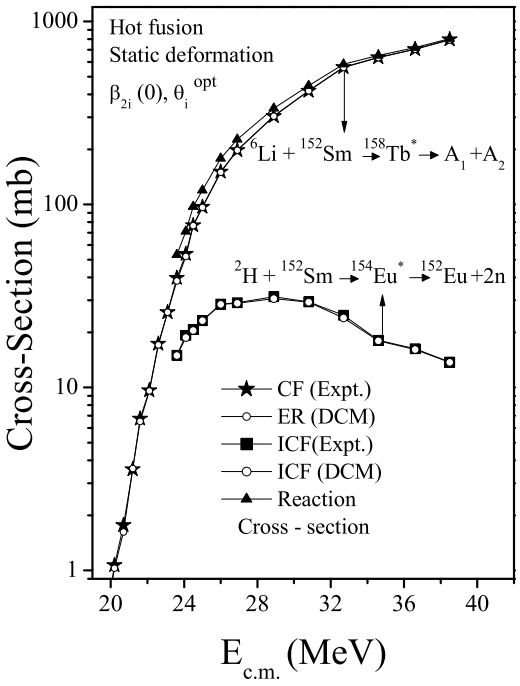

Figure 4.9 Comparison of DCM cross-sections having contribution from complete fusion and incomplete-fusion processes with experimental data at different center-of-mass energies.

been calculated. The fitted cross-sections at various corrected energies for ^2H channel with the corresponding $\triangle R$ values are tabulated in Table 4.2.

A comparative study of calculated ER cross-sections with experimental data is shown in Fig.4.9. It may be noted that evaporation residue channel is the major contributor towards complete fusion cross-sections with fission contribution being negligibly small at reported energy range. Also the behavior of incomplete fusion is depicted in this figure, which shows that ICF contributes significantly towards the total reaction cross-section. Fig.4.9 clearly shows that the DCM based ER cross-sections are in nice agreement with the experimental data.

4.3 Summary

In this chapter, the deformations and orientations are observed to have significant effect on decay of intermediate mass $^{158}Tb^*$ system. The role of static and dynamic deformations is studied within framework of DCM for ^{6}Li+^{152}Sm$\rightarrow^{158}$Tb* reaction over a wide range of incident energies spread on either side of Coulomb barrier. The complete fusion cross-sections having major contribution from the ER channel are reasonably accounted at various incident energies within a single parameter ($\triangle$R) description. The fragment mass distribution varies with the inclusion of deformations. This may be due to the preformation factor P_0, which gets modified with the inclusion of deformations and hence changes the fragment mass distribution. The deformations play a silent role at ℓ=0$\hbar$, whereas they become indispensable at ℓ=ℓ_{max}. The neck-length parameter $\triangle$R is almost similar for spherical and dynamic $\beta_{2i}(T)$ deformed choice of fragmentation whereas, it is higher in magnitude for static deformed consideration. In addition to this, the effect of hot (equatorial) compact and cold (polar) elongated orientation is explored in the decay of $^{158}Tb^*$ nucleus. For equatorial orientation, IMF and HMF components seem more prominent which are otherwise suppressed for polar orientation. Moreover, the fragment mass distribution changes from symmetric to asymmetric distribution while going from equatorial to polar orientations. This result is consistent with the observation of superheavy region studied in chapter 3. With the change in level density parameter, no significant change in potential energy surfaces (PES) is observed for the $\sum$xn ;x=2-5 cross-sections. Interestingly the fragmentation structure of $\sum$xn ;x=2-5 decay channel is similar to that of ER, despite of the fact that the contributing fragments are not the same in both of them. The N/Z dependence of decay fragments in Tb isotopes is explored and it is observed that neutron-rich ^{158}Tb* nucleus formed with deformed target ^{152}Sm target exhibits enhanced cross-sections for ^{34}P (Z=15, N=19) and its complementary fragment ^{124}Sn(Z=50, N=74)

which are otherwise suppressed for $^{150}Tb^{*}$ nucleus formed via spherical target ^{150}Sm. This observation concludes that the shell closure effect in decaying fragments are more prominent for reactions with deformed target as compared to spherical targets and gives way to some competing decay process. Also, the contribution of cross-sections obtained through ICF process is worked out in framework of DCM.

So far in chapters 3 and 4 the ER and fission decay channels were addressed where various aspects related to CN dynamics of heavy and intermediate mass nuclei have been addressed. Apart from studying the compound nucleus picture and its subsequent governance in the possible decay channels, the dynamics associated with loosely bound nucleus exhibiting the incomplete fusion process is also discussed briefly in chapter 4. The collective clusterization description is further applied to address the incomplete fusion process observed for relatively heavy and light mass nuclei and the results for the same are discussed in chapter 5.

Bibliography

[1] R. K. Gupta, M. Balasubramaniam, R. Kumar, N. Singh, M. Manhas, and W. Greiner, J. Phys. G : Nucl. Part. Phys. **31**, 631 (2005).

[2] R. K. Gupta, M. Manhas, and W. Greiner, Phys. Rev. C **73**, 054307 (2006).

[3] R. K. Gupta, M. Balasubramaniam, R. Kumar, D. Singh, and C. Beck, Nucl. Phys. A **738**, 479c (2004).

[4] R K Gupta, W. Scheid, and W Greiner, Phys. Rev. Letts. **35**, 353 (1975)

[5] K. Sandhu, G. Kaur, and M. K. Sharma, Nucl. Phys. A **921**, 114 (2014).

[6] G. Kaur, D. Jain, R. Kumar, and M. K. Sharma, Nucl. Phys. A **916**, 260 (2013)

[7] B. B. Singh, M. K. Sharma, R. K. Gupta, and W. Greiner, Int. J. Mod. Phys E **15**, 699 (2006)

[8] S. Kanwar, M. K. Sharma, B. B. Singh, R. K. Gupta, and W. Greiner, Int. J. Mod. Phys E **18**, 1453 (2009).

[9] P. Moller, J. R. Nix,W. D. Myers, and W. J. Swiatecki, At. Nucl. Data Tables **59**, 185 (1995).

[10] M. Muenchow and W. Scheid, Phys. Lett. B **162**, 265 (1985); Nucl. Phys. A **468**, 59 (1987).

[11] M. Rashdan, A. Faessler, and W. Wadia, J. Phys. G: Nucl. Part. Phys. **17**, 1401 (1991).

[12] P. K. Rath, S. Santra, N. L. Singh, K. Mahata, R. Palit, B. K. Nayak, K. Ramachandran, V. V. Parkar, R. Tripathi, S. K. Pandit, S. Appannababu, N. N. Deshmukh, R. K. Choudhry, and S. Kailas, Nucl. Phys. A **874**, 14 (2012).

[13] P. K. Rath, S. Santra, N. L. Singh, R. Tripathi, V. V. Parkar, B. K. Nayak, K. Mahata, R. Palit, S. Kumar, S. Mukherjee, S. Appannababu, and R. K. Choudhry, Phys. Rev. C **79**, 051601(R) (2009).

[14] G. Kaur and M. K. Sharma, Phys. Rev. C **87**, 044601 (2013)

[15] M. G. Itkis, J. Äystö, S. Beghini, A. A. Bogachev, L. Corradi, O. Dorvaux, A. Gadea, G. Giardina, F. Hanappe, I. M. Itkis, M. Jandel, J. Kliman, S. V. Khlebnikov, G. N. Kniajeva, N. A. Kondrateiv, E. M. Kozulin, L. Krupa, A. Latina, T. Mataerna, G. Montagnoli, Yu. Ts. Oganessian, I. V. Pokrovsky, E. V. Prokhorova, N. Rowley, V. A. Rubchenya, A. ya. Rusanov, R. N. Sagaidak, F. Scarlassara, A.M. Stefanini, L. Stuttge, S. Szilner, M. Trotta, W. H. Trzaska, D. N. Vakhtin, A. M. Vinodkumar, and V. I. Zagrebaev, Nucl. Phys. A **734**, 136 (2004).

[16] A.M. Stefanini, M. Trotta, B. R. Behera, L. Corradi, E. Fioretto, A. Gadea, A. Latina, S. Szilner, Y. W. Wu, S. Beghini, G. Montagnoli, F. Scarlassara, A. Yu. Chizhov, I. M. Itkis, N. A. Kondratiev, I. V. Pokravskiy, R. N. Sagaidak, G. N. Kniajeva, E. M. Kozulin, V. M. Voskressensky, S. Courtin, F. Hass, and N. Rowley, Eur. Phys. J. A **23**, 473 (2005).

[17] K. Nishio, H.Ikezoe, S. Mitsuoka, I. Nishinaka, Y. Nagame, Y. Watanabe, T. Ohtsuki, K. Hirose, and S. Hofmann, Phys. Rev. C **77**, 064607 (2008).

Chapter 5

Decay analysis of nuclei formed through complete fusion and incomplete fusion processes

In previous chapters, the reaction dynamics associated with compound nucleus (CN) formed after compete fusion (CF) of projectile with target nucleus was explored by studying the role of deformations, orientation degree of freedom, shell closure, iso-spin (N/Z ratio) etc. An extensive analysis of such effects was carried out by studying the decay profile of heavy and intermediate mass systems formed in heavy ion collisions. In addition to this, a brief discussion on incomplete fusion process was also carried out in context of ^{6}Li+^{152}Sm reaction, explaining the dynamics of intermediate mass $^{158}Tb^{*}$ system. Widening this horizon, the present chapter explores the dynamics of reactions exhibiting incomplete fusion (ICF) process in reference to heavy and relatively lighter intermediate mass nuclei. To pursue with it, the evaporation residue (ER) decay cross-sections obtained through complete fusion of ^{20}Ne projectile and incomplete fusion observed due to break-up of ^{20}Ne is studied using DCM in reference to experimental observations of [1].

Also, the ER cross-sections observed through complete and incomplete fusion of ^{6}Li with ^{90}Zr target are explored in reference to [2]. The results obtained using DCM for these reactions are published in [3,4]. This chapter provides a brief description of ICF mechanism in Sec.5.1. Further, Sec.5.2.1 and Sec.5.2.2 presents the study of dynamics associated with CF and ICF processes observed in ^{20}Ne and ^{6}Li induced reactions respectively. Finally the results are summarized in Sec.5.3.

5.1 Introduction

For reactions involving projectile with low break-up threshold, the processes other than the complete fusion become important, because of which the fusion cross sections are found to drop below the total reaction cross sections. This suppression is associated with phenomenon of splitting of projectile before interaction with target nucleus and is coined as incomplete fusion (ICF) process. For reactions exhibiting ICF, the fractional mass, charge as well as the linear momentum of projectile is transferred to the target nucleus, due to the prompt emission of α and/or α-like clusters in forward direction with almost projectile velocity. Wilczynski et. al. [5] has established ICF as an extension of CF for higher angular momentum values. This is because, in CF process, for the compound nucleus formed after amalgamation of entire projectile with the target nucleus the angular momentum and the kinetic energy is distributed amongst all degrees of freedom. However, with non-central interactions [6–8], higher angular momentum values are imparted and as a consequence of this entire fusion of the projectile is hindered giving way to ICF. This suggests that, the CF and ICF reaction modes can be disentangled on the basis of driving angular momenta at different interaction trajectories. The lower angular momentum states are shown to contribute towards CF, whereas at relatively higher ℓ values

the centrifugal potential controls the attractive nuclear potential, and consequently the pocket in the entrance channel potential starts disappearing [9–11], giving rise to ICF contribution.

The ICF concept was coined with the experimental observation by Britt and Quinton [12]. Since then, it has been actively investigated using heavy-ion beam facilities and various macroscopic models [13–16] and received a fillip [17] with the advent of loosely bound nuclei [18]. However in certain exceptional cases, ICF process has also been noticed for reactions involving tightly bound nuclei [19] and has an impact on the complete fusion cross-sections.

Just like CF process, the ICF process also contributes to provide worthy information regarding nuclear dynamics and hence it becomes mandatory to investigate its behavior for overall understanding of nuclear reaction. In view of this, the present chapter comprises of the application of DCM [20–27] to study the ER decay cross-sections obtained through CF and ICF processes in reference to heavy and relatively lighter intermediate mass nuclear systems.

5.2 Calculations

5.2.1 Analysis of CF and ICF processes in ^{20}Ne induced reaction

In a nuclear reaction, the availability of evaporation residues and fission fragments impart a comprehensive picture of processes subsequent to collision between projectile and target nuclei. In view of this, the ER cross-sections obtained through CF and ICF processes are studied using DCM in reference to an experiment carried by Tripathi et. al., [1] for ^{201}Bi* system formed in ^{20}Ne+^{181}Ta reaction at E_{lab}=150 MeV and 180 MeV. In addition to this a significant contribution of ICF, is also analyzed by incorporating some relevant energy

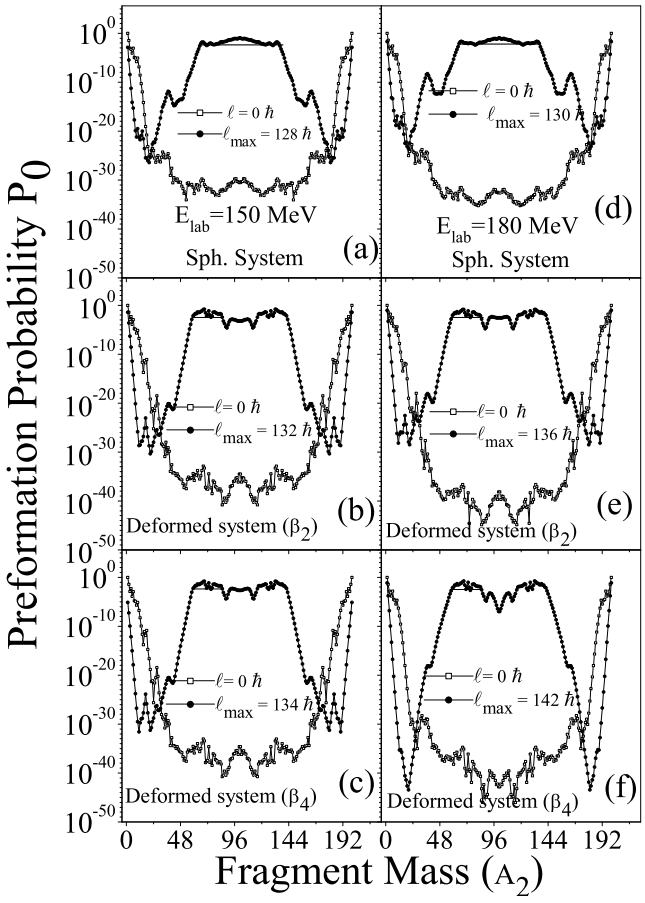

Figure 5.1 Preformation Probability P_0 as a function of Fragment Mass A_2 for spherical, β_2 deformed and β_2-β_4 deformed consideration at (a) E_{lab}=150 MeV and (b) E_{lab}=180 MeV .

corrections in framework of DCM.

As an extension to previous study of deformation effects, the role of higher multipole deformations is examined in this chapter in reference to ^{201}Bi* nucleus, by studying ERs for CN decay using (i) spherical choice of fragmentation (ii) with inclusion of quadrupole (β_2) deformations using optimum orientations [20] and (iii) deformation effects up to hexadecapole (i.e β_2+β_3+β_4) deformations using compact orientation approach [21].

Fig. 5.1 shows variation of preformation probability P_o plotted as a function of fragment mass (A_2) for spherical (upper panel), β_2 deformed (middle panel) and β_2-β_4 deformed (lower panel) fragmentation approach at E_{lab}=150 MeV and E_{lab}=180 MeV re-

Table 5.1 The DCM calculated ER cross-sections for the decay of ^{201}Bi* nucleus formed in ^{20}Ne+^{181}Ta reaction, compared with experimental results of [1]. Also tabulated are the neck-length parameter Δ R, ℓ_{max} values for spherical and deformed approach at both energies.

S.No.	Choice of Fragmentaion	ΔR_{ER} (fm)	ℓ_{max} ($\hbar$)	σ_{ER}^{DCM} (mb)	$\sigma_{ER}^{Expt.}$ (mb)
		E_{lab}=150MeV			
1	Spherical	1.595	128	15	15
2	β_2 Deformed	1.256	132	15	15
3	β_{2-4} Deformed	1.250	134	15	15
		E_{lab}=180MeV			
1	Spherical	1.785	130	92	92
2	β_2 Deformed	1.248	136	92	92
3	β_{2-4} Deformed	1.680	142	92	92

spectively. For both the energies, the deformations seem to influence the fragment mass distribution at extreme ℓ-values i.e. at ℓ=0$\hbar$ and ℓ=ℓ_{max}. From Fig. 5.1 (upper panel) it is observed that mass distribution is symmetric and fragments in the range A_2=65-100 contribute toward fission fragments. On the contrary with inclusion of deformation effects (for the middle and lower panels of Fig. 5.1) it becomes near-symmetric and the contributing fission fragments lie in range A_2=58-84. It is worth noting that, the fission distribution is almost identical for spherical and β_2 choice of deformation, whereas, the same becomes relatively asymmetric with inclusion of β_4 deformation at E_{lab}=180 MeV. Fig. 5.1, also suggests that the ER contribution dominates at ℓ=0$\hbar$ whereas fission products start competing with ER at higher ℓ values. The reported CN based ER cross-sections could be achieved with either of these three choices of fragmentation by using only parameter of DCM, the neck-length parameter ΔR. At E_{lab}=150 MeV the total experimental ER cross-section is 154 mb [1] whereas at higher energy its value is 580 mb. This reported ER is shown to have contribution from CF as well as ICF process. At

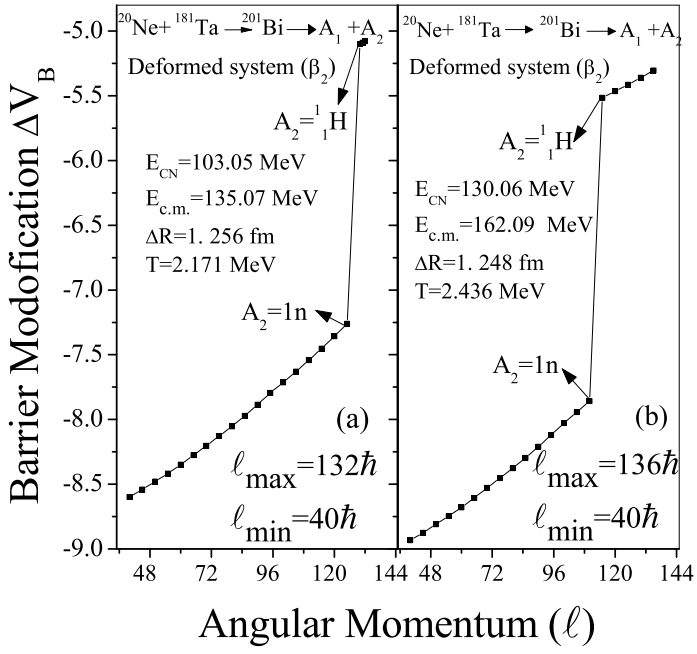

Figure 5.2 ΔV_B as a function angular momentum (ℓ) at (a) E_{lab}=150 MeV and (b) E_{lab}=180 MeV.

E_{lab}=150 MeV the ER formed via CF is reported to have contribution of 15 mb whereas the remaining 139 mb cross-section accounts for the ER due to ICF process. Similarly, the ER cross-section obtained due to CN at E_{lab}=180 MeV is 92 mb and the rest i.e. 488 mb stands for cross-section through ICF. For all the three cases i.e., spherical, β_2 deformed and β_2-β_4 deformed systems the ER cross-section at energies E_{lab}=150 and 180 MeV successfully attained using the DCM approach, compared with experimented data are tabulated in Table 5.1. Also shown are the neck-length parameter "ΔR" and ℓ_{max} values used in the calculations. It may be noted that, ΔR, assimilates the neck formation effects and this criteria is similar to the one adopted in scission and saddle point statistical fission models. The neck-length parameter ΔR, refers to the actually used barrier height and hence the concept of "barrier lowering" gets introduced in a natural way. In other words by introducing ΔR, the barrier penetration path i.e. $V(R_a, \ell)$ is modified as shown in Fig. 2.2 of chapter 2. With the positive value of ΔR, $V(R_a, \ell)$ increases and conse-

quently $\Delta V_B = V(R_a)$-V_B decreases. Thus, the DCM supports the possible explanation for hindrance phenomenon in terms of modified shape of potential inside the barrier at sub-barrier energies.

Fig. 5.2 represents the barrier modification,i.e. "barrier lowering" effects (see equation 2.57) as a function of angular momentum ℓ, for β_2 deformed choice of fragmentation at both the energies. One may clearly see that, barrier modification becomes more desirable at higher energy and lower angular momentum. Moreover, with the variation of ℓ-values, the contributing decaying fragments being emitted also vary from 1n to ^{1}H.

After studying ER cross-sections obtained through the CN decay of ^{201}Bi* nucleus formed in ^{20}Ne+^{181}Ta reaction at E_{lab}=150 MeV and E_{lab}=180 MeV, the validity of DCM is tested in reference to the experimentally measured ICF cross-sections at reported energies. The ICF process is observed when the projectile breaks up prior to the fusion state and a part of it goes straight without interacting with the target while the residual part fuses with the target. In present case, ^{20}Ne having low α-break-up threshold is supposed to break up before fusion as a result, some of the nucleons go un-deviated and uninteracted while the remaining one's fuse with the target. The four dominant channels accounting for the ICF process are:

Channel 1:-^{4}He+^{181}Ta$\rightarrow$^{185}Re$\rightarrow A_1+A_2$(^{4}He transfer)

Channel 2:-^{8}Be+^{181}Ta$\rightarrow$^{189}Ir$\rightarrow A_1+A_2$ (^{8}Be transfer)

Channel 3:- ^{14}N+^{181}Ta$\rightarrow$^{195}Hg$\rightarrow A_1+A_2$(^{14}N transfer)

Channel 4:- ^{16}O+^{181}Ta$\rightarrow$^{197}Tl$\rightarrow A_1+A_2$ (^{16}O transfer)

For all these four channels, the energy of interacting projectile needs to be modified. The energy of remnant projectiles which fuse with the target nucleus is obtained by subtracting the ejectile (i.e outgoing particle which does not fuse with target) energy from the energy of original projectile, as discussed in chapter 2.

Table 5.2 Evaporation Residues formed in ICF process for four dominant channels at E_{lab}=150 MeV and 180 MeV

	E_{lab}=150 MeV			E_{lab}=180 MeV		
Projectile	E_{lab} (MeV)	ℓ_{max} ($\hbar$)	σ_{ICF}^{DCM} (mb)	E_{lab} (MeV)	ℓ_{max} ($\hbar$)	σ_{ICF}^{DCM} (mb)
^{4}He	30	110	78.6	36	110	262.0
^{8}Be	60	117	36.8	72	120	138.0
^{14}N	105	116	9.8	126	121	45.0
^{16}O	120	129	12.8	144	129	40.8
			Σ_{DCM}=138.0			Σ_{DCM}=485.8
			$\Sigma_{Expt.}$=139.0			$\Sigma_{Expt.}$=488.0

The energy correction to four ICF channels i.e ^{4}He, ^{8}Be, ^{14}N and ^{16}O transfer reactions is applied and the energy of new projectiles in ICF process is calculated. The modified energies in reference to ICF process are tabulated in Table 5.2 with the corresponding ER cross-sections for each channel calculated at same value of neck-length parameter i.e. ΔR=1.460 fm at E_{lab}=150 MeV and ΔR=1.586 fm at E_{lab}=180 MeV. The sum of ER cross-section obtained for all the four channels at same value of the neck-length parameter ΔR=1.460 fm comes out to be 138.0 mb which is very close to the reported experimental value i.e. 139.0 mb at E_{lab}=150 MeV. Similarly at E_{lab}=180 MeV, the evaporation residue cross-section of 485.8 mb, summed up for all four channels is calculated at ΔR=1.586 fm and is in good agreement with reported cross-section of 488.0 mb. Interestingly, with β_2 deformed choice of fragmentation the neck-length parameter ΔR increases as a function of E_{lab} for ICF channel (ΔR=1.460 at E_{lab}=150 MeV and 1.586 at E_{lab}=180 MeV) contrary to CN process where ΔR is almost same at both incident energies. It may be noted that DCM based calculations can be used to account for ICF contribution of individual transfer channels. The individual contribution of all four channels is tabulated in Table

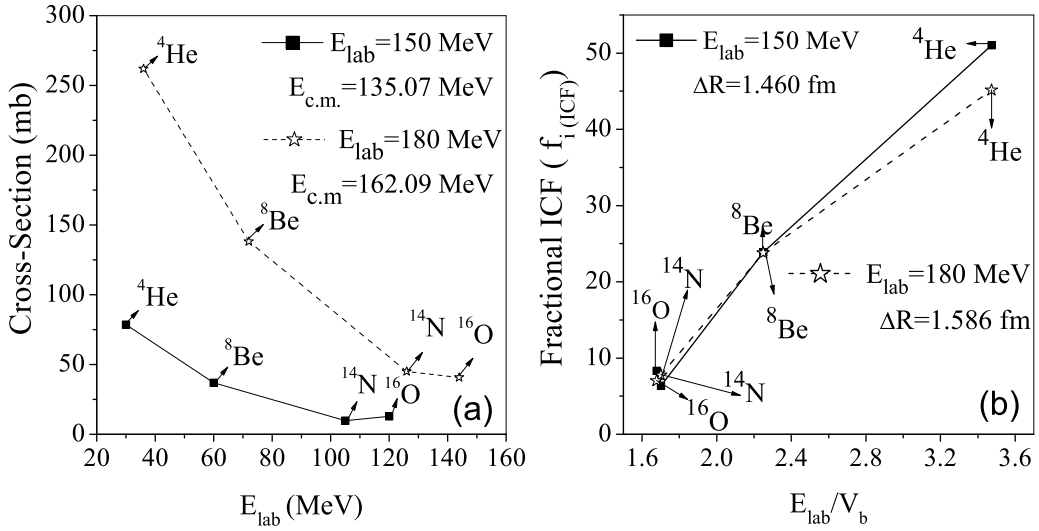

Figure 5.3 (a)Variation of DCM calculated ICF cross-sections formed in ^{4}He, ^{8}Be, ^{14}N, ^{16}O transfer channels as a function of corresponding E_{lab} values (b) Fractional ICF as a function of E_{lab}/V_b at E_{lab}=150 MeV and E_{lab}=180 MeV.

5.2 and illustrated in Fig.5.3(a). It is observed that ^{4}He transfer channel contributes maximum towards ICF process, followed by ^{8}Be transfer channel, ^{14}N transfer channel, ^{16}O transfer channels at E_{lab}=150 MeV and E_{lab}=180 MeV. This result is in agreement with that of Morgenstern *et al.,* [28, 29] which shows that ICF component contributes more towards the total reaction cross-sections for mass asymmetric systems as compared to mass symmetric systems. Also an extensive work has been carried out on CF and ICF processes by Morgenstern *et al.,* that provides a correlation between fraction of ICF and center-of-mass velocity with mass asymmetry in the entrance channel. In order to see this effect, f_{ICF} is plotted as a function of E_{beam}/V_b for each channel as shown in Fig.5.3(b). The f_{ICF} corresponds to ICF contribution of respective transfer channel and is given as

,

$$f_{ICF} = \frac{\sigma_{i(ICF)}}{\sigma_{TF}} \times 100 \tag{5.1}$$

where $\sigma_{i(ICF)}$ corresponds to cross-sections for each channel and σ_{TF} is total cross-section i.e. σ_{CF}+σ_{ICF}. Although ICF cross-sections are higher at higher incident energy (as seen in Fig.5.3(a)) but the fractional contribution of ICF components is almost independent

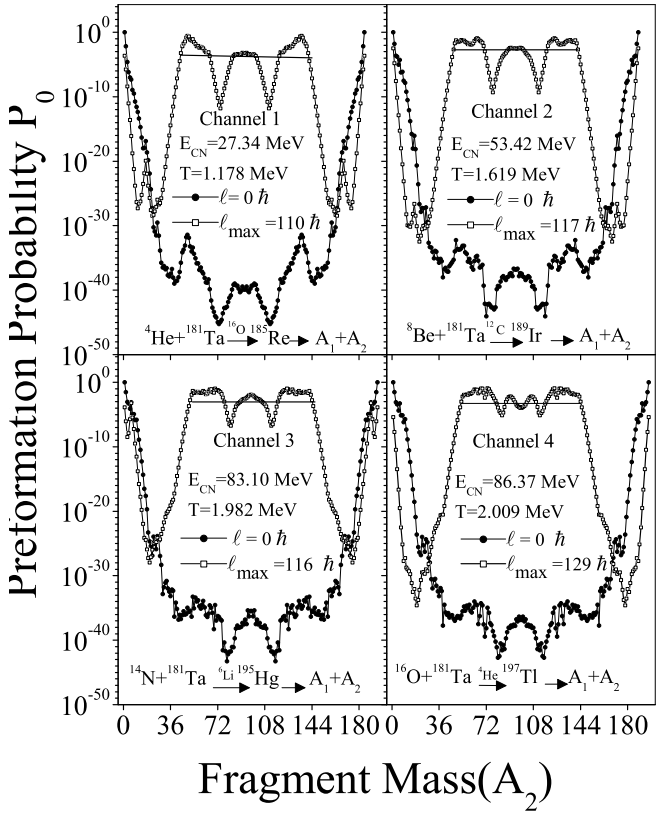

Figure 5.4 Preformation Probability P_0 as a function of Fragment Mass A_2 for ICF transfer channels plotted at E_{lab}=150 MeV and ΔR=1.460 fm using β_2 deformed fragmentation.

of energy of projectile. Moreover, the percentage of f_{ICF} is more for asymmetric transfer channel as compared to relatively symmetric channels, in agreement with the systematics of Morgenstern [28, 29].

Fig. 5.4 shows the preformation probability plotted as a function of fragment mass for all the transfer channels using β_2 deformed approach. The asymmetric mass distribution observed for ^{4}He, ^{8}Be, ^{14}N and ^{16}O transfer reactions is quite similar to that of CN decay (compare Fig.5.4 with middle panel of Fig.5.1). A closer look of Fig. 5.4 shows that the contribution of symmetric fragments becomes more prominent while going from ^{4}He to ^{16}O transfer channel. It may be noted that ERs formed in the four ICF channels in DCM based calculations are similar to the ones reported in Table III of [1]. The

ICF cross-sections calculated using DCM for ^{20}Ne break-up channel are found to have a nice agreement with the experimental measurements [1]. This observation suggests that DCM can be applied to investigate ICF process in addition to the CF mechanism. After exploring the role of deformations and suitable energy corrections in reference to CF and ICF processes observed in ^{20}Ne induced reaction, the DCM is further applied to address CF and ICF component in reference to relatively lighter mass ^{96}Tc* nucleus formed in ^{6}Li induced reaction for which the role of rotational energy is also explored.

5.2.2 CF and ICF analysis of ^{6}Li+^{90}Zr reaction

In a recent experiment [2] carried out to study the fusion of ^{6}Li projectile with medium mass ^{90}Zr target, the complete fusion cross-sections, having major contribution from evaporation residue have been measured over a wide range of incident energy, E_{lab}=14.9-29.9 MeV (equivalently $E_{c.m.}$=13.9-28.0 MeV) spread across the Coulomb barrier. In this reaction, the projectile ^{6}Li being loosely bound nucleus and the target ^{90}Zr, having a double shell closure with $N = 50$ and $Z = 40$ seem to provide a good opportunity to address the decay mechanism of ^{96}Tc* system and thus play an important role in dynamics of the chosen reaction. In view of this, the decay of ^{6}Li+ ^{90}Zr reaction is examined in framework of dynamical cluster-decay model (DCM) [20–27]. It is relevant to state that DCM has been successfully applied to numerous systems for evaporation residue (ERs; $Z_2{\leq}2$,$A_2{\leq}$ 4), intermediate mass fragments (IMFs; 2 $\leq Z_2 \leq$10,5$\leq A_2 \leq$ 20), near symmetric and symmetric fission fragments using sticking limit (I_s) of moment of inertia in which the rotation of two touching spheres is considered about their common center of mass. The choice of moment of inertia in sticking limit is attributed to the use of proximity potentials such as Blocki et.al. [30], in DCM based calculations. On the other hand, for the fission fragment anisotropies it has been observed that DCM [31] approach favors the non-sticking limit

(I_{NS}) of moment of inertia where no intrinsic rotation of fragments is considered due to the small separation distance between them. However, with loosely bound ^{6}Li projectile having radius 10% larger than the normal systematics, an attempt is made to analyze the comparative role of I_S or I_{NS} limit of moment of inertia, for the neutron evaporation decay channel observed in the reaction under consideration.

Apart from these features, another reason for this study is that reactions induced by fragile loosely bound nuclei exhibit a range of phenomena (break-up being one of them) and thus lead to sizable effects on the dynamics of a reaction. It is well known that at higher energies when processes other than complete fusion become important, the fusion cross sections are found to drop below the total reaction cross section. An overall suppression of 34±8 % observed in the fusion cross sections of ^{96}Tc* nucleus [2] suggests the possibility of some competing process such as ICF. Evidently, for smaller systems lying in this mass region, the separation of CF and ICF cross section becomes difficult at both theoretical and experimental level. An attempt is made to separate the CF and ICF components in framework of DCM by associating these processes with the angular momentum bins. The lower angular momentum states upto ℓ_{crit} are associated with CF process and higher ones with ICF process. This is because above ℓ_{crit}, the centrifugal potential suppresses the attractive nuclear potential, due to which the complete fusion of the projectile is hindered, giving rise to the break-up of the projectile and hence the incomplete fusion. In other words, the interplay between the centrifugal and the attractive nuclear potential plays an important role in the dynamics of loosely bound reaction. Thus, the main aim of this work is to study the effect of angular momentum in two different aspects (i) in terms of sticking limit (I_S) and non-sticking limit (I_{NS}) of moment of inertia (ii) for disentangling the contribution of CF and ICF processes for ^{96}Tc* nucleus.

In reference to the measured complete fusion data [2], the evaporation residues having

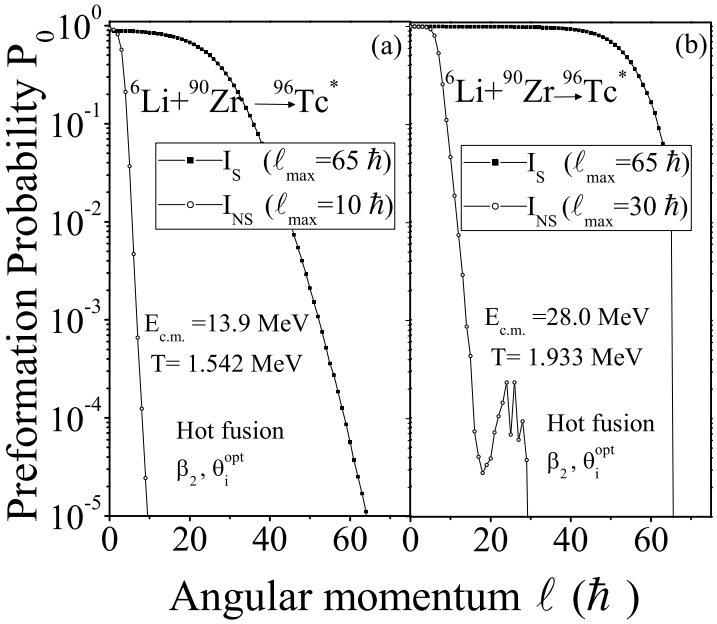

Figure 5.5 The variation of preformation probability P_0 as a function of angular momentum for the use of sticking and non-sticking limit of moment of inertia at (a) $E_{c.m.}$=13.9 MeV (b)$E_{c.m.}$=28.0 MeV.

contribution from neutron cross sections (xn;x=1-3) are calculated using the dynamical cluster-decay model (DCM) for β_2 deformations within optimum orientation (θ_i^{opt}) approach. The deformations $\beta_{\lambda i}$, in DCM are taken from the theoretical estimates of Möller and Nix [32] while the optimum orientations θ_i^{opt} of the hot fusion process are employed in reference to [20]. The behavior of centrifugal potential, fragmentation potential, preformation probability P_0 and the penetrability P is analyzed to look for the possible effect of non-sticking limit (I_{NS}) of moment of inertia in addition to the usually applied sticking limit(I_S).

The role of moment of inertia enters DCM through centrifugal potential (V_ℓ) (shown in Eq. (2.38)) and it is observed that for a given value of centrifugal potential, I_{NS} approach contributes up to fewer units of angular momentum as compared to I_S approach. This result is depicted in Fig. 5.5(a) and (b) which shows the variation of preformation probability P_0 summed up for the most prominent fragments ($\sum$xn;x=1-3), as a function of

angular momentum ℓ at two extreme energies lying across the barrier i.e. $E_{c.m.}$=13.9 and 28.0 MeV. For calculating the neutron-evaporation residue cross sections the preformation probability (P_0) helps to fix the maximum value of angular momentum ℓ_{max}, defined at a point where the magnitude of P_0 is negligibly small (10^{-5}). Clearly, P_0 contributes significantly up to certain ℓ states and drops sharply reaching the limiting value of 10^{-5} at ℓ=ℓ_{max}. Consequently, the ℓ_{max}=65$\hbar$ is observed for sticking limit of moment of inertia at both energies across the barrier. On the other hand for the I_{NS} limit of moment of inertia, P_0 changes considerably in going from below barrier to above barrier energy, due to which ℓ_{max} increases from 10$\hbar$ to 30$\hbar$ on going from $E_{c.m.}$=13.9 MeV to $E_{c.m.}$=28.0 MeV. Comparing Fig. 5.5 (a) and (b) for the I_{NS}-approach, it is observed that the variation of preformation probability with angular momentum is smooth for below barrier energy but not for above barrier. Thus, one may say that the lower limit on preformation probability fixed uniquely for all the energies is responsible for higher ℓ_{max} value at above barrier energy for I_{NS} based calculations.

To further explore the effect of sticking (I_S) and non-sticking (I_{NS}) limit of moment of inertia, the behavior of centrifugal potential is studied as a function of inter nuclear distance R (fm). Fig. 5.6(a) shows the variation of centrifugal potential (V_ℓ) for the use of I_S and I_{NS} approach at maximum energy, $E_{c.m.}$=28.0 MeV in reference to ^{96}Tc*$\rightarrow$^{95}Tc+1n decay channel. To analyze explicitly the effect of moment of inertia, the centrifugal potential has been calculated at a fixed ℓ value (ℓ=16$\hbar$). From the figure it is observed that for small interaction range (up to 10fm) a large difference in the potential is observed for the use of two different limits of moment of inertia. The centrifugal potential decreases very slightly (although not visible due to difference in scale) for the use of sticking limit of moment of inertia whereas for I_{NS} approach significant decrease with an increase in interaction range is observed.

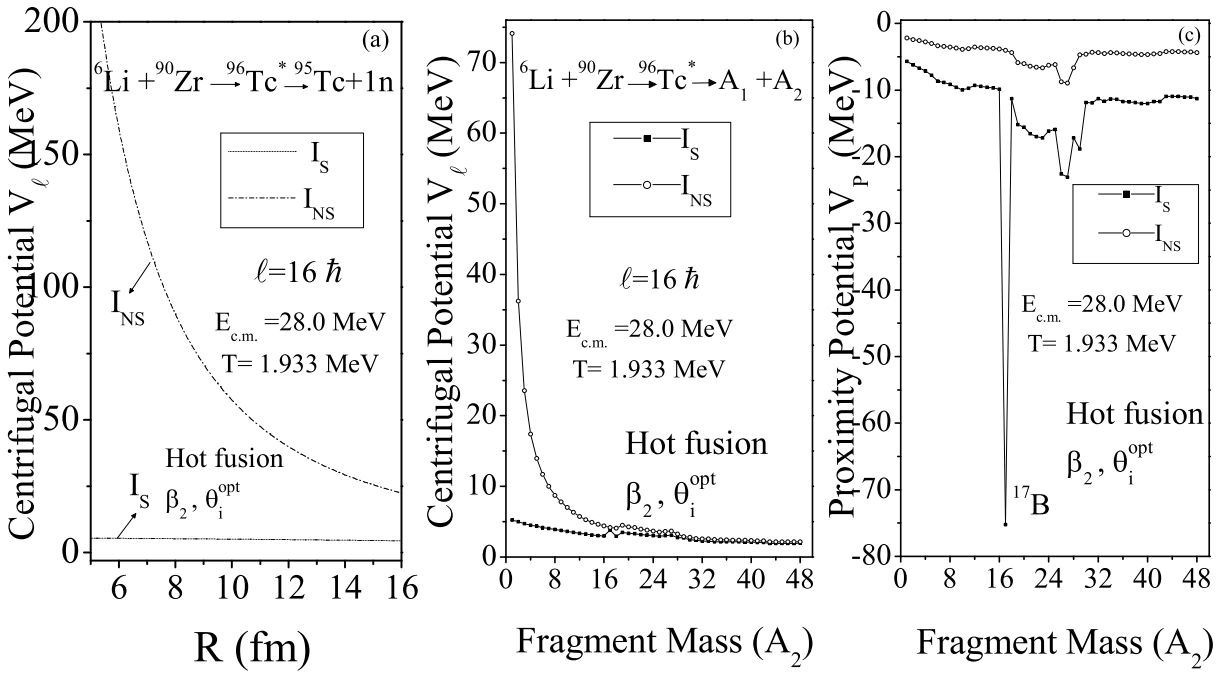

Figure 5.6(a) The centrifugal potential V_ℓ plotted for the $^{96}Tc^{*} \rightarrow ^{95}Tc+1n$ decay channel for both the choices of moment of inertia. (b) Variation of V_ℓ as a function of fragment mass A_2. (c) The proximity potential (V_P) plotted as a function of fragment mass A_2 for decay of $^{96}Tc^{*}$ system at $E_{c.m.}$=28.0 MeV.

The effect of sticking and non-sticking limit of moment of inertia is further investigated in Fig. 5.6(b) which shows the variation of centrifugal potential as a function of fragment mass A_2. The potential corresponding to the I_{NS} limit is much higher as compared to I_S limit for the light fragment mass region whereas, in the IMF and fission region, the potential for both the choices of inertia start overlapping. Apparently, the behavior of V_ℓ depicted in Fig. 5.6(a) and Fig. 5.6(b) suggests that the effect of moment of inertia is more prominent in the small interaction range and lighter cluster or fragment masses. Also, the variation of proximity potential (V_P) for both the choices of moment of inertia is shown in Fig.5.6(c). It is observed that the short range proximity potential (defined in Eq. (2.26)) follows relatively similar variation for all decaying fragments, only exception being the magnitude is higher for the I_{NS} approach. Besides this, relatively more structure effects are observed for the use of sticking limit of moment of inertia as compared to the non-

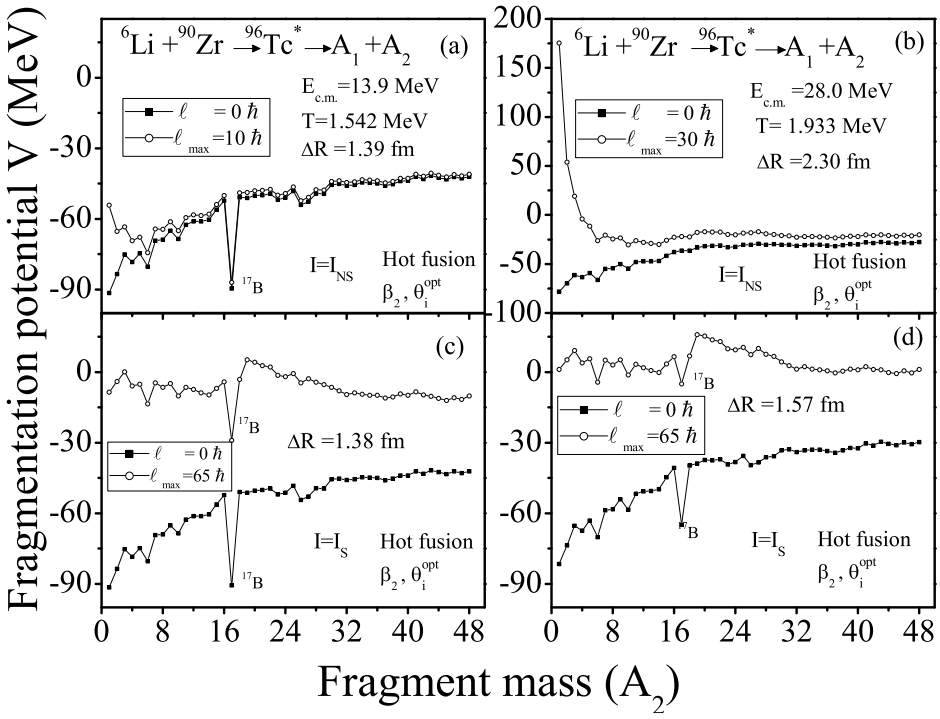

Figure 5.7 The variation of fragmentation potential as a function of fragment mass A_2 for decay of ^{96}Tc* system at $E_{c.m.}$=13.9 MeV and $E_{c.m.}$=28.0 MeV with non-sticking moment of inertia shown in panel (a),(b) and sticking moment of inertia in panel (c),(d).

sticking limit. It must be noted that with the inclusion of β_2 deformations an unexpected minimum is observed for the ^{17}B fragment. The probable reason for this may be the inappropriate value of β_2 deformations and a possible remedy to this sharp minimum is addressed later in explanation of Fig. 5.10.

With the use of centrifugal potential as a part of the long range interaction potential in DCM, it has been observed that for the fusion-fission decay channels the sticking limit of moment of inertia is more appropriate [31]. However, recent investigation on superheavy system Z=112 [33], seem to suggest that I_{NS} is equally probable for addressing the neutron evaporation residue cross sections as well. This observation seems justified as relatively lower angular momentum states contribute towards neutron evaporation via ER decay as compared to fission decay. In view of this, we intend to explore the comparative study of I_S

and I_{NS} in reference to neutron evaporation cross sections for the intermediate mass $^{96}Tc^*$ nucleus. In order to explore the dynamics of $^{96}Tc^*$ nucleus, the fragmentation potential for the use of I_{NS} approach at extreme energies lying across the barrier, is shown in Fig. 5.7(a) and (b) while Fig. 5.7 (c) and (d) represent the use of I_S approach at $E_{c.m.}$=13.9 MeV and $E_{c.m.}$=28.0 MeV respectively. Fig. 5.7 clearly shows that the choice of moment of inertia explicitly governs the centrifugal potential V_ℓ, which in turn influences the fragmentation potential. At ℓ=0$\hbar$, due to the absence of ℓ effect the behavior of fragmentation potential is similar for I_{NS} and I_S approach at both energies across the barrier. A small difference at higher incident energy may be attributed to the difference in neck-length parameter ΔR. Also, a small increase in the magnitude of potential is observed while going from below barrier to above barrier energy. At ℓ=ℓ_{max}, the potential energy surfaces show a similar behavior for the I_{NS} and I_S choice of inertia at minimum energy below the barrier i.e. $E_{c.m.}$=13.9 MeV, but a drastic change is observed at highest energy, $E_{c.m.}$=28.0 MeV lying above the Coulomb barrier.

It must be noted that when the I_S limit is replaced by I_{NS} a large increase in magnitude of fragmentation potential is observed in the ER region. This enhancement in magnitude of fragmentation potential may be associated with higher centrifugal potential of lighter fragments for the use of I_{NS} approach (as shown in Fig. 5.6(b)). In terms of DCM calculations, higher fragmentation corresponds to lower preformation probability and hence relatively less favorable decay. Thus, due to larger magnitude of fragmentation potential for I_{NS} approach at $E_{c.m.}$=28.0 MeV and ℓ=ℓ_{max}, the decay of compound system in form of neutron evaporation residue becomes more favorable for the use of sticking limit of moment of inertia. On the basis of fragmentation profile, one may say that both the sticking as well non-sticking limit of moment of inertia respond almost equally at near and below barrier region whereas, at above barrier energy, the sticking limit of inertia

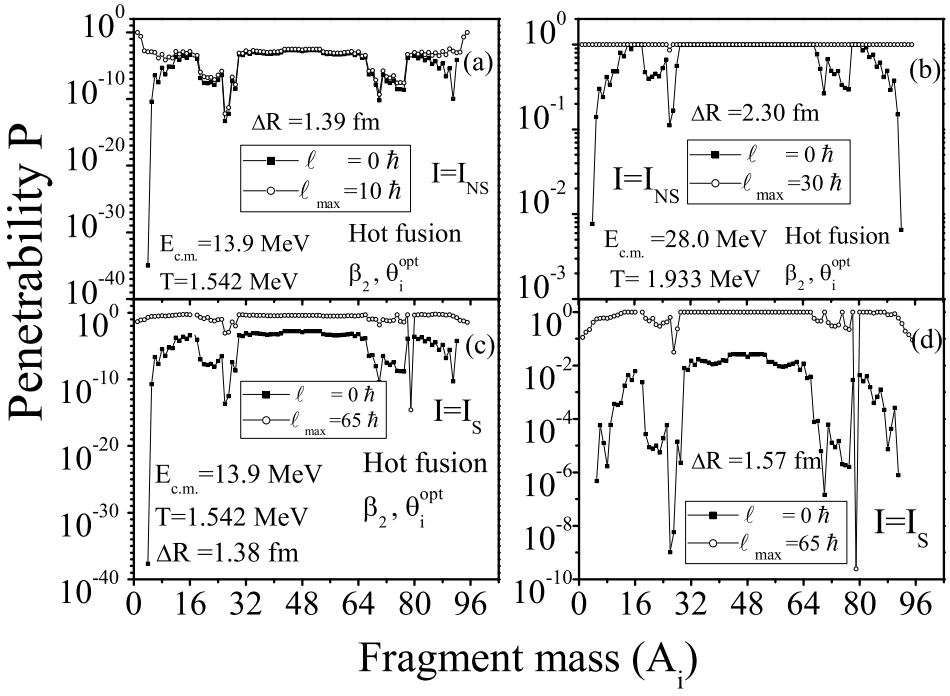

Figure 5.8 Penetrability P as a function of fragment mass A_i (i=1,2) shown at extreme energies across the barrier for the I_{NS} limit (parts a,b) and the I_S limit of moment of inertia (parts c,d) .

seems a better choice. Also, the structure effects due to proximity forces are more evident for the use of I_S limit of moment of inertia as compared to I_{NS} limit. It is relevant to mention here that, the dip at ^{17}B fragment appears due to large decrement in magnitude of proximity potential for this fragment as mentioned in Fig. 5.6(c).

It is observed that on going from below barrier to above barrier energy, the fragment mass distribution varies for both I_S and I_{NS} approaches. The observed change in structure across the Coulomb barrier is relatively more for the I_{NS} limit as compared to the I_S limit. It is worth mentioning that at below barrier energy, not much change in behavior of P_0 of light mass fragments is observed for I_{NS} and I_S approach hence, the ERs (with $A_2 \leq 4$) dominate for both the choices. However, at above barrier energy the formation probability of ERs is small for the use of non-sticking limit of moment of inertia as compared to sticking limit and hence the latter seems a better option.

Table 5.3 The DCM calculated neutron evaporation residue cross sections considering quadrupole (β_2) deformation for the use of sticking (I_S) and non-sticking (I_{NS}) limit of moment-of-inertia for the decay of ^{96}Tc* compound system formed in ^{6}Li+^{90}Zr reaction compared with the experimental data [2].

S. No.	$E_{c.m.}$	E^*_{CN}	T	ΔR		ℓ_{max}		σ^{DCM}		$\sigma^{Expt.}$
	(MeV)	(MeV)	(MeV)	I_S(fm)	I_{NS}(fm)	$I_S(\hbar)$	$I_{NS}(\hbar)$	I_S(mb)	I_{NS}(mb)	(mb)
1	13.9	23.84	1.542	1.38	1.39	65	10	1.30	1.29	1.30±0.2
2	14.9	24.84	1.573	1.40	1.41	65	13	6.13	6.30	6.30±0.6
3	15.8	25.74	1.601	1.43	1.44	65	15	27.02	26.3	27.00±2
4	16.8	26.74	1.631	1.45	1.47	65	16	62.10	63.71	63.00±4
5	17.7	27.64	1.657	1.46	1.50	65	18	115.00	114.00	114.00±7
6	19.6	29.54	1.711	1.50	1.62	65	22	228.00	224.00	230.00±11
7	23.3	33.24	1.813	1.53	1.95	65	28	510.00	507.00	510.00±24
8	28.0	37.94	1.933	1.57	2.30	65	30	774.00	753.00	778.00±37

Since, the cross sections calculated using DCM also depend upon penetrability (P) (see Eq.2.50), the effect of moment of inertia for the same is also explored. In Fig. 5.8, penetrability is plotted as a function of fragment mass (A_i) for the use of sticking and non-sticking limit of moment of inertia. It is clearly depicted that barrier penetrability increases when sticking approach is replaced by non-sticking one. The enhancement in penetrability for I_{NS} choice is more at higher $E_{c.m.}$ as compared to that for lower energy. The variation in P_0 and P is responsible for significant change in the cross sections. Interestingly, for ^{96}Tc* nucleus P_0 decreases and P increases when I_{NS} choice of interaction is preferred over I_S. Therefore, the dependence of decay cross section on I_S or I_{NS} approach provide quite interesting scenario in reference to the dynamics of heavy ion reactions for the use of I_{NS} limit. In case of ^{96}Tc* it is observed that the enhancement in P is steeper as compared to decrease in P_0 and hence higher ΔR is required to address the neutron evaporation data particularly at above barrier energies.

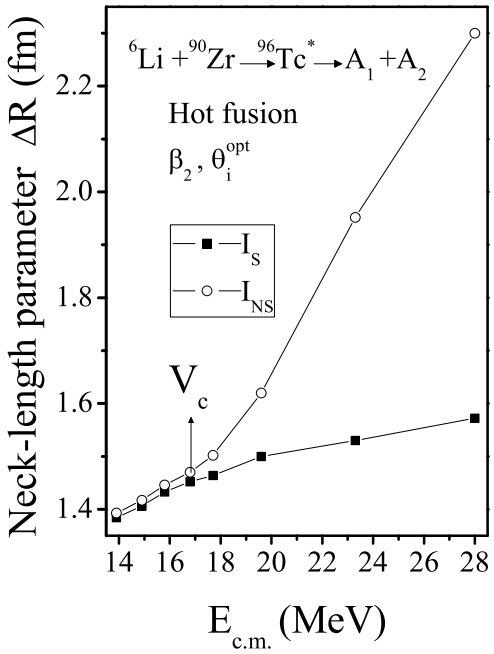

Figure 5.9 The best fitted neck-length parameter ΔR corresponding to the neutron-ER decay channel, for the use of sticking and non-sticking limit of moment of inertia plotted as a function of $E_{c.m.}$ for the ^{6}Li+^{90}Zr reaction.

An explicit representation of the results obtained from these calculations (for β_2 deformation) is given in Table 5.3, where the best fitted ΔR values in reference to the calculated neutron-ER cross sections for the use of sticking and non-sticking limit of moment of inertia are presented along with the measured cross-sections [2]. A nice agreement with the experimental data is obtained for both the sticking and non-sticking limits at different center-of-mass energies. Corresponding to the fitted neutron-ER cross sections, the ΔR values are also depicted as a function of center-of-mass energy in Fig. 5.9. The value of ΔR remains almost similar for the sticking and non-sticking limit of moment of inertia for all energies lying below the Coulomb barrier ($E_{c.m.}$=16.9 MeV). However at above Coulomb barrier energies, the difference in ΔR values used for sticking and non-sticking limit increases with increase in energy. In general the upper limit on ΔR is fixed around 2 fm to justify the use of proximity potential. In the present case since the data

Table 5.4 The DCM calculated neutron evaporation residue cross sections obtained through CF process up to ℓ_{CF} (denoted for ℓ corresponding to 0.65-1.2ℓ_{crit}) at various $E_{c.m.}$ values compared with experimental complete fusion (CF) data [2]. The ℓ_{crit} used to decide the ℓ_{CF} is 36$\hbar$ and ΔR =1.9fm.

S. No.	$E_{c.m.}$ (MeV)	E^*_{CN} (MeV)	T (MeV)	ℓ_{CF} ($\hbar$)	σ_{CF}^{DCM} (mb)	$\sigma_{CF}^{Expt.}$ (mb)
1	13.9	23.84	1.542	23	1.12	1.30±0.2
2	14.9	24.84	1.573	26	7.00	6.30±0.6
3	15.8	25.74	1.601	29	30.00	27.00±2
4	16.8	26.74	1.631	31	63.00	63.00±4
5	17.7	27.64	1.657	33	119.00	114.00±7
6	19.6	29.54	1.711	36	254.00	230.00±11
7	23.3	33.24	1.813	40	531.00	510.00±24
8	28.0	37.94	1.933	43	740.00	778.00±37

is addressed by taking ΔR up to 2 fm (except for the highest energy for I_{NS} case), it may be concluded that both approaches seem to be equally capable of handling the neutron evaporation residue data for the intermediate mass ^{96}Tc* nucleus with I_S being favorable approach at higher incident energies. In view of this the further study involves the use of sticking approach only.

It is worth noting that, an overall suppression in the measured complete fusion cross sections has been observed [2] in comparison to coupled channel calculations. This suppression is associated with the incomplete fusion (ICF) observed due to break up of ^{6}Li projectile having two body cluster structure (α+ d) and low break-up threshold. The experimental observations suggest the possible contribution of ICF through the ^{4}He+^{90}Zr reaction in form of ^{93}Mo+1n decay channel and the same is tested in framework of DCM. So far for the ICF process the cross sections were calculated corresponding to the best fitted neck-length parameter ΔR up to ℓ=ℓ_{max}. However, in the dynamics of ^{6}Li +^{90}Zr reaction, the CF and ICF cross sections have been separated by confining their contributions in two different ℓ-windows. In other words, the earlier calculations for ICF have

Table 5.5 The ICF cross sections for 1-neutron decay channel calculated using DCM with quadrupole (β_{2i}) deformation for ^{94}Mo* nucleus formed in ^{4}He+^{90}Zr reaction at corrected $E_{c.m.}$ values compared with incomplete fusion (ICF) data [2]. Also shown are the best fitted ΔR values and the ℓ_{ICF}^{min} (denoted for ℓ>ℓ_{CF}). The maximum angular momentum is ℓ_{max}=65$\hbar$.

S. No.	$E_{c.m.}$ (MeV)	E^{*}_{CN} (MeV)	T (MeV)	ΔR_{ICF} (fm)	ℓ_{ICF}^{min} ($\hbar$)	σ_{ICF}^{DCM} (mb)	$\sigma_{ICF}^{Expt.}$ (mb)
1	9.5	11.4	1.093	0.94	24	34.00	38.00
2	10.1	12.0	1.122	1.00	27	62.00	71.00
3	10.8	12.7	1.150	1.07	30	125.00	131.00
4	11.4	13.3	1.177	1.12	32	190.00	196.00
5	12.1	14.0	1.204	1.17	34	285.00	300.00
6	13.3	15.2	1.256	1.23	37	441.00	445.00
7	15.9	17.8	1.353	1.28	41	543.00	560.00
8	19.1	21.0	1.466	1.33	44	588.00	597.00

been done by applying relevant and necessary energy corrections [3] to obtain the energy of the new projectile involved, however the concept of different ℓ-windows for CF and ICF processes is exercised only for ^{6}Li +^{90}Zr reaction. Following the observation of [2], the ICF cross section have been obtained by deducting the CF cross-sections from the total reaction cross-section and also subtracting average contribution of ∼7.5% (taken average of measured contribution of 5-10%) for the exclusive break-up (BU) cross section, i.e,

$$\sigma_{ICF} = \sigma_{Reaction} - \sigma_{CF} - \sigma_{BU} \tag{5.2}$$

The above equation gives an upper limit of incomplete fusion cross-section as the contribution of direct reactions other than breakup is not included in it. In view of [34] for $\ell \leq \ell_{crit}$ CF process dominates while for $\ell > \ell_{crit}$ ICF starts contributing. However, in addition to the centrifugal and nuclear potential, the localization of ℓ-window may also depend on other features such as the target deformation and semi-magic nature of nuclei [35], as a result the onset of ICF has been observed for ℓ values lying even below $0.5\ell_{crit}$ [36]. Also, in some cases CF and ICF have been observed both above and below

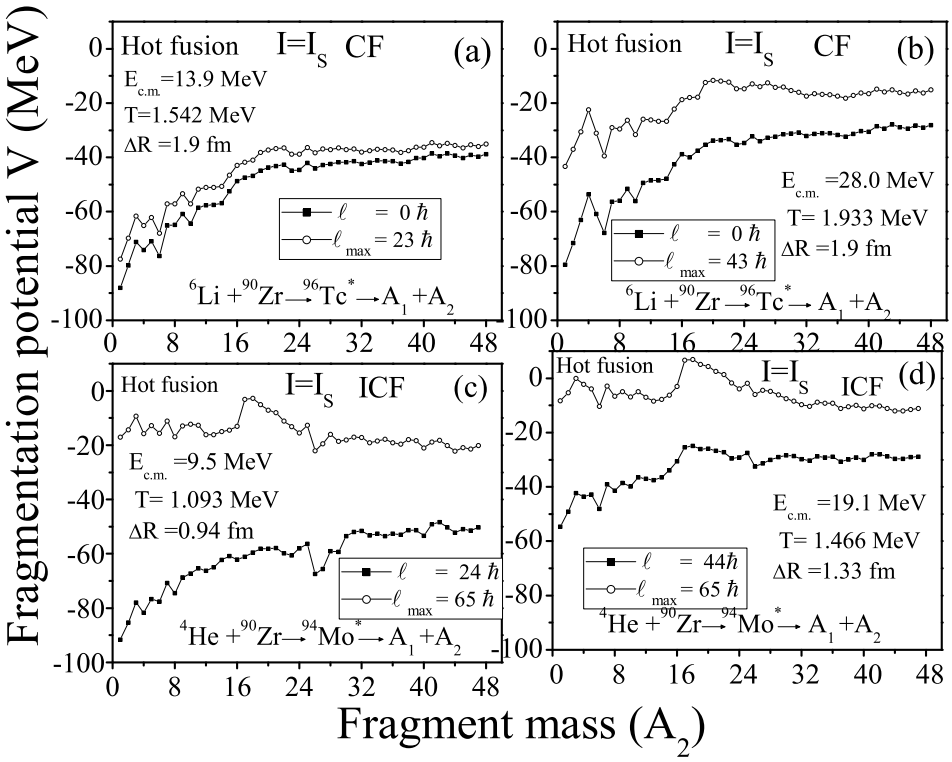

Figure 5.10 (a),(b) Fragmentation Potential V (MeV) for fragments formed through complete fusion (CF) process in ^{6}Li+ ^{90}Zr reaction and (c),(d) for incomplete fusion (ICF) process in ^{4}He+ ^{90}Zr reaction (observed due to the break-up of ^{6}Li), with inclusion of quadrupole (β_{2i}) deformation.

the ℓ_{crit}. Therefore, the main aim here is to the study the CF and ICF contributions in reference to ℓ_{crit} in framework of DCM. The critical ℓ-value, ℓ_{crit}=36$\hbar$ here, is decided at a point where the centrifugal potential approaches the proximity potential, i.e. $V_\ell \sim V_P$. The cross sections for CF have been calculated for ℓ-values lying between ℓ=0$\hbar$ to ℓ=ℓ_{CF} whereas, ICF cross sections have been obtained for $\ell_{CF}<\ell\leq\ell_{max}$. It is worth mentioning here that ℓ_{CF} varies from $0.65\ell_{crit}$ to $1.2\ell_{crit}$ with increase in incident energy. The possible cause for the deviation of ℓ_{CF} from ℓ_{crit} may be associated with deformations of decaying fragments involved in the collective clusterization process. The calculated cross-sections at varied range of incident energies, for CF and ICF processes with the corresponding ℓ values are tabulated in Table 5.4 and Table 5.5 respectively.

Fig. 5.10 shows the variation of fragmentation potential V(MeV) for CF and ICF

processes. The calculation for both the decay processes have been done with the inclusion of β_2 deformations. From the figure it is clear that the overall fragmentation path is almost similar for CF and ICF processes at two extreme energies lying across the barrier. An unexpected minima was observed with the inclusion of β_2 deformations as in Fig. 5.6(c) and Fig. 5.7. However, from Fig. 5.10 (a,b), it is observed that for the calculations of CF done using higher ΔR the minimum at ^{17}B disappears. This is due the fact that at higher ΔR values, the minimized fragment ^{17}B is replaced by ^{17}O. While for the ICF calculations done at lower ΔR values, the ^{17}B dip continues to exist (graph not shown here). To rectify this, the deformation of ^{17}B fragment has been modified from -0.398 to 0.62 as obtained from relativistic calculations using NL3 force [37]. With this deformation, the unexpected dip has been removed as observed in Fig. 5.10(c),(d). The comparison of Fig. 5.10 with Fig.5.7(c,d) suggests that CF process follows the structural path of lower angular momentum state and ICF process follows the one of higher angular momentum. It is so because in these calculations lower angular momentum states are shown to influence CF process and higher ones are applicable for ICF component.

The DCM based CF and ICF cross sections are found to be in nice agreement with data of [2]. Interestingly, the results for CF are obtained nicely at a fixed ΔR=1.9 fm and ℓ=ℓ_{CF}. However, for ICF ΔR increases linearly as a function of energy (see Table 5.5). A comparative study of calculated DCM cross-sections with experimental data showing contributions of CF and ICF processes is shown in Fig.5.11. It must be noted that decay of CF is through contribution of xn;x=1-3 whereas for ICF only 1n channel contributes.

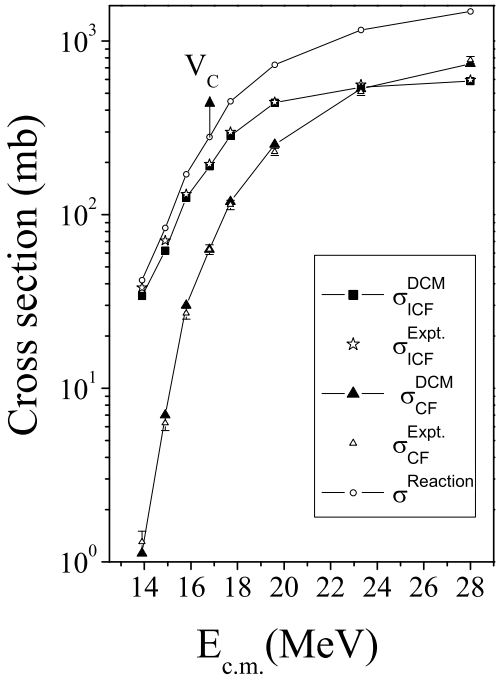

Figure 5.11 Comparison of DCM cross-sections having contribution from complete fusion and incomplete-fusion processes with the data [2] at different center-of-mass energies.

5.3 Summary

The ER cross-sections for ^{201}Bi* system formed through compete fusion of ^{20}Ne projectile with ^{181}Ta target are nicely addressed for spherical, β_2 deformed and β_2-β_4 deformed choice of fragmentation. The deformations seem to play significant role for either of the chosen energies at higher ℓ values i.e. at ℓ=ℓ_{max}. The fragmentation mass distribution is observed to be symmetric for spherical choice of fragmentation and becomes near-symmetric with the inclusion of deformation effects. However, at higher energy, the mass distribution becomes asymmetric with inclusion hexadecapole deformations. The barrier modification, which comes in a natural way with in DCM approach, seems more desirable at higher value of compound nucleus energy ($E_{CN}{}^{*}$) and lower value of angular momentum. The role of deformations, angular momentum and barrier modification is explored in context to ^{20}Ne induced reaction. In addition to this, the DCM is also applied to study

ICF process observed due to beak-up of ^{20}Ne projectile into four dominant channels. The ER cross-sections formed in these four channels, calculated at fixed ΔR value are summed up to account for reported ICF cross-sections at E_{lab}=150 MeV and E_{lab}=180 MeV. Amongst the ^{4}He, ^{8}Be, ^{14}N and ^{16}O transfer channels, the ^{4}He induced reaction contributes maximum towards the ICF cross-sections. The asymmetric fragmentation is observed for all four channels for the use of qaudrupole deformation and fragments in the mass range A_2= 181-197 contribute towards ICF process which are in agreement with the experimental observations.

In addition to this it is observed that sticking and non-sticking limit of moment of inertia affect the decay of $^{96}Tc^{*}$ system. The neutron evaporation residue cross sections have been attained for both the approaches, where I_S favors relatively larger angular momentum states. The effect of I_{NS} is more prominent for the small interaction range and light fragment region ($A_2 \leq 4$) and starts approaching the behavior of I_S limit for higher range and fragment mass. The neck-length parameter ΔR is almost similar for the sticking and non-sticking limit of moment of inertia at energies lying below the Coulomb barrier ($E_{c.m.}$=16.9 MeV) but is higher for non-sticking limit at above barrier energies. In general one may conclude that both the processes respond to neutron evaporation data equally well with I_S showing slight favor at above barrier region. The ICF contribution is also investigated within DCM approach by suggesting different ℓ-windows for CF and ICF component. The successful representation of ER cross-section formed in CF and ICF processes for both the reactions, conclude that DCM can be applied successfully for CF as well as ICF processes.

It may be noted that, decay cross-sections obtained through CF and ICF processes are studied for both heavy and intermediate mass region in this chapter. It will be of further interest to carry out the decay analysis of light mass region by exploring decay

of $^{66}As^{*}$ nucleus formed in p-halo induced reaction and by studying charge distribution observed in $^{40}Ca^{*}$ and $^{39}K^{*}$ nuclei. This work is presented in chapter 6.

Bibliography

[1] R.Tripathi, K.Sudarshan, A. Goswami, R. Guin, and A.V. Reddy, Phys.Rev. C **74**, 014610 (2006).

[2] H. Kumawat, V. Jha, V. V. Parkar, B. J. Roy, S. K. Pandit, R. Palit, P. K. Rath, C. S. Palshetkar, S. K. Sharma, S. Thakur, A. K. Mohanty, A. Chatterjee, and S. Kailas, Phys. Rev. C **86**, 024607 (2012).

[3] G. Kaur and M. K. Sharma, Nucl. Phys. A **884**, 36 (2012).

[4] G. Kaur, N. Grover, K. Sandhu, and M. K. Sharma, Nucl. Phys. A **927**, 232 (2014).

[5] J. Wilczynski et.al., Phys. Rev. Lett. **45**, 606 (1980); Nucl. Phys. A **373**,109 (1982).

[6] K. A. Geoffroy, D. G. Sarantites, M. L. Halbert, D. C. Hensley, R. A. Dayras and J. H. Barker, Phys. Rev. Lett. **43**, 1303 (1979).

[7] W. Trautmann, O.Hansen, H. Tricoire, W. Hering, R. Ritzka, and W. Trombik, Phys. Rev. Lett. **53**, 1630 (1984).

[8] T.Inamura et.al., Phys. Lett. B **68**, 51 (1977); **84**, 71 (1982); T.Inamura, A. C. Kahler, D. R. Zolnowski, U. garg, T. T. Sugihara, and M. Wakai, Phys. Rev. C **32**, 1539 (1985).

[9] M. B. Tsang, D. R. Klesch, C. B. Chitwood, D. J. Fields, C. K. Gelbke, W. G. Lynch, H. Utsunomiya, K. Kwiatkowski, V. E. Viola Jr., and M. Fatyga, Phys. Lett. B **134**, 169 (1984).

[10] H. Oeschler, M. Kollatz, W. Bohne, K. Grabisch, H. Lehr,H. Freiesleben, and K. D.Hildenbrand, Phys. Lett. B **127**, 177 (1983).

[11] P. E. Hodgson, E. Gadioli, and E. Gadioli Erba, *Introductory Nuclear Physics* (Clarendon Press, Oxford), Chap. 23 (1997).

[12] H. C. Britt and A. R. Quinton, Phys. Rev. **124**, 877 (1961).

[13] T. Udagawa and T. Tamura, Phys. Rev. Lett. **45**, 1311 (1980).

[14] J. P. Bondorf, J. N. De, G. Fai, A. O. T. Karvinen, and J. Randrup, Nucl. Phys. A **333**, 285 (1980).

[15] D. P. Singh, Unnati, P. P. Singh, A. Yadav, M. K. Sharma, B. P. Singh, K. S. Golda, R. Kumar, A. K. Sinha, and R. Prasad, Phys. Rev. C **80**, 014601 (2009).

[16] P. P. Singh, B. P. Singh, M. K. Sharma, Unnati, D. P. Singh, R. Prasad, Phys.Rev. C **77**, 014607 (2008) .

[17] L. F. Canto, P. R. S. Gomes, R. Donangelo, and M. S. Husssein, Phys. Rep. **424**, 1 (2006) and references therein.

[18] M. Dasgupta, P. R. S. Gomes, D. J. Hinde, S. B. Moraes, R. M. Anjos, A. C. Berriman, R. D. Butt, N. Carlin, J. Lubian, C. R. Morton, J. O. Newton, and A. Szanto de Toledo, Phys. Rev. C **70**, 024606 (2004).

[19] A. Mukherjee, S. Roy, M.K. Pradhan, and M.Saha Sarkar et.al., Phys. Lett. B **636**, 91 (2006).

[20] R. K. Gupta, M. Balasubramaniam, R. Kumar, N. Singh, M. Manhas, and W. Greiner, J. Phys.G : Nucl. Part. Phys. **31**, 631 (2005).

[21] R. K. Gupta, M. Manhas, W. Greiner, Phys. Rev. C **73**, 054307 (2006).

[22] M. Balasubramaniam, R. Kumar, R. K. Gupta, C. Beck, and W. Scheid, J. Phys. G : Nucl.Part. Phys. **29**, 2703 (2003).

[23] M. K. Sharma, Shefali Kanwar, Gudveen Sawhney, R.K.Gupta, and W.Greiner, J. Phys. G: Nucl. Part. Phys. **38**, 055104 (2011).

[24] D. Jain, R. Kumar, and M. K. Sharma, Phys. Rev. C **85**, 024615 (2012).

[25] K. Sandhu, M. K. Sharma, and Raj K.Gupta, Phys. Rev. C **85**, 024604 (2012).

[26] M. Kaur, R. Kumar, and M. K. Sharma, Phys. Rev. C **85**, 014609 (2012).

[27] G. Sawhney, G. Kaur, M. K. Sharma, and R. K. Gupta, Phys. Rev. C **88**, 034603 (2013).

[28] H. Morgenstern, W. Bohne, W. Galster, K. Grabisch, A. Kyanowski, Phys. Rev. Lett. **52**, 1104 (1984).

[29] H. Morgenstern, *et al.,* Z. Phys. A **313**, 39 (1983).

[30] J. Blocki, J. Randrup, W. J. Swiatecki, and C. F. Tsang, Ann. Phys. (NY) **105**, 427 (1977).

[31] G. Sawhney, R. Kumar, and M. K. Sharma, Phys. Rev. C **86**, 034613 (2012).

[32] P. Möller, J. R. Nix, W. D. Myers, and W. J. Swiatecki, At. Nucl. Data Tables **59**, 185 (1995).

[33] R. K Gupta, Niyti, M. Manhas, and W. Greiner, J. Phys. G: Nucl. Part. Phys. **36**, 115105 (2009).

[34] P. P. Singh, A. Yadav,D. P. Singh, U. Gupta, M. K. Sharma, R. Kumar,D. Singh, R. P. Singh, S. Muralithar, M. A. Ansari, B. P. Singh, R. Prasad, and R. K. Bhowmik, Phys. Rev. C **80**, 064603 (2009).

[35] C. Gerschel, Nucl. Phys. A **387**, 297 (1982).

[36] H. Tricoire, C. Gerschel, A. Gillibert, and N. Perrin, Z. Phys. A **323**, 163 (1983); R. L. Robinson et al., Phys. Rev. C **24**, 2084 (1981);H. Utsunomiya, T. Nomura, M. Ishihara, T. Sugitate, K. Ieki, and S. Kohmoto, Phys. Lett. B **105**, 135 (1981).

[37] P. Arumugam, B. K. Sharma, S. K. Patra, and R. K. Gupta, Phys. Rev. C **71**, 064308 (2005).

Chapter 6

Decay analysis of nuclei in light mass region

After exploring the dynamics of heavy and intermediate mass nuclei in reference to complete fusion and incomplete fusion processes, the DCM is further applied to study the decay of light mass nuclei. In pursuance of this, the dynamics of $^{66}As^{*}$ nucleus formed in proton halo induced reaction and that of $^{40}Ca^{*}$, $^{39}K^{*}$ nuclei formed in ^{12}C and ^{11}B induced reaction is studied. It is relevant to mention here that so far in this thesis, the decay processes such as ER, fission, quasi fission etc. are addressed while the present chapter involves the individual contribution of various decay modes, mass identification and its contribution corresponding to a given charge and analysis of a non-compound nucleus process i.e., Deep Inelastic Collision (DIC). In reference to the measured fusion cross-sections of $^{66}As^{*}$ system, the comparative analysis of different decay modes is analyzed and their contribution towards the total fusion cross-section is studied. Also the role of higher multipole deformations is explored for the same. Besides this, the collective clusterization approach is employed to identify the favorable fragment mass(es) contributing towards the measured charge distribution for the $^{40}Ca^{*}$, $^{39}K^{*}$ nuclei. Also, the application

of DCM is made for DIC process by studying the decay pattern of these two nuclei. The decay profile of ^{66}As* is published in [1] and that of ^{40}Ca*, ^{39}K* nuclei in [2]. By exploring all the above mentioned aspects in the present chapter, this thesis presents a comprehensive picture of reaction dynamics involved in complete fusion, incomplete fusion and non-compound nucleus processes observed for a variety of nuclei extending over a wide mass range.

6.1 Introduction

In order to investigate the dynamics involved in a nuclear reaction, vigorous research has been carried out over a wide compound nucleus mass (A_{CN}) regime. Apparently, different mass regions show numerous characteristics which prove to be of tremendous importance in understanding the nuclear structure and the underlying nuclear forces. Interestingly, many distinctive features have been observed in the decay of light mass nuclear systems, which distinguish them from one's lying in heavier mass region. Thus, the investigation of decay patterns observed in light mass nuclei is equally important for thorough understanding of nuclear dynamics. In view of this, the present chapter presents the study of $^{66}As^{*}$ nucleus in Sec.6.2 and that of ^{40}Ca*, ^{39}K* nuclei in Sec.6.3. Finally the results are summarized in Sec.6.4.

6.2 Decay of $^{66}As^{*}$ formed in ^{8}B induced reaction

The discovery of nuclear halos plays a significant role in understanding nuclear structure and associated reaction dynamics. Owing to this, a lot of work has been done to study the dynamical effects associated with the reactions involving p-halo and n-halo nuclei [3–6]. Recently, an experiment was performed to measure fusion cross-sections of

$^{66}As^*$ nucleus formed in proton-halo ^8B induced reaction [7]. The fusion of ^8B nucleus (which lies near the proton drip line) with ^{58}Ni is the first known case of its kind, and therefore, studying its decay pattern may impart useful information regarding the overall behavior of ^{66}As* nucleus. In view of this, the DCM [8–16] is applied to look for dominant decay mode contributing towards the decay of $^{66}As^*$ nucleus by studying the light particles (LPs), intermediate mass fragments (IMFs) and fission fragments. It is worth noting that DCM treats all processes [i.e., light particles (LPs; $Z_2 \leq 2$, $A_2 \leq 4$), intermediate mass fragments (IMFs; $5 \leq A_2 \leq 20$) and fission fragments] on equal footing as the dynamic collective mass motion of preformed clusters or fragments through the barrier, and it therefore holds a distinct advantage over other available statistical models. In addition to the decay processes, another aspect worth studying is the role of deformations on the decay of light mass nucleus. It has been observed in previous chapters that DCM having both deformations and orientations degree of freedom included into it, provides worthwhile information for the decay of heavy and intermediate mass nuclei. To check for the consistency of earlier results, the decay of light mass $^{66}As^*$ nucleus formed in the $^8B+$ ^{58}Ni reaction is investigated by fitting the available fusion cross section data using (i) spherical fragmentation approach, (ii) quadrupole deformations (β_{2i}) within optimum orientation approach [15] and (iii) deformation effects up to the hexadecapole (β_{2i}-β_{4i}) with the compact orientation approach [16]. The role of both quadrupole (β_{2i}) and hexadecapole (β_{2i}-β_{4i}) deformations is observed in the fragmentation potential, preformation probability (P_0) and barrier modification ($\Delta\ V_B$). Besides this, the decay cross sections for $^{66}As^*$ nucleus are also estimated at three higher energies. The details of calculations performed and results obtained are presented in the following.

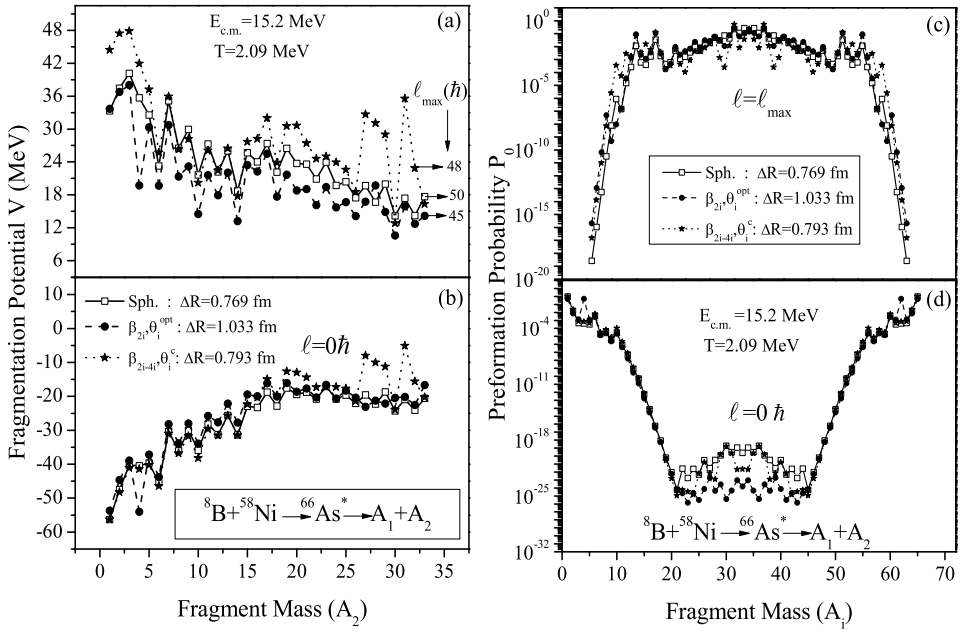

Figure 6.1(a),(b) The fragmentation potential V (MeV) as a function of fragment mass. (c),(d) Preformation probability P_0 as a function of fragment mass A_i(i=1,2) for energetically favored fragments of the compound system $^{66}As^*$ formed in the $^{8}B+$ ^{58}Ni reaction at $E_{c.m.}$=15.2 MeV using spherical and deformed choices of nuclei.

6.2.1 Calculations

Fig. 6.1(a,b) illustrates the fragmentation potentials V (MeV) for the decay of the parent nucleus ^{66}As* at $E_{c.m.}$=15.2 MeV (T=2.09 MeV) at two extreme ℓ values, ℓ=ℓ_{max} (Fig. 6.1 (a)) and ℓ=0$\hbar$ (Fig. 6.1(b)). At ℓ=0$\hbar$, hexadecapole-deformation effects are evident for $A_2 \geq 20$, but no β_{2i} deformation effects are apparent. In contrast, at higher ℓ values both deformations (up to β_{2i} and β_{4i}) play a significant role in the fragmentation process. Moreover, at lower and higher ℓ values, the α- nucleus structure is prominent for spherical and quadrupole deformed cases. It is evident from Fig. 6.1 that the ℓ_{max} value changes with the inclusion of deformation effects, being smallest for β_{2i}-deformed case and comparable for β_{2i}-β_{4i} and spherical fragmentation. A similar behavior of the potential energy surfaces (PES) is also observed at the highest energy, except for some changes in the magnitude of the fragmentation potential. Hence, the role of deformations

Table 6.1 Calculated fusion cross sections $\sigma_{fusion}^{Cal.}$ with the individual contributions from all possible decay processes, i.e., LPs, IMFs and fission fragments, and their sum $\sum_{fusion}^{DCM}$ compared to the experimental fusion cross section $\sigma_{fusion}^{Expt.}$ [7] for the $^{8}B+^{58}Ni \rightarrow ^{66}As^{*}$ reaction at all $E_{c.m.}'s$ for quadrupole (β_{2i}) deformation and at ℓ_{max}=45$\hbar$. In DCM, LPs and IMFs correspond to $A_2 \leq 4$ and A_2=5-20, respectively.

S. No.	$E_{c.m.}$ (MeV)	ΔR (fm)	σ_{DCM} (mb)			Σ_{fusion}^{DCM} (mb)	$\sigma_{fusion}^{Expt.}$ (mb)
			LP	IMF	fission		
1	15.2±0.2	1.033	8.00	14.00	3.00	25.00	28.31.00±4
2	19.4±0.2	1.179	54.00	52.00	15.00	121.00	112.83±41
3	21.1±0.2	1.243	118.00	93.00	29.00	240.00	210.50±50
4	21.7±0.2	1.275	165.00	123.00	41.00	329.00	398.85±71
5	23.2±0.3	1.319	251.25	175.20	61.90	488.35	488.52±127
6	23.6±0.3	1.334	282.00	195.00	71.00	548.00	606.12±122
7	23.7±0.3	1.338	291.67	200.97	74.23	566.87	567.06±156
8	25.0±0.3	1.371	370.00	247.62	95.87	713.49	714.82±212
9	25.5±0.3	1.390	426.00	282.00	111.00	819.00	864.67±154

in the decay of $^{66}As^{*}$ is clearly observed from Fig. 6.1(a,b). The role of spherical versus deformed configurations and the characteristic behavior of the fragmentation potential for LPs and IMFs at lower versus higher ℓ values are better illustrated in terms of the preformation probability P_0 (A_i; i=1, 2), which is plotted in Fig. 6.1(c,d). At minimum ℓ, i.e., at ℓ=0$\hbar$, the contribution of LPs is dominant, whereas at maximum ℓ, i.e., at ℓ_{max}, the contribution of IMFs and fission fragments is greater. In other words, at lower ℓ values the LP decay channel dominates, whereas IMFs and fission fragments start appearing at higher ℓ values. Thus, LPs, IMFs and fission fragments compete with each other in the decay of $^{66}As^{*}$.

An explicit representation of the results obtained from these calculations (for β_2 deformation) is given in Table 6.1, where the calculated cross sections of the different processes (LPs, IMFs and fission fragments) are presented along with ΔR and the experimental

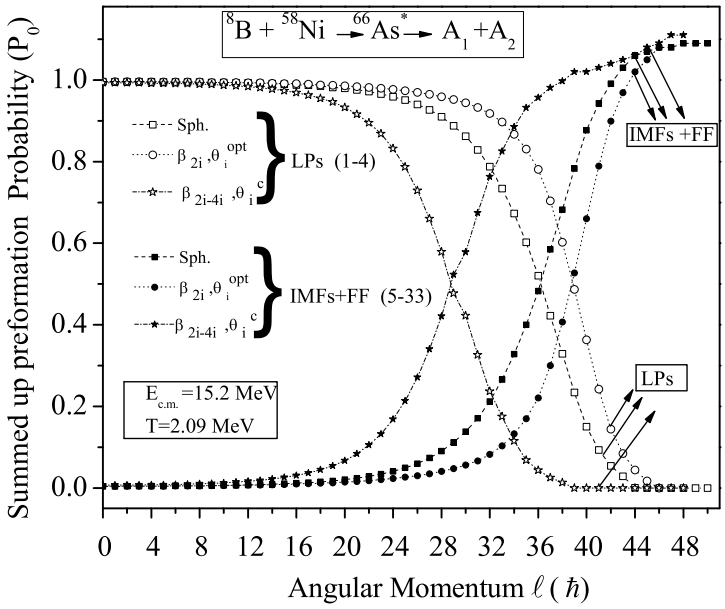

Figure 6.2 Effect of deformations on the variation of the summed-up preformation probability P_0 for LPs and for IMFs + fission fragments at $E_{c.m.}$=15.2 MeV.

data [7]. It is clear from Table 6.1 that the contribution of fission fragments is much less than those of LPs and IMFs. At below-barrier energy, IMFs dominate, whereas at above-barrier energies, LPs are the major contributors. Fission fragments contribute the least at both below and above-barrier energies. However, the fission fragments start dominating for (β_{2i}-β_{4i})-deformed fragmentation, which has a contribution of 5.98 mb for LPs, 9.26 mb for IMFs and 13.5 mb for fission fragments at below barrier energy ($E_{c.m.}$=15.2 MeV). Meanwhile, at higher energies, the contributions increase to 323.67 mb for LPs, 314.90 mb for IMFs and 227.50 mb for fission fragments at $E_{c.m.}$=25.5 MeV. Additionally, for spherical fragmentation, the contribution of LPs remains the maximum at both below and above-barrier energies. The relative contributions of LPs, IMFs and fission fragments for spherical approach are 15.4 mb,9.07 mb and 3.28 mb, respectively, at $E_{c.m.}$=15.2 MeV and 408.78 mb, 241.26 mb and 216.26 mb at $E_{c.m.}$=25.5 MeV.

The variations of LPs, IMFs and fission fragments as a function of angular momentum

and the effect of deformations on the summed-up preformation probability (P_0) is shown in Fig. 6.2. The behavior of the summed-up preformation probability (P_0) for LPs and for IMF + fission fragments does not change significantly for a large range of angular momentum values. However, after a certain limit, a fine shift in the variation of P_0 can be seen. For β_{2i}-deformed fragmentation, at below-barrier energy (at 15.2 MeV), the summed-up preformation probability (P_0) is minimum for IMF + fission and maximum, i.e., $P_0 \approx 1$, for LPs up to ℓ=30$\hbar$. However, this trend is no longer followed for ℓ>30$\hbar$. The contribution of LPs then drops until the ℓ_{max} value of 45$\hbar$ is reached. In contrast, the P_0 for IMF + fission fragments shows a rising trend for all values above 30$\hbar$. A similar trend is observed for spherical and hexadecapole-deformed fragmentation, but the shift in profile of preformation factor occurs at a comparatively lower angular momentum. It is observed that at a certain ℓ value (which is ℓ=28$\hbar$ for hexadecapole deformations, ℓ=36$\hbar$ for spherical choice of fragmentation and ℓ=38$\hbar$ for quadrupole deformations), LPs and IMFs + fission fragments have the same $P_0 \simeq 0.5$. The LP contribution to the summed-up P_0 is maximum at lower angular momentum, whereas the contribution of IMFs + fission fragments is larger at higher angular momentum for all three choices of fragmentation. It is relevant to mention that the general behavior of preformation probability as a function of angular momentum does not change with an increase in excitation energy. However, at higher energies (for example, $E_{c.m.}$=25.5 MeV), the change in preformation is observed at lower angular momentum of ℓ=22$\hbar$ for quadrupole deformations, ℓ=18$\hbar$ for spherical fragmentation and ℓ=15$\hbar$ for hexadecapole-deformed fragmentation. Hence, it can be concluded that the fragmentation potential and preformation probability of the decaying fragments is influenced by the inclusion of deformation effects.

For β_{2i} deformation, the cross sections obtained for the decay of ^{66}As* nucleus formed in the ^{8}B+^{58}Ni reaction for different decay modes, i.e., LPs, IMFs and fission fragments

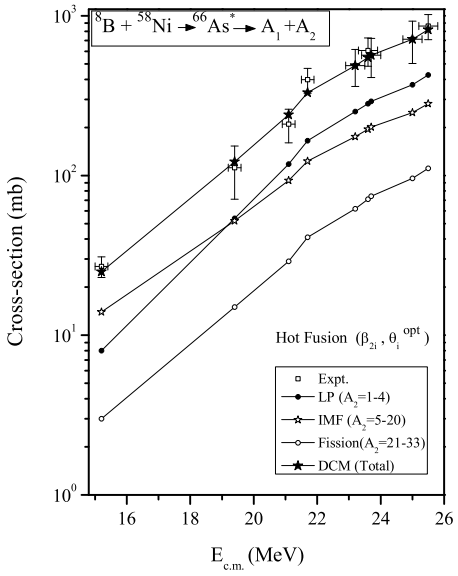

Figure 6.3 Comparison of the fusion excitation function calculated using the DCM (where σ_{fusion}=σ_{LP}+σ_{IMF}+$\sigma_{fission}$) to the experimental data [7] for the decay of ^{66}As* formed in the ^{8}B+^{58}Ni reaction.

at different $E_{c.m.}$ values and their sum, i.e., the total fusion excitation function σ_{fusion}^{cal}, are plotted in Fig. 6.3 and are also tabulated in Table 6.1. The corresponding ΔR values are depicted later in Fig. 6.4(c). It is clear from Fig. 6.3 that the contribution from LPs is the highest, followed by IMFs and fission fragments at near and above-barrier energies. Interestingly, at below-barrier energy ($E_{c.m.}$=15.2 MeV), IMFs dominate over LPs, whereas fission fragments are still the weakest contributor towards the fusion cross sections. This enhanced IMF contribution at below-barrier energies calls for experimental verification. Fission fragments contribute approximately ∼15% of the total fusion cross sections.

The inbuilt barrier lowering property [17] of DCM is included via the neck-length parameter ΔR. Fig. 6.4(a) shows the variation of the barrier-lowering parameter ΔV_B as a function of $E_{c.m.}$ for individual decay fragments i.e LPs, IMFs, and fission fragments at ℓ=ℓ_{max}. It should be noted that ΔV_B is negative and non-zero for all three components, which indicates that the barrier lowering is essential and inbuilt in DCM. The magnitude

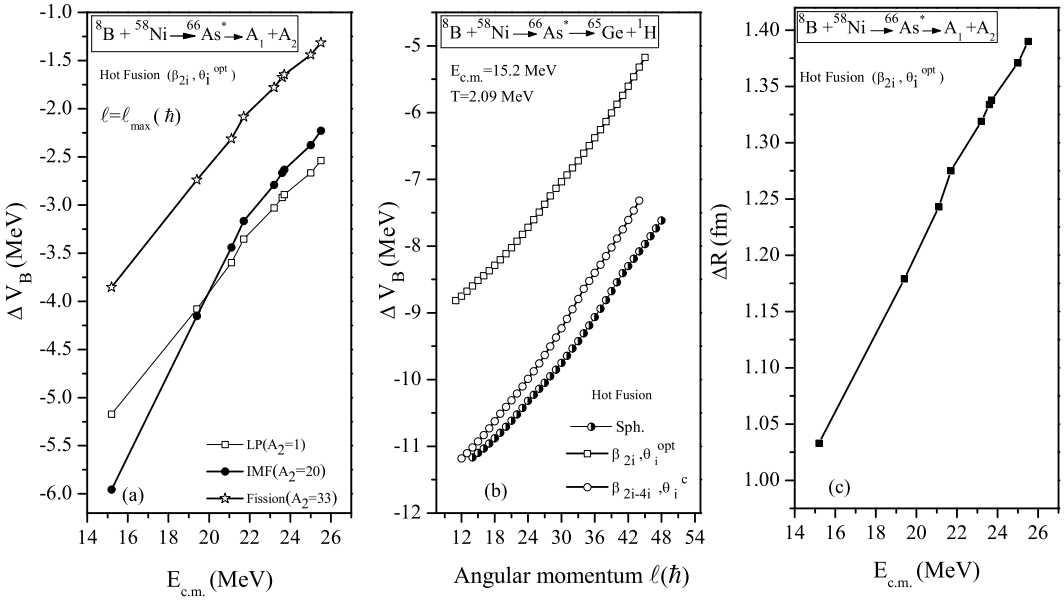

Figure 6.4(a) Variation of the barrier-lowering parameter ΔV_B as a function of $E_{c.m.}$ for the ℓ=ℓ_{max} case . (b) ΔV_B as a function of angular momentum ℓ ($\hbar$). (c) The best-fit neck-length parameter ΔR as a function of $E_{c.m.}$.

of ΔV_B is minimum for each decay mode at highest energy and increases as the energy decreases. The barrier-lowering ΔV_B is almost comparable for LPs and IMFs, whereas it is of relatively lesser magnitude for fission. As Fig. 6.4(a) deals with an explicit ℓ value, an equivalent variation of ΔV_B as a function of ℓ, at $E_{c.m.}$=15.2 MeV is shown in Fig. 6.4(b) for the ^{8}B+^{58}Ni→^{66}As*→^{65}Ge+ ^{1}H decay channel with spherical, β_{2i}-deformed and up to β_{2i-4i} deformed fragmentation. The magnitude of ΔV_B is maximum for the spherical case and decreases from the β_{2i-4i} to β_{2i} approach. Fig. 6.4(c) shows the neck-length parameter ΔR, which controls the barrier-lowering parameter ΔV_B, shown in Fig 6.4 (a) and (b). It is worth mentioning that in the experiment carried out by [7] the radius of p-halo nucleus is taken to be 26 % larger than the normal radius. To compensate for the increased radius of the halo nucleus, the neck-length parameter ΔR used in DCM calculations adjusts itself such that it absorbs the extended radius. The value of ΔR for spherical and β_{2i-4i}-deformed cases are comparable to each other, whereas it is relatively higher in

Table 6.2 Cross sections for the ^{8}B+^{58}Ni→^{66}As* reaction at extrapolated $E_{c.m.}$ for quadrupole (β_{2i}) deformation.

S. No.	$E_{c.m.}$	DCM					
		ΔR	ℓ_{max}	σ_{LP}	σ_{IMF}	$\sigma_{fission}$	σ_{fusion}
	(MeV)	(fm)	($\hbar$)	(mb)	(mb)	(mb)	(mb)
1	27.0	1.417	45	488.84	319.35	129.59	937.78
2	28.5	1.437	45	536.57	344.66	140.00	1021.23
3	30.0	1.448	45	536.21	339.94	142.40	1018.55

magnitude for the β_{2i}-deformation effect with the optimum orientation approach. This result indicates that the fragmentation is more prompt with β_{2i} deformation compared with the spherical and β_{2i-4i} deformed cases.

Experimentally, it was observed that fusion cross sections for ^{8}B+^{58}Ni→^{66}As* are enhanced with respect to normal systems in this energy range. This observation is also supported by the use of neck-length parameter ΔR in DCM calculations. At the touching configuration, i.e., with ΔR=0, the cross sections are small in comparison to the observed fusion cross sections, but as the value of neck-length parameter ΔR is increased, the calculated cross sections find nice agreement with the experimental data. This result leads to the realization that because of the increased size of the p-halo ^{8}B nucleus, the cross sections are larger compared to normal nuclei, and this enlarged size of the ^{8}B nucleus is suitably absorbed into the DCM through its neck-length parameter ΔR. Therefore, DCM based calculations could nicely address for these enhanced cross sections.

In addition to this, an estimation of cross sections at higher energies i.e, $E_{c.m.}$=27 MeV, 28.5 MeV and 30 MeV is done for β_{2i} deformation. Following the trend at available energies, the cross sections at higher energies is estimated at neck-length parameter ΔR obtained via polynomial fitting of the ΔR values given in Table 6.1, and is shown in Fig. 6.5. The table 6.2 shows the values of ΔR, ℓ_{max} and the cross sections estimated

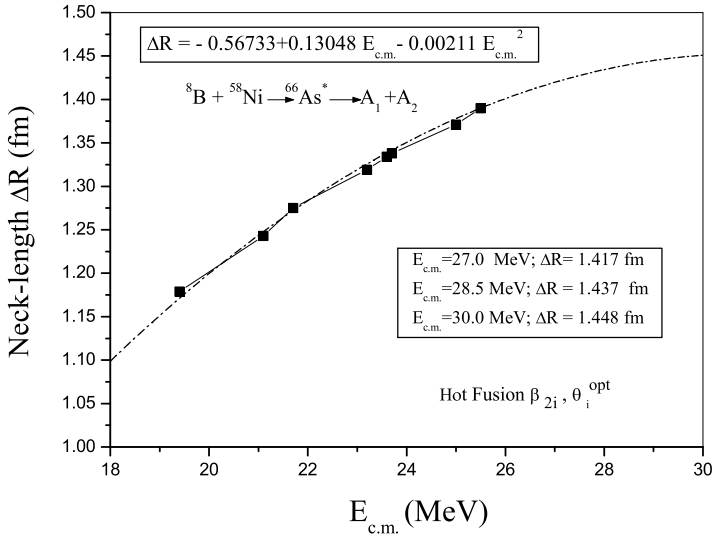

Figure 6.5 The best-fit neck-length parameter ΔR as a function of $E_{c.m.}$. The extrapolated energies and the corresponding values of ΔR are shown for quadrupole (β_{2i}) deformation.

using DCM, which can further be verified by performing experiments at these higher energies. It is observed that LPs are still the major contributors at all energies at which the cross-sections are predicted.

Apart from studying the role of deformations and the cross-sections of decay fragments contributing towards ^{66}As* nucleus, the application of DCM is further extended to much lighter even mass ^{40}Ca* and odd mass ^{39}K* nuclei to check the consistency of results obtained through collective clusterization method applied to relatively heavier nuclei. In addition to this, the fragment masses corresponding to the measured fragment charge are identified for the decay of these nuclei. Besides this, an application to Deep Inelastic Collision (DIC) process is also studied for ^{40}Ca* and ^{39}K* nuclei. The details of this study are presented in the following section.

6.3 Fragment mass identification and related aspects in the decay of $^{40}Ca^*$ and $^{39}K^*$ nuclei

In the results discussed above it has been observed that for light mass nuclei, the light charged particles [LPs, also called evaporation residues; $A \leq 4$ and $Z \leq 2$] form the dominant decay mode accompanied with small contribution of intermediate mass fragments, also termed as complex mass fragments. However, apart from the CN contribution, the cross-sections for such nuclei may also involve contribution from certain non-compound nucleus (nCN) process such as deep inelastic collisions (DIC) [18], where projectile and target nuclei stick together leading to a composite system with interaction time small enough for the formation of a compound nucleus (CN). The presence of DIC may be attributed to large angular momentum, exceeding the critical value (ℓ_{crit}) for which the partial waves can not be trapped [19] and hence inhibit the formation of CN. However, for lighter systems the individual contribution of CN and nCN processes (DIC here) could not be distinctly separated due to the involvement of relatively smaller mass. Thus, the study of decay patterns observed in light mass nuclei is of considerable interest and the same is investigated in this section, for $^{40}Ca^*$ and $^{39}K^*$ nuclei formed in asymmetric reactions. Although, the complex fragments with $Z \geq 6$ emitted in the decay of $^{40}Ca^*$ system have been studied in various experiments [20], the emission of much lighter fragments, $3 \leq Z \leq 5$ have been observed recently for both $^{40}Ca^*$ and $^{39}K^*$ nuclei [21] and the same is tested using the dynamical cluster-decay model (DCM) [8–16]. It is worth mentioning that so far all the calculations have been carried out in reference to the mass measurement, however, the following study takes into account the measured charge distribution of decaying fragments. The dynamical cluster-decay model (DCM) [8–16], based on the QMFT adequately identifies the most favorable fragment mass(es) corresponding to a given fragment

charge (Z) and thus provides a complete description of the decay mechanism involved in the dynamics of considered nuclear systems.

In reference to the experimentally measured charge cross-sections for Z=3,4 and 5 the contribution of corresponding fragment masses for the neutron-magic (N=20) $^{40}Ca^{*}$ nucleus and odd-mass $^{39}K^{*}$ nucleus formed at same excitation energy, E^{*}_{CN}=66.5 MeV (equivalently T=4.0MeV), have been calculated in framework of DCM by considering spherical choice of fragmentation. Interestingly, the neutron magic $^{39}K^{*}$ nucleus, formed in $^{11}B+^{28}Si$ and $^{12}C+^{27}Al$ reaction provides an opportunity to explore the possible effect of entrance channel. Thus, the work presented in this chapter aims at (i) identifying the fragment masses corresponding to a given fragment charge and subsequently accessing their respective contribution towards the cross-sections for both the CN as well as nCN processes. (ii) investigating the effect of entrance channel for the $^{39}K^{*}$ nucleus formed using ^{11}B and ^{12}C beams. The behavior of fragmentation potential, preformation probability (P_0) and penetrability (P) is analyzed to look for the nuclear structure effects and to explore the dynamics of the chosen reactions. Also, the role of angular momentum along with preformation probability P_0 is investigated to account for different decay processes observed through CN and nCN channel. It is worth mentioning that for the CN process, the complex fragment cross-sections have been fitted for lower ℓ-values upto ℓ=ℓ_{crit} (27 $\hbar$). However, for the partial waves above ℓ_{crit}, the CN formation is hindered giving rise to the nCN (DIC) process. Thus, for the fragments observed through DIC, the contribution of ℓ-values lying between ℓ_{crit} <$\ell \leq \ell_{max}$ has been considered.

Fig.6.6 shows the variation of fragmentation potential V(MeV) minimized in mass co-ordinate η_A for the CN decay of $^{40}Ca^{*}$ and $^{39}K^{*}$ systems at extreme values of angular momentum, ℓ=0$\hbar$ and ℓ=ℓ_{crit} (27$\hbar$). The behavior of complex fragments corresponding to CN decay is denoted as fusion-fission (FF) fragments. From the figure it is observed

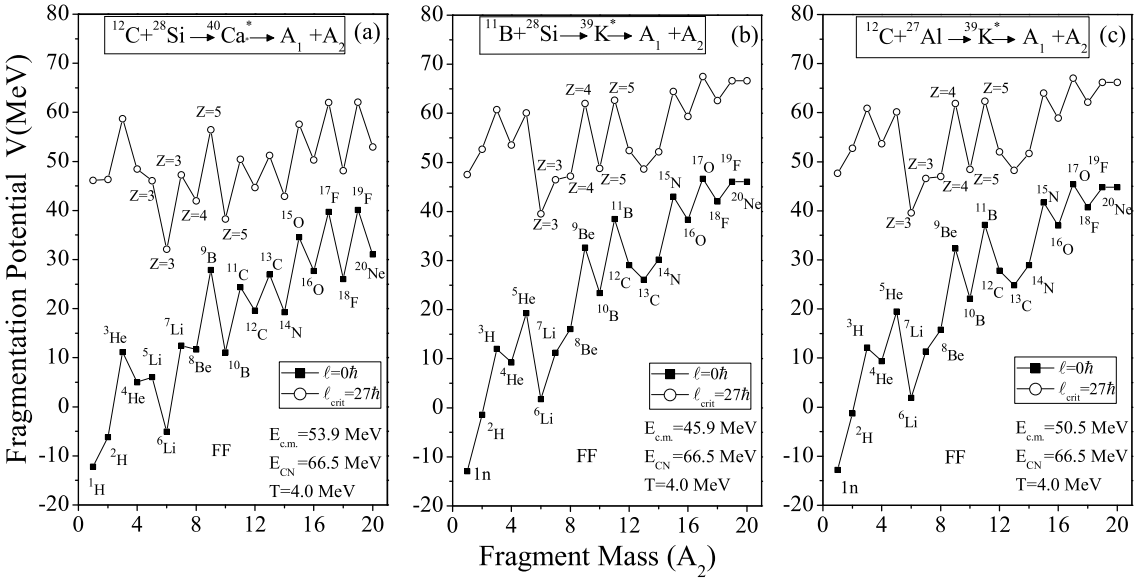

Figure 6.6 Variation of fragmentation potential V (MeV) as a function of fragment mass A_2 for the fusion-fission (FF) fragments observed in (a) $^{12}C+^{28}Si\rightarrow^{40}Ca^*$ (b)$^{11}B+^{28}Si\rightarrow^{39}K^*$ (c) $^{12}C+^{27}Al\rightarrow^{39}K^*$ reactions.

that overall structure of potential energy surfaces (PES) remain similar at extreme values of angular momentum for both the systems at ℓ=0$\hbar$ and at ℓ=ℓ_{max}. However, the characteristic behavior of the LPs and the FF fragments change on going from ℓ=0$\hbar$ to ℓ_{crit}. At ℓ=0$\hbar$, the magnitude of fragmentation potential is least for the LPs and relatively higher for the FF fragments whereas, at ℓ_{crit} the even-mass fragments corresponding to Z=3,4 and 5 attain the lower potential compared to LPs. In terms of DCM calculations, lower fragmentation corresponds to higher preformation probability and hence corresponds to relatively more favorable decay. Thus, the even fragments corresponding to measured charge form the favorable decay mode at higher ℓ-values. A careful investigation of Fig.6.6 reveals that fragmentation potential is different for the decay of $^{40}Ca^*$ and $^{39}K^*$ nuclei [compare Fig.6.6(a) with Fig.6.6(b)] but is identical for $^{39}K^*$ system formed through two different entrance channels, $^{11}B+^{28}Si$ and $^{12}C+^{27}Al$ [compare Fig.6.6(b) with Fig.6.6(c)]. Thus it may be concluded that the PES vary with mass of compound nucleus formed but

Table 6.3 The FF cross sections calculated using DCM with spherical fragmentation for the decay of ^{40}Ca* nucleus formed in ^{12}C+^{28}Si reaction and for ^{39}K* nucleus formed through ^{11}B+^{28}Si, ^{12}C+^{27}Al channels at $E_{CN}{}^*$=66.5MeV, compared with experimental data Also shown are the best fitted ΔR values and fragments contributing towards Z=3,4 and 5. The cross-sections have been calculated upto ℓ_{crit}=27$\hbar$.

Z=3			Z=4			Z=5		
ΔR	σ_{DCM}	$\sigma_{Expt.}$	ΔR	σ_{DCM}	$\sigma_{Expt.}$	ΔR	σ_{DCM}	$\sigma_{Expt.}$
(fm)	(mb)	(mb)	(fm)	(mb)	(mb)	(fm)	(mb)	(mb)
			^{12}C+^{28}Si→^{40}Ca$^* \rightarrow A_1 + A_2$					
	A_2=5+6+7			A_2=8			A_2=9+10	
1.04	3.41	$3.7\pm^{5.4}_{1.7}$	1.47	2.53	$2.7\pm^{4.1}_{1.2}$	1.49	3.38	$3.4\pm^{5.1}_{1.5}$
			^{11}B+^{28}Si→^{39}K$^* \rightarrow A_1 + A_2$					
	A_2=6+7			A_2=8+9			A_2=10+11	
1.12	9.80	$8.5\pm^{10.0}_{5.8}$	1.48	6.19	$5.3\pm^{8.0}_{2.3}$	2.00	19.15	$21\pm^{32.1}_{9.2}$
			^{12}C+^{27}Al→^{39}K$^* \rightarrow A_1 + A_2$					
	A_2=6+7			A_2=8+9			A_2=10+11	
1.14	9.48	$8.5\pm^{10.6}_{6.2}$	1.46	4.86	$4.2\pm^{5.8}_{3.0}$	1.81	10.77	$9.0\pm^{13.0}_{5.2}$

are independent of the entrance channel effect. Comparing Fig.6.6(a) with Fig.6.6 (b) and (c) one may observe that structure effects are more prominent in the doubly magic ^{40}Ca* nucleus as compared to the odd mass ^{39}K* nucleus particularly in symmetric fission region. The individual fragments emitted in the decay of both the systems under study have been identified and marked in Fig.6.6. For ^{40}Ca*, the fragment masses contributing towards the FF cross section corresponding to Z=3 are ^{5,6,7}Li, Z=4 is ^{8}Be while for Z=5 the isotopes ^{9,10}B contribute. On the other hand the contributing fragments change for the decay of ^{39}K*, being ^{6,7}Li for Z=3, ^{8,9}Be for Z=4 and ^{10,11}B for Z=5.

Using DCM approach, the available cross-sections for the complex fragments have been fitted simultaneously by using the neck-length parameter ΔR. The ΔR values used for the decay of both nuclei and the cross-sections calculated for each Z along with contributing isotopes, compared with the experimental data are tabulated in Table 6.3. It must be noted that neck-length parameter ΔR used for ^{11}B+^{28}Si and ^{12}C+^{27}Al reaction forming

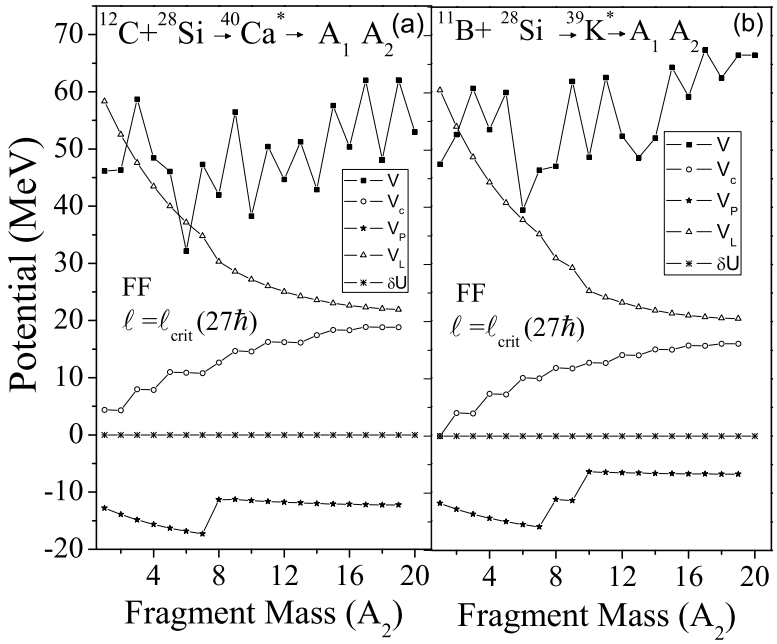

Figure 6.7 Variation of individual potentials and their sum, the total fragmentation potential plotted as function of fragment mass A_2 for (a) ^{12}C+^{28}Si and (b) ^{11}B+^{28}Si reactions at ℓ=ℓ_{crit}.

^{39}K* nucleus are quite similar, further indicating that entrance channel effects are absent in these reactions. On the contrary, ΔR is much lower for doubly magic nucleus ^{40}Ca*.

Further to explore the effect of each potential contributing towards the fragmentation structure [potential $V_R(\eta, T)$ (shown in Eq.(2.14)], the individual variation of V_ℓ,V_C, V_P, shell corrections (δU) and their sum is plotted as a function of fragment mass (A_2) for ^{40}Ca* and ^{39}K* systems as shown in Fig.6.7. It may be noted that behavior of ^{40}Ca* nucleus is shown in comparison to ^{39}K* system formed though ^{11}B+^{28}Si channel only, since the structure of odd-mass nucleus ^{39}K* is identical for both the reactions. The angular momentum (ℓ) forms an important ingredient in the DCM based calculations. In general, the results obtained involve the effect of ℓ-values upto ℓ=ℓ_{max}. However in the present work, an attempt is made to limit the CN contribution upto ℓ=ℓ_{crit} while higher ℓ-values upto ℓ=ℓ_{max} are implied to calculate the DIC contribution. The centrifugal potential (V_ℓ) given by Eq.(2.38) provides magnitude to the total potential V (MeV) and

is found to vary inversely with fragment mass A_2. Further, the effect of fragment charge and hence mass is contained in the Coulomb potential (V_C) given by Eq. (2.20) which increases with increase in mass (A_2). The structure in the total fragmentation potential may be attributed to variations present in V_C which get enhanced in magnitude under the influence of centrifugal and proximity potential. It is well known that the shell effects start vanishing at T>2.0 MeV, and the same is also witnessed in the present case where $\delta U \sim 0$ for both the light nuclei formed at T=4.0 MeV. The presence of odd-Z, non-α fragments at the minima signifies that due to the absence of shell-effects, no α-cluster structure is observed in the decay of $^{40}Ca^*$ and $^{39}K^*$ nuclei. Apart from these contributors, the attractive nuclear proximity potential (V_P) given by Eq. (2.26) also plays crucial role in the total potential. The effect of neck length parameter ΔR is clearly evident from the behavior of V_P. For $^{40}Ca^*$ nucleus it decreases with increase in fragment mass upto A_2=7 (Z=3) after which a sudden rise is observed for A_2=8 (Z=4). This is mainly due to different ΔR involved in the calculations for Z=3 and Z=4 (as mentioned in Table 6.3). However, ΔR for Z=5 is similar to Z=4, due to which the trend of V_P for A_2=9,10 is similar to A_2=8 and remains almost constant thereafter. Whereas, for $^{39}K^*$ system, the ΔR values are considerably different for Z=3,4 and 5 as a result of which a sharp increase is observed at A_2=8,9 (Z=4) and at A_2=10,11 (Z=5) and eventually becomes constant for A_2>11.

The characteristics of the energetically favored fragments corresponding to Z=3,4 and 5 are explored further through the preformation probability (P_0) plotted for the decay of $^{40}Ca^*$ and $^{39}K^*$ systems formed in respective entrance channels as shown in Fig.6.8. At extreme ℓ-values an asymmetric variation is observed for both the systems. However, the contribution of symmetric fragments show upward trend with increase in ℓ-value. At higher angular momentum, the complex fragments varying from A_2=5-10 for $^{40}Ca^*$ and

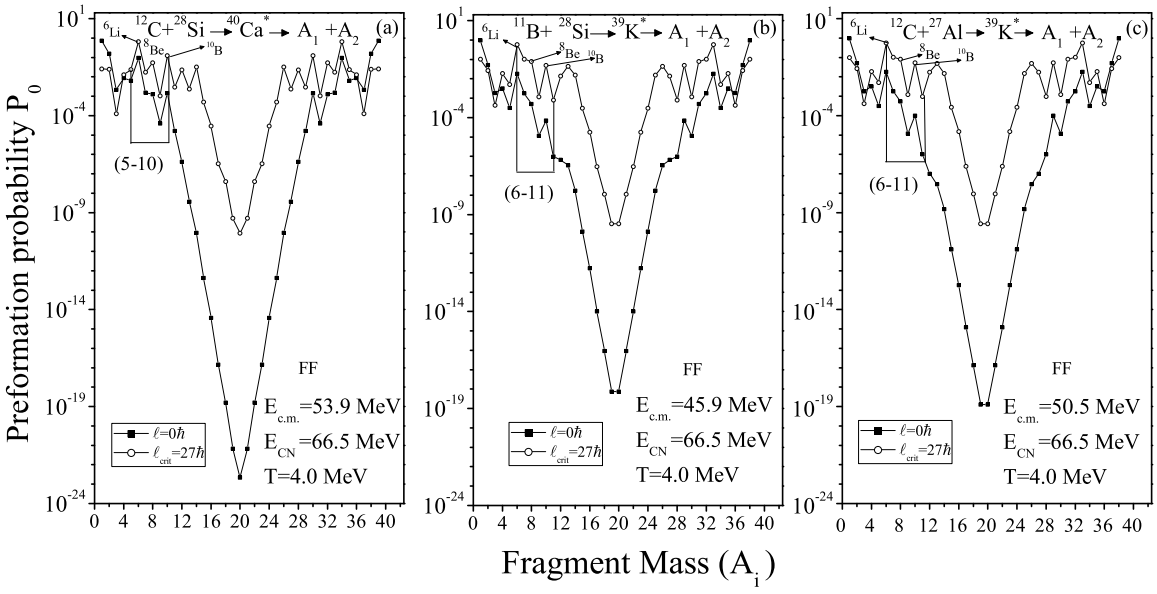

Figure 6.8 Preformation probability P_0 as a function of fragment mass (A_i) for the decay of ^{40}Ca* and ^{39}K* systems plotted for ℓ=0$\hbar$ and ℓ=ℓ_{crit} for spherical choice of fragmentation.

A_2=6-11 for ^{39}K* nucleus show maximum preformation probability as compared to other fragments. This enhanced probability justifies the emergence of such complex fragments as compared to LPs at higher ℓ values. The mass distribution is almost identical at extreme ℓ values, except for A_2=11-14 for ^{40}Ca* and A_2=12-14 for ^{39}K* system. However, a closer look at Fig.6.8(a) suggests that in addition to the experimentally observed Z=3,4 and 5, the fragments ^{11,12,13}C and ^{14}N with considerably large (P_0) might also contribute towards the decay of ^{40}Ca* systems. Similarly ^{12,13}C and ^{14}N seem equally favorable in the decay of ^{39}K* as evident in Fig.6.8 (b,c). The cross-sections predicted for these higher charges (Z=6,7), using ΔR values same as that of Z=5 are tabulated in Table 6.4. Thus, in framework of DCM, the experimental charge cross-section have been fitted with the identified fragments along with the estimation of higher Z contribution towards the decay of even and odd mass nuclei under study. Among all the identified fragments, ^{6}Li, ^{8}Be and ^{10}B may form the most favorable decay choices in context of their larger preformation

Table 6.4 The DCM estimated cross-sections for light particles ($A_2 \leq 4$) and higher Z (=6,7) fragments using spherical choice of fragmentation for the decay of $^{40}Ca^*$ and $^{39}K^*$ nucleus formed through both the entrance channels, along with the corresponding ΔR values.

S.No.	ΔR	σ_{DCM}		
		LP	Z=6	Z=7
	(fm)	(mb)	(mb)	(mb)
	$^{12}C+^{28}Si \rightarrow ^{40}Ca^* \rightarrow A_1 + A_2$			
1	1.49	69.30	0.45	0.31
	$^{11}B+^{28}Si \rightarrow ^{39}K^* \rightarrow A_1 + A_2$			
2	2.00	777.00	16.47	3.70
	$^{12}C+^{27}Al \rightarrow ^{39}K^* \rightarrow A_1 + A_2$			
3	1.81	457.40	8.33	1.88

factor. This observation supports the presence of deeper minima corresponding to these fragments as observed in Fig.6.6. Moreover, the mass distribution for $^{39}K^*$ nucleus being almost identical for $^{11}B+^{28}Si$ and $^{12}C+^{27}Al$ reactions further justifies the entrance channel independence. As mentioned earlier, in the light mass region such as the one under study, the light particles [(LPs; $A_2 \leq 4$)] form the dominant decay mode with relatively smaller time of emission in comparison to fission fragments. In the framework of DCM, the neck-length parameter gives a measure of time, with large ΔR indicating a small time scale. Thus, the LP cross sections were estimated by taking highest ΔR among the best fit values obtained for the fitted FF cross-sections corresponding to Z=3,4 and 5 and are tabulated in Table 6.4. Interestingly, the structure and mass distribution of both the light nuclear systems studied here is consistent with the earlier results of $^{48}Cr^*$ [22] and $^{56}Ni^*$ [23] nuclei.

In addition to P_0, the cross-sections in DCM depend upon penetrability P [see Eq. (2.50)], thus one also needs to explore its behavior in order to understand the dynamics of a reaction completely. In Fig.6.9 (a,b) penetrability is plotted as a function of angular

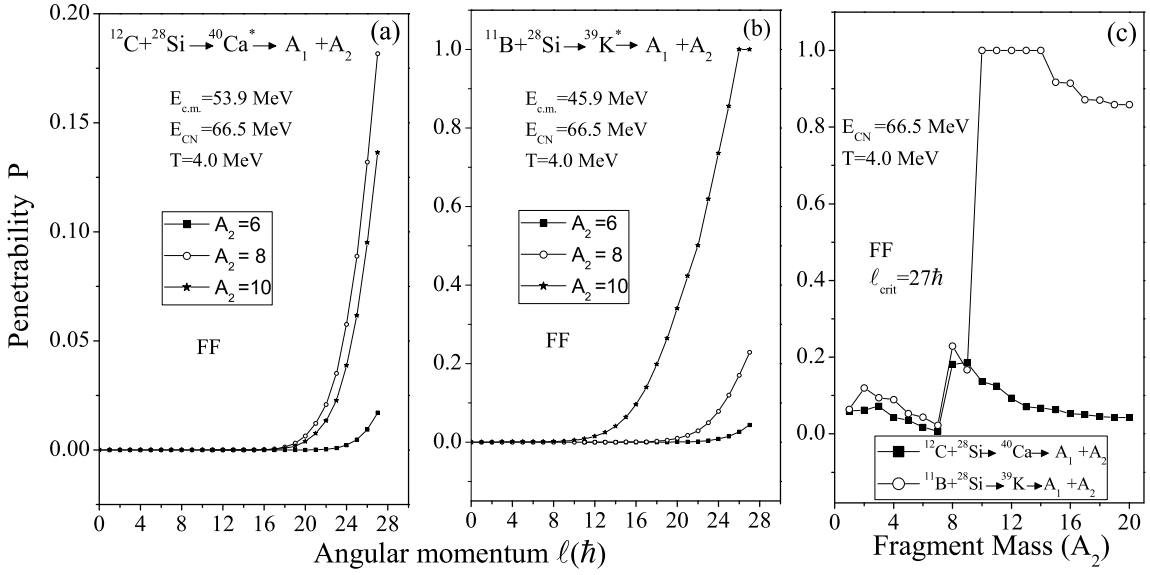

Figure 6.9 Penetrability P plotted as function of angular momentum for the emission of ^{6}Li, ^{8}Be and ^{10}B fragments for the (a) ^{12}C+^{28}Si and (b)^{11}B+^{28}Si reaction. (c) P as a function of fragment mass (A_2) for the decay of ^{40}Ca* and ^{39}K* systems.

momentum (ℓ) for the highly preformed FF fragments ^{6}Li, ^{8}Be and ^{10}B emitted in the decay of ^{40}Ca* and ^{39}K* systems. From Fig.6.9 (a) it is observed that for ^{40}Ca* nucleus, the penetrability remains negligible upto ℓ=22$\hbar$ for ^{6}Li and upto ℓ=17$\hbar$ for ^{8}Be and ^{10}B. However, it changes significantly with increase in ℓ above ℓ>22$\hbar$ and 17$\hbar$ being maximum for ^{8}Be followed by ^{10}B and minimum for ^{6}Li. On the other hand, for ^{39}K* nucleus, the P starts contributing from ℓ>20$\hbar$ for ^{6}Li and ^{8}Be, while for ^{10}B it contributes from relatively lower ℓ ($>$ 12$\hbar$).

Fig.6.10 shows the variation of barrier lowering parameter ΔV_B as a function of angular momentum ℓ for the ^{40}Ca* and ^{39}K* nuclei. Owing to the entrance channel independence, the barrier modification for ^{12}C+^{27}Al channel is similar to that of ^{11}B+^{28}Si channel and thus is not illustrated in the figure. It may be noted that, barrier modification [defined in Eq.(2.57)] is an in-built property of DCM, that enters through the neck-length parameter ΔR. It is negative and nonzero for all the three most probable decaying fragments which

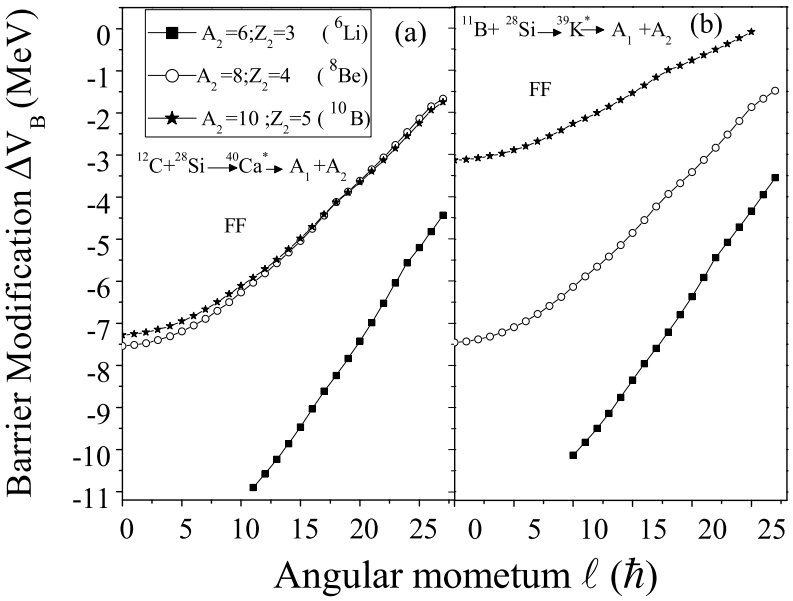

Figure 6.10 Variation of barrier lowering parameter ΔV_B as a function of angular momentum ℓ, plotted for the most probable fragments contributing towards (a)^{40}Ca* and (b) ^{39}K* nuclei.

indicates that barrier lowering is essential in DCM. Evidently, barrier modification is maximum in magnitude at lower ℓ-values and decreases with increase in angular momentum for both the systems.

This suggests that at lower ℓ, large barrier modification is required as compared to higher ℓ-values. It is observed that at a given ℓ, magnitude of ΔV_B is large for A_2=6. However, for ^{40}Ca* system it is almost similar for A_2=8 and A_2=10 whereas different for both these fragments for the odd mass ^{39}K* nucleus, being higher for A_2=8 and least A_2=10. This difference in barrier modification observed in the ^{39}K* nucleus may be attributed to the different values of neck-length parameter used (ΔR=1.48 for A_2=8 and ΔR=2.0 for A_2=10) to fit the cross-section for these fragments which are almost similar (ΔR=1.47 for A_2=8 and ΔR=1.49 for A_2=10) for ^{40}Ca* system. Thus the large difference in ΔV_B for ^{8}Be and ^{10}B observed for ^{39}K* nucleus may be associated with relatively higher ΔR values for A_2=8 and A_2=10.

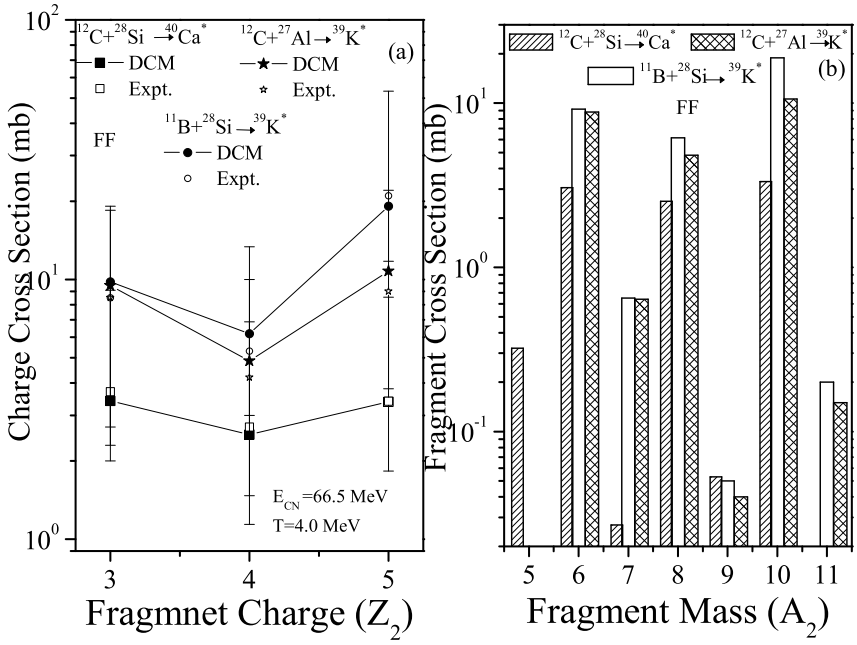

Figure 6.11(a) The DCM calculated cross-sections plotted as a function of fragment charge (Z=3,4,5) contributing towards the decay of $^{40}Ca^*$ and $^{39}K^*$ systems and its comparison with the experimental data. (b) Individual contributions for each fragment mass corresponding to a given charge obtained using DCM for both the light mass nuclei.

Fig.6.11(a) shows the comparison of experimental data [21] with DCM results as a function of fragment charge Z=3,4 and 5. It is observed that for all three charge fragments the cross sections obtained using DCM are in good agreement with experimental results (within error bars). Moreover, the individual contribution of the fragments identified using DCM corresponding to a given charge have also been calculated and are shown in Fig.6.11(b). Apparently, for a given Z, the cross sections for the even mass, Z=N nuclei are maximum compared to other fragments.

Apart from studying the decay of compound nucleus in form of complex fragments, we further aim at investigating the dynamics of non-compound nucleus (nCN) process in form of deep inelastic collision (DIC) observed for the light mass nuclei under consideration. It is worth mentioning that so far DCM has been successfully applied to study the decay of composite system formed via complete fusion, incomplete fusion and nCN

processes such as QF, however DIC is being addressed here for the first time. Based on

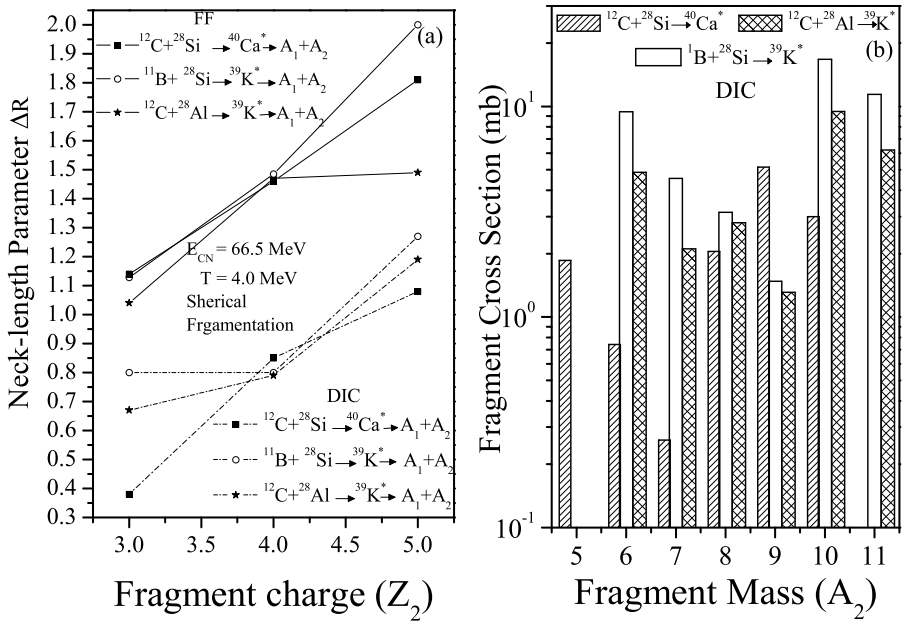

Figure 6.12(a) Variation of neck-length parameter as function of fragment charge for both the decay processes. (b) Individual contribution of the fragments contributing towards the decay of $^{40}Ca^{*}$ and $^{39}K^{*}$ systems through DIC process.

the characteristic features of DIC process, the DCM approach is modified in terms of angular momentum (ℓ) and Preformation probability P_0. For the CN process, observed at $\ell<\ell_{crit}$, the favorable decaying fragments penetrate through the potential barrier, while the same may not be the case for fragments obtained through DIC process. This is because at higher angular momentum, above ℓ_{crit}, projectile and target nuclei may not be trapped inside the potential barrier leading to hinderance of complete fusion and hence invoking the possibility of non-compound nucleus process. Thus DIC cross-sections have been calculated at ℓ-values varying from $\ell_{crit} <\ell\leq\ell_{max}$, i.e for 28$\hbar$-33$\hbar$, for which the equilibrated compound system is not formed. Another factor differentiating between CN and nCN processes is the preformation probability P_0, which is considered unity (P_0=1) for the projectile and target like fragments and is distributed equally among them. While

Table 6.5 The cross sections calculated for DIC fragments obtained using DCM with spherical fragmentation for the decay of $^{40}Ca^*$ nucleus formed in $^{12}C+^{28}Si$ reaction and for $^{39}K^*$ nucleus formed through $^{12}C+^{27}Al$, $^{11}B+^{28}Si$ channels at $E_{CN}{}^*$=66.5MeV, compared with experimental data. Also shown are the best fit ΔR values and fragments contributing towards Z=3,4 and 5. The cross-sections have been calculated for ℓ values varying from ℓ_{crit} (27$\hbar$)-ℓ_{max} (33$\hbar$).

Z=3			Z=4			Z=5		
ΔR	σ_{DCM}	$\sigma_{Expt.}$	ΔR	σ_{DCM}	$\sigma_{Expt.}$	ΔR	σ_{DCM}	$\sigma_{Expt.}$
(fm)	(mb)	(mb)	(fm)	(mb)	(mb)	(fm)	(mb)	(mb)
			$^{12}C+^{28}Si \rightarrow ^{40}Ca^* \rightarrow A_1 + A_2$					
	A_2=5+6+7			A_2=8			A_2=9+10	
0.38	2.9	$3.1\pm^{0.4}_{1.9}$	0.85	2.06	$2.0\pm^{1.3}_{1.3}$	1.08	8.16	$8.0\pm^{6.4}_{6.4}$
			$^{11}B+^{28}Si \rightarrow ^{39}K^* \rightarrow A_1 + A_2$					
	A_2=6+7			A_2=8+9			A_2=10+11	
0.8	14.0	$14.6\pm^{7.0}_{8.1}$	0.8	4.62	$4.7\pm^{3.4}_{3.4}$	1.27	28.2	$28.4\pm^{22.9}_{23.7}$
			$^{12}C+^{27}Al \rightarrow ^{39}K^* \rightarrow A_1 + A_2$					
	A_2=6+7			A_2=8+9			A_2=10+11	
0.67	7.0	$7.0\pm^{3.1}_{3.47}$	0.79	4.1	$4.2\pm^{2.2}_{2.3}$	1.19	15.6	$15.6\pm^{9.9}_{10.16}$

for the CN decay, P_0 is relatively distributed among all possible decay fragments.

Interestingly, for DIC the fragments emitted corresponding to a given charge are same as that of CN process, i.e ^{5,6,7}Li, ^{8}Be and ^{9,10}B contribute towards $^{40}Ca^*$ nucleus whereas, for $^{39}K^*$ nucleus ^{6,7}Li, ^{8,9}Be and ^{10,11}B are observed. In Table 6.5, the DIC contribution for $^{40}Ca^*$ and $^{39}K^*$ nuclei is tabulated along with isotopic mass and respective neck-length values. Also, Fig.6.12(a) shows the variation of only parameter of the model, neck-length parameter ΔR, obtained for the best-fit to the FF and DIC cross-sections as a function of fragment charge (Z_2). Also the individual cross-sections of the fragments contributing towards the decay of both the nuclei $^{40}Ca^*$ and $^{39}K^*$ through DIC process are shown in Fig.6.12(b). The contribution of a given fragment mass (A_2) is different for each charge (Z_2). It is observed that for $^{40}Ca^*$ nucleus, the contribution of fragments corresponding to Z=3 is maximum for A_2=5 and decreases with increase in mass, being minimum for A_2=7. However, for Z=4 and 5 for $^{40}Ca^*$ and Z=3,4,5 for $^{39}K^*$ system, the even fragments

show maximum contribution as observed earlier for the CN decay. The summary of these results is presented ahead in Sec. 6.4.

6.4 Summary

In this Chapter, the dynamics of the $^{8}B+^{58}Ni$ reaction is studied over a wide range of incident energies using the collective clusterization approach of DCM. Interestingly, LPs, IMFs and fission fragments all contribute significantly towards the decay of $^{66}As^{*}$ system. A deeper insight into the fragmentation paths reveals that at higher ℓ values the deformations (β_{2i} and β_{2i}-β_{4i}) play a significant role, whereas at ℓ=0$\hbar$, only hexadecapole effects influence the fission path. The role of deformations on the decay fragments is also analyzed with regard to the preformation probability (P_0), and the barrier modification ΔV_B. Also, the inclusion of deformations is shown to influence the relative contributions of the decay fragments. For the spherical fragmentation approach, at all reported energies, light-particle evaporation is dominant followed by IMF and fission decay. However, with the inclusion of quadrupole and hexadecapole-deformation effects, the IMF and fission fragments start dominating at the below-barrier region. The fusion excitation functions have been successfully obtained using the DCM at all energies, i.e., both above and below the Coulomb barrier, as a result of the model's inbuilt property of barrier modification. Moreover, the neck-length parameter (ΔR) accounts for the radius of the halo nuclei, and therefore no additional increment in the radius needs to be considered in DCM calculations. Besides this, estimation of the fusion cross sections at higher energies is also made using DCM which calls for experimental verification.

In addition to this, DCM is also applied to study the decay of light mass ^{40}Ca* and ^{39}K* nuclei. In framework of DCM, the fragment mass(es) contributing towards the CN and

nCN (DIC) processes are identified corresponding to the measured experimental charge distribution using spherical choice of fragmentation. It is observed that the complex fragments varying from A_2=5-10 for $^{40}Ca^*$ and A_2=6-11 for $^{39}K^*$ system corresponding to Z=3,4 and 5 contribute towards the cross-sections for both the decay processes. For a given Z, the fragments with Z=N are more probable among all the contributing isotopes. From the variation of fragmentation potential, preformation probability and penetrability, the entrance channel independence of $^{39}K^*$ nucleus is also investigated. Besides this, the cross-sections for the LPs and the higher Z fragments (Z=6,7) are estimated, with the former having larger cross-sections and being the dominant contributor. The CN cross-sections are attained successfully upto ℓ_{crit} for both the nuclei whereas, for the nCN process, only higher ℓ values lying between $\ell_{crit} < \ell \leq \ell_{max}$ are considered. As expected, CN cross-sections obtained for the fragments identified are larger for the even mass fragments for a given charge. The DCM based cross-sections obtained for CN and nCN (DIC) processes find nice agreement with the experimental data.

Converging here, this thesis presents a comprehensive picture of different decay processes observed in variety of nuclear systems formed in heavy ion reactions. The conclusions derived from this study are summarized in the next Chapter.

Bibliography

[1] G. Kaur, D. Jain, R. Kumar, and M. K. Sharma, Nucl. Phys. A **916**, 260 (2013).

[2] G. Kaur and M. K. Sharma, Int. Jour. of Mod. Phys. E **23**, 10 (2014).

[3] C. Signorini, Z.H. Liu, Z.C. Li, K.E.G. Lobner, L. Muller, M. Ruan, K. Rudolph, F. Soramel, C. Zotti, A. Andrighetto, L. Stroe, A. Vitturi, and H.Q. Zhang, Eur. Phys. J. A **5**, 7 (1999).

[4] R.Kumar and A.Bonaccorso Phys. Rev. C. **86**, 061601(R) (2012);R.Kumar and A.Bonaccorso, Phys. Rev. C. **84**, 014613 (2011).

[5] S. S. Chandel, S. K. Dhiman, and R. Shyam, Phys. Rev. C. **68**, 054320 (2003).

[6] Y. Kucuk and A. M. Moro, Phys. Rev. C. **86**, 034601 (2012);A.Bonaccorso *et al.,* Phys. Rev. C. **69**, 024615 (2004).

[7] E. F. Aguilera *et al.,* Phys. Rev. Lett. **107**, 092701 (2011).

[8] M. Kaur and M. K. Sharma, Phys. Rev. C **85**, 054605 (2012).

[9] G. Sawhney and M.K. Sharma, Eur. Phys. J. A **48** (2012).

[10] K. Sandhu, M. K. Sharma, A. Kaur, and R. K.Gupta, Phys. Rev. C **90**, 034610 (2014).

[11] M. Kaur and M. K. Sharma, Eur. Phys. J. A **50** (2014).

[12] G. Kaur, N. Grover, K. Sandhu, and M. K. Sharma, Nucl. Phys. A **927**, 232 (2014).

[13] M. K. Sharma and G. Kaur, Pramana Jour. of Phys. **82**, 919 (2014).

[14] M. Balasubramaniam, R. Kumar, R. K. Gupta, C. Beck, and W. Scheid, J. Phys. G : Nucl.Part. Phys. **29**, 2703 (2003).

[15] R. K. Gupta, M. Balasubramaniam , R. Kumar, N. Singh, M. Manhas, and W. Greiner, J. Phys.G : Nucl. Part. Phys. **31**, 631 (2005).

[16] R. K. Gupta, M. Manhas, and W. Greiner, Phys. Rev. C **73**, 054307 (2006).

[17] S. K. Arun, R. Kumar, and R. K. Gupta, J. Phys. G:Nucl. Part. Phys. **36**, 085105 (2009).

[18] A. Szanto de Toledo, B. V. Carlson, C. Beck, and M. Thoennessen, Phys. Rev. C **54**, 6 (1996) .

[19] N. Anyas-Weiss, J.C. Cornell, P.S. Fisher, P.N. Hudson, A. Menchaca-Rocha, D.J. Millener, A.D. Panagiotou, D.K. Scott, D. Strottman, D.M. Brink, B. Buck, P.J. Ellis, and T. Engeland, Phys Rep. (Section C of Physics Letters) **12**, 201 (1974).

[20] D. Shapira, D. Schull, J. L. C. Ford Jr., B. Shivakumar, R. L. Parks, R. A. Cecil, and S. T. Thornton, Phys. Rev. Lett. **53**, 1634 (1984).

[21] S. Kundu, C. Bhattacharya, K. Banerjee, T. K. Rana, et al., Phys. Rev. C **85**, 064607 (2012).

[22] B. B. Singh, M. K. Sharma, R. K. Gupta, and W. Greiner, Int. J. Mod. Phys E **15**, 699 (2006).

[23] R. K. Gupta, M. Balasubramaniam, R. Kumar, D. Singh, C. Beck, and W. Greiner, Phys. Rev. C **71**, 014601 (2005).

Chapter 7

Summary and outlook

In this thesis, the decay of various hot and rotating nuclear systems is studied to have a comprehensive picture of reaction dynamics associated with heavy ion reactions in low energy regime. The DCM formulated to study the decay of excited nucleus is adequately applied to explore the dynamics of nuclei in heavy, intermediate and light mass region. Using the collective clusterization approach of DCM, the decay of equilibrated compound nucleus (CN) formed via complete amalgamation of projectile and target nucleus is studied in form of evaporation residues (ER), intermediate mass fragments (also called complex fragments) and fission fragments. Moreover, for the reactions involving loosely bound nuclei as projectile, the decay of composite system formed through incomplete fusion (ICF) process is also studied. Besides this, the competing non-compound nucleus (nCN) processes such as quasi-fission (QF) and deep inelastic collision (DIC) are also explored in framework of DCM. In reference to all these decay processes, various aspects such as static and dynamic quadrupole deformation, hexadecapole deformation, orientation degree of freedom, barrier modification, shell closure effects, entrance channel effect, fission anisotropy and fine/sub-structure effects are studied. A general introduction related to an overview of importance of nuclear physics and hence nuclear reactions and description of

various decay processes related to this work is discussed in chapter 1. The methodology used, i.e the dynamical cluster-decay model (DCM) finds its basis in the well known quantum mechanical fragmentation theory (QMFT). In this pproach, the decay pattern of a nuclear system formed in heavy ion collisions is governed via the collective clusterization aspect. The detailed description of this methodology is given in chapter 2.

As a first application of DCM the decay of odd-mass ^{213,215,217}Fr* isotopes is studied in chapter 3. In this chapter, the prime focus is to carry out complete study of decay cross-sections (both ER and ff) and fission fragment anisotropies for ^{18}O+^{197}Au$\rightarrow^{215}$Fr* and ^{19}F+^{194,198}Pt$\rightarrow^{213,217}$Fr* reactions over a wide energy range, of $E_{c.m.}$ = 48-106 MeV. For ^{215}Fr* nucleus, the evaporation residue (ER) cross-sections are predicted using DCM by assuming that neck-length parameter 'ΔR' for ^{215}Fr* lies in between that for the ^{213}Fr* and ^{217}Fr* nuclei. Further, the fission and ER cross-sections of ^{213,217}Fr* nuclei are predicted at higher incident energies. It is observed that for both ^{213,217}Fr* isotopes, DCM based fission cross-sections σ_{fision} compare nicely with the experimental data and the predicted ER cross-sections σ_{ER} at the higher incident energies fit in to the systematics governed at relatively lower energies. The behavior of fission fragment anisotropy is also studied for ^{213,217}Fr* isotopes. The DCM calculated anisotropies for use of I_{NS} limit of moment of inertia show a nice agreement with the data. Due to the use of I_{NS} approximation the anisotropies are fitted at much smaller ℓ_{max} values, being consistent with the earlier result of ^{215}Fr*.This implies the fact that moment of inertia plays an important role regarding the dynamics involved in heavy-ion reactions. Besides this, a comparative analysis is made for the decay of ^{215}Fr* formed in ^{19}F+^{196}Pt and ^{18}O+^{197}Au reaction channels at a comparable excitation energy E^*_{CN} $\sim$47 MeV (T=1.429 MeV). It is observed that, the structure of fragmentation potential does not change much for the chosen extreme combinations. Also, the summed values of P_0 over ℓ are almost similar for both the reactions and the decay

barrier heights almost overlap each other at ℓ=ℓ_{max}. These observations suggest that the decay of ^{215}Fr* is almost independent of the choice of entrance channel. Apart from this, the ER as well as fission cross-sections are also predicted for ^{211,219}Fr* nuclei formed in proposed ^{19}F+^{192}Pt and ^{19}F+^{200}Pt reactions. It is observed that the contribution of ^{211,219}Fr* isotopes is rather small, compared to observed experimental data for ^{213,215,217}Fr* isotopes. Finally the role of shell closure effect in mass distribution is studied for the odd mass $^{211-219}$Fr* isotopes at a similar excitation energy $E^{*}_{CN}$$\sim$47 MeV. The shell effects in Fr isotopes arise due to the deformed closed shell around light-fragment charge Z_2=36 (actually at Z_2=35 and 37), and spherical shell closure around heavy-fragment charge Z_1=50 (actually at Z_1= 52 and 50). Thus it may be concluded that shell closure effect of the decay fragments play an important role in all the Fr isotopes under study. The DCM is also applied to study the role of orientation degree of freedom in context to superheavy ^{278,286}112* isotopes. For the use of hot (equatorial) compact orientation at above barrier energy, symmetric structure of fission fragments is observed whereas, at sub-barrier energy owing to the preferred cold (polar) elongated orientation the suppression in magnitude of symmetric fragments and dominance of asymmetric fragments is observed. Consequently, for the use of cold orientation, the DCM calculated fission cross-sections in sub-barrier region are over-estimated in comparison to the experimental data and signify the presence of quasi-fission contribution, which is more for neutron deficient ^{278}112* nucleus.

After exploring the dynamics of nuclei lying in heavy mass region by studying ER, fission, anisotropy, entrance channel and shell closure effect etc, the DCM is further applied to study the decay properties of intermediate mass ^{150,158}Tb* nuclei formed in ^{6}Li +^{144,152}Sm reactions in chapter 4. At incident energies varying from E_{lab}=20-40 MeV, the measured complete fusion cross-sections for ^{158}Tb* nucleus are addressed using DCM in terms of dominant ER decay mode. The role of deformations in the decaying fragments

is studied by considering spherical fragmentation, static deformations and dynamic deformations having effect of temperature included in it. It is observed that with inclusion of static $\beta_{2i}(0)$ and dynamic $\beta_{2i}(T)$ quadrupole deformations the barrier position and barrier height gets modified. At ℓ=ℓ_{max} the structure of fragmentation potential is almost similar for spherical and dynamic deformation but is different for static deformation. Thus, the inclusion of deformations changes the potential energy surfaces (PES) exhibiting variations in the relative preformation probability P_0. For all three approaches, i.e. spherical, static deformed and dynamical deformed choice, the ER contribution reproduces the experimentally measured complete fusion cross-sections, thus giving way to the fact that fission contribution is negligible. Moreover, the DCM based calculations identify the charged particle involved and suggest that ^4H charged particle, contributes about ∼1% towards the ER cross-section of ^{158}Tb* nucleus. Also, it is noticed that with the change in level density there is no significant change in the structure of potential energy surfaces (PES). Further, to explore the shell closure effect of decaying fragments, the ^{6}Li+^{144}Sm reaction is investigated in addition to ^{6}Li+^{152}Sm reaction. As observed for heavy mass Fr nuclei studied in Chapter 3, the shell effects (magic shells) play an important role for intermediate mass ^{158}Tb* nucleus formed through deformed target ^{152}Sm. Additionally, the role of orientation is also explored for ^{158}Tb* nucleus and consistent with the observations for superheavy region, as discussed in chapter 3, it is observed that hot (equatorial) compact orientations favors the symmetric fragment mass distribution whereas, for the cold (polar) elongated orientations an asymmetric fragmentation is preferred. Finally, the suppression in the complete fusion cross-section associated with the break-up of loosely bound projectile ^{6}Li into ^{2}H and ^{4}He fragments is accounted through incomplete fusion (ICF) process studied by applying necessary energy correction in view of binary break-up of ^{6}Li projectile. It is observed that the structure of fragmentation paths is similar for

both CF and ICF processes.

In chapter 5, the work presented in chapters 3 and 4 is further extended to understand the decay of heavy and relatively lighter nuclei formed through complete and incomplete fusion (ICF) processes observed in ^{20}Ne and ^{6}Li induced reactions. For ^{201}Bi* nucleus formed through complete fusion of ^{20}Ne projectile, the role of higher multipole deformations is examined by studying the ER decay mode using spherical choice, with inclusion of quadrupole (β_2) deformations using optimum orientations and hexadecapole (i.e β_2+β_3+β_4) deformations using compact orientation approach. It is observed that mass distribution is symmetric for spherical choice and becomes near-symmetric with inclusion of deformation effects. For all the three approaches, the ER cross-sections attained using DCM are in agreement with experimented data. Besides this, the ^{20}Ne projectile having low α-break-up threshold, breaks-up to form four dominant channels *viz.* ^{4}He, ^{8}Be, ^{14}N and ^{16}O channels which account for incomplete fusion (ICF) process. In agreement with Morgestern systematics, the DCM calculations show that ^{4}He channel contributes maximum towards ICF process, followed by ^{8}Be , ^{14}N and ^{16}O channels which means that the percentage of fractional ICF (f_{ICF}) is highest for asymmetric ^{4}He transfer channel. After applying relevant energy correction, the sum of DCM calculated ER cross-sections obtained for all the four channels is very close to the reported experimental value. This suggests that apart from studying the decay of CN, DCM can also be applied to study the decay processes of nuclei formed through incomplete fusion (ICF) processes. After exploring the role of deformations in CF and application of suitable energy correction in reference to ICF process observed in ^{20}Ne induced reaction, DCM is further applied to address the CF and ICF component in another reaction involving ^{6}Li projectile. In reference to the measured complete fusion data the evaporation residues are studied by implying the sticking limit (I_S) and the non-sticking limit (I_{NS}) of moment of inertia in

framework of DCM. It is observed that the effect of moment of inertia is more prominent in the small interaction range and lighter fragment masses. The choice of moment of inertia explicitly governs the centrifugal potential V_ℓ, which results into large increase in magnitude of fragmentation potential in the ER region. Moreover, the formation probability of ERs is small for the use of non-sticking limit of moment of inertia as compared to sticking limit. Thus, it may be concluded that both approaches seem to be equally capable of handling the neutron evaporation residue data for ^{96}Tc* nucleus with I_S choice being relatively more favorable. Further, the suppression in measured complete fusion cross sections is associated with the incomplete fusion (ICF) process observed due to break up of ^{6}Li projectile. In framework of DCM, the CF and ICF cross sections are separated by confining their contributions in two different ℓ-windows, where CF cross-sections are studied for ℓ=0$\hbar$ to ℓ=ℓ_{CF} while, ICF cross sections are obtained for ℓ_{CF}<ℓ≤ℓ_{max} region by applying relevant energy correction. Owing to the deformations of decaying fragments, ℓ_{CF} varies from 0.65ℓ_{crit} to 1.2ℓ_{crit} with increase in incident energy. The DCM based CF and ICF cross sections are found to agree well with the experimental data and hence, it may be concluded that DCM successfully explains the decay processes associated with CF and ICF process for heavy and intermediate mass region.

In Chapter 6, DCM is further applied to study the decay of light mass nuclei in reference to ^{66}As* nucleus formed in proton halo ^{8}B induced reaction and that of ^{40}Ca*, ^{39}K* nuclei formed in ^{12}C and ^{11}B induced reaction. To check for the consistency of results obtained for heavy and intermediate mass region, the role of deformations in the decay of $^{66}As^*$ nucleus is investigated by fitting the available fusion cross section data using spherical fragmentation approach, quadrupole deformations (β_{2i}) and hexadecapole (β_{2i}-β_{4i}) deformations. As observed earlier for the heavy and intermediary mass nuclei, the role of deformations is prominent at higher angular momentum, ℓ=ℓ_{max} and play a

significant role in fragmentation process. Also the comparative analysis of different decay modes contributing towards the total fusion cross-section of $^{66}As^*$ system is studied. It is observed that at lower ℓ values the LP decay channel dominates, while IMFs and fission fragments start appearing at higher ℓ values. Also, the contribution from LPs is the highest, followed by IMFs and fission fragments at near and above-barrier energies whereas, at below-barrier energy, IMFs dominate over LPs. Thus, LPs, IMFs and fission fragments compete with each other in the decay of ^{66}As* nucleus. Further, following the trend at lower excitation energies, the cross sections at higher energies are also estimated which can further be verified by performing relevant experiment. Besides this, DCM is applied to identify the favorable fragment mass(es) and their contribution towards the measured charge distribution for very light mass nuclei such as, ^{40}Ca* and ^{39}K*. The role of entrance channel effect is studied for ^{39}K* nucleus formed through ^{12}C+^{27}Al and ^{11}B+^{28}Si channels. It is observed that fragmentation potential, preformation probability (P_0) and the penetrability (P) depend on the mass of compound nucleus formed but is independent of the entrance channel effect. The DCM calculations also suggest that in addition to the experimentally observed Z=3,4 and 5, the fragments corresponding to Z=5,6 and LPs may also contribute towards the decay of ^{40}Ca* and ^{39}K* system. Additionally, the DIC process observed in both these light mass nuclei is also studied. Based on the characteristic features of DIC process, the DCM approach is modified in terms of Preformation probability P_0 and angular momentum (ℓ), by distributing P_0=1 equally among all the projectile and target like fragments and by considering the partial waves in the range ℓ_{crit} to ℓ_{max} only, while the lower ℓ region is limited to CN process. It is observed that for all three charge fragments the cross sections for both CN and nCN (DIC) processes obtained using DCM are in good agreement with experimental data. Thus, it may be concluded that DCM adequately identifies the fragment masses corresponding to

a given charge and its application can be extended to study the decay of nuclei exhibiting nCN (DIC) process.

Summarizing, the work of this thesis presents a comprehensive picture of decay modes observed through various processes such as complete fusion (CF), incomplete fusion (ICF) and non-compound nucleus (nCN). In CN channel, relative contribution of ER, IMF and fission etc. is explored by studying the decay analysis of a variety of heavy ion reactions. The ICF component in context of loosley bound projectile such as ^{6}Li, ^{20}Ne etc., is worked out and the application of DCM is extended for nCN based process such as quasi-fission (QF) and deep inelastic collision (DIC) mechanisms. For still better understanding of the reaction dynamics, the work presented here may be extended further to study various other competing processes such quasi-elastic, break-up, fast-fission etc. Also, it would be of further interest to study the effect of higher order deformations and associated non coplanar ($\phi \neq 0$) orientations in reference to different decay mechanisms observed in heavy ion induced reactions.